Structural and Kinetic Characterization of Disease-Associated Tau Mutants

By

Allan Yarahmady

A thesis submitted in partial fulfilment of the requirements for the degree of

Master of Science

Department of Biochemistry

University of Alberta

Abstract

While great advancements have been made in the field of tau biology, one particularly elusive component is the significance of structural variance of tau aggregates linked to disease: we see great structural heterogeneity among the aggregates obtained from various tauopathies despite being made from the same protein. Furthermore, these profiles appear to be consistent across patients with a given disease. This suggests disease-specific cellular triggers that favour certain aggregate structures over others. A better understanding of these differences would bring us closer to defining the critical early stages of disease onset and spread. One way to study this research question is via saturation mutagenesis. Point mutations in tau can have marked effects on aggregate kinetics, structure, and morphology, so this method would allow for a thorough assessment of the sequence-structure relationship for tau aggregation. To achieve this, a high-throughput method of purifying recombinant tau was optimised to be compatible with downstream assays such as those measuring *in vitro* aggregation kinetics or aggregate core structures resistant to protease digestion. In this thesis, a preliminary screen of our developed platform was performed on 36 tau mutants linked to the tauopathy FTLD-tau. These mutants were found to group into ten structural subtypes.

Preface

This thesis is an original work conducted by Allan Yarahmady under the supervision and guidance of Dr. Sue-Ann Mok. Dr. Jónathan Heras from the University of La Rioja provided the algorithm-based program to analyse protein digestion patterns and assisted in data analysis. Jack Moore and Erik Gomez of the Alberta Proteomics and Mass Spectrometry Facility at the University of Alberta assisted with obtaining MALDI spectra. No part of this thesis has been previously published.

Dedication

I dedicate this to BB

Acknowledgements

First and foremost, I would like to thank my supervisor Sue-Ann Mok. I've learned so much from working with her, and I've been infected by her dedicated love for science and curiosity. I would also like to thank Emily McNamara for always being there when I peer over from my desk. We've had so many wild days and nights in the lab together and I couldn't imagine going through grad school without her. I also could not have done it without current and previous lab members. Particularly Heather Baker, Tark Patel, Kerry Sun, and Angelle Britton.

Special thanks as well to my committee members Valerie Sim and Richard Fahlman. Their input has been invaluable over the years and has saved me months of headache and torment. I couldn't have asked for a better committee.

I would also like to thank Jack Moore and Erik Gomez of the Proteomics core as well as the members of the Olivier Julien lab for their help and input in mass spectrometry experiments and providing support and materials when needed. Also, thank you to Jónathan Heras for his help with developing the digest sorting program.

Finally, I would like to thank my parents. They supported me throughout my entire university career and gave me the resources to succeed. They've been there when I needed them, and they never hesitated to let me know that they'd never let me fall. They always say how they are so lucky to have a great son like me, but I truly am so lucky to have two great parents like them. My success is their success, and I'll always be appreciative of them.

Table of Contents

List of Tables

List of Figures

List of Abbreviations

AD	Alzheimer's Disease	
AGD	Argyrophilic Grain Disease	
BH	Brain Homogenate	
CTE	Chronic Traumatic Encephalopathy	
DPBS	Dulbecco's Phosphate Buffered Saline	
dNTP	Deoxynucleotide Triphosphate	
DTT	1,4-Dithiothreitol	
EM	Electron Microscopy	
FTD	Frontotemporal Dementia	
FTLD-tau	Frontotemporal Lobar Degeneration-Tau	
IDP	Intrinsically Disordered Protein	
IPTG	Isopropyl-b-D-1-thiogalactopyranoside	
kDa	Kilo-Dalton	
LB	Luria Bertani	
MAPT	Microtubule Associated Protein Tau	
MALDI-TOF	Matrix Assisted Laser Desorption Ionisation-Time of Flight	
MTBR	Microtubule-Binding Region	
NaCl	Sodium Chloride	
NaF	Sodium Fluoride	
Ni-NTA	Nickel Nitrilotriacetic acid	
PHF	Paired Helical Filament	
PiD	Pick's Disease	
PMSF	Phenylmethylsulfonyl Fluoride	
PSP	Progressive Supranuclear Palsy	
PTM	Post-Translational Modification	
SDS-PAGE	Sodium Dodecyl Sulphate Polyacrylamide Gel Electrophoresis	
SF	Straight Filament	
TB	Terrific Broth	
TDP-43	TAR DNA-binding protein 43	
ThT	Thioflavin T	

WT	Wild Type

Chapter 1

INTRODUCTION

Chapter One: Introduction
1.1 Tauopathies

Alzheimer's disease was first described in 1906 by Alois Alzheimer. He focused primarily on examining patients with psychiatric symptoms and correlating their clinical presentation with brain autopsy samples and whether any visible pathology existed (Hippius & Neundörfer, 2003). One of his patients was a 51-year-old woman who exhibited classic symptoms of dementia such as confusion, emotional outbursts, hallucinations, and impaired memory (Alzheimer et al., 1995). When he examined her post-mortem brain, he observed a significant loss of brain matter. He also remarked upon the presence of fibrils in the brain slices which appeared different from normal structures one would see. The marked difference was specifically in the fibrils' unique thickness and susceptibility to silver impregnation. It wouldn't be for another 80 years that the fibrils Alois remarked upon would be identified as being composed of the protein tau (Brion et al., 1985, p. 198). This is one of two hallmarks of Alzheimer's disease, the other being extracellular amyloid beta plaques made up of misfolded Aβ peptides.

Tau pathology is observed in other neurodegenerative diseases as well. Collectively, these are referred to as tauopathies, and include frontotemporal lobar degeneration with tau pathology (FTLD-tau), progressive supranuclear palsy (PSP), Pick's disease (PiD), chronic traumatic encephalopathy (CTE), and Argyrophilic grain disease (AGD), among others. Tauopathies differ in their presentation, causative factors, tau fibril make-up, brain region affected, and fibril morphology.

1.1.1 Alzheimer's Disease

Alzheimer's disease is the most common form of dementia making up over 50% of cases. It is characterized by the presence of intracellular neurofibrillary tangles (NFTs)

made up of misfolded tau protein and extracellular amyloid beta plaques made up of misfolded Aβ peptide. Aβ pathology is seen much earlier on, before symptom onset with tau pathology more closely correlating with disease progression (Nelson et al., 2012; Whitwell et al., 2008). Common symptoms include memory loss, disorientation, issues with sensory processing, and hallucinations and/or delusions. Certain genetic links have been identified which correspond to a higher risk of developing AD, including: Apo E4 haplotype, mutations in presenilin 1 and 2, and mutations in amyloid precursor protein (APP, the protein that gets cleaved into the Aβ peptide and aggregates to form amyloid beta plaques). However, single nucleotide polymorphisms and mutations in tau have not been linked to AD onset.

1.1.2 Frontotemporal Dementia

Frontotemporal dementia (FTD) is a class of neurodegenerative diseases that share protein misfolding characteristics and is the second most common form of dementia. The misfolding proteins involved in these diseases are TAR DNA-binding protein 43 (TDP-43), RNA-binding protein FUS (FUS), and tau (Olszewska et al., 2016). Tau-related FTD diseases exhibit tau pathology in the form of neurofibrillary tangles however they do not contain increased Aβ pathology compared to age-matched controls (Tan et al., 2017). These diseases can arise either sporadically or due to genetic mutations with approximately 70% of FTD cases being sporadic and 30% linked to genetic factors (Greaves & Rohrer, 2019). Just under 50% of sporadic FTD cases show tau pathology (Mackenzie & Neumann, 2016). Of the 30% of genetic cases of FTD, approximately 10% are tau-related and directly linked to MAPT gene mutations (Mackenzie & Neumann, 2016; Rohrer et al., 2009). The physical presentation of FTD

can fall into three categories: behavioural variant (bvFTD), semantic variant progressive primary aphasia (PPA-S), agrammatic primary aphasia (PPA-G,), and logopenic aphasia (PPA-L) (Devenney et al., 2019). However, there are degrees of phenotypic overlap between these disorders.

Pick's disease is a pathological description of a neurological disorder that exhibits tau pathology and diagnosis is only made post-mortem. PiD typically presents phenotypically as behavioural variant frontotemporal dementia (bvFTD) or nonfluent agrammatic primary progressive aphasia (nfaPPA). Common symptoms include impulsive and inappropriate behaviour, apathy, emotional swings, and impaired language processing. It differs from Alzheimer's disease in that the tau inclusions are made up entirely of a single isoform of tau, where AD inclusions constitute a mixture of tau isoforms (Sergeant et al., 1997). Also, Pick's disease doesn't tend to affect the patient's memory as severely.

1.1.3 Progressive Supranuclear Palsy

Progressive supranuclear palsy is a rarer tauopathy. It may exist on its own or in tandem with FTD (Devenney et al., 2019). This disease falls under the progressive motor decline category. Common symptoms include slow and restricted eye movements, stiffness, difficulty moving, and problems keeping balance. Whereas PiD is composed of one particular tau isoform deposits, tau deposits in PSP are composed of a different isoform. Genetic mutations, both intronic and exonic, in tau have also been identified in patients with PSP (Debnath et al., 2022). Genome-wide association studies (GWAS) have identified SNPs and other genetic factors play a role in the risk for developing sporadic PSP.

1.1.4 Chronic Traumatic Encephalopathy

Chronic traumatic encephalopathy (CTE) is another progressive neurodegenerative disease that exhibits tau pathology. The onset of CTE is highly associated with a singular or repeated traumatic injury to the head (Gavett et al., 2011). CTE has been tied to cognitive decline in athletes participating in high-impact contact sports such as wrestling, football, and hockey, as well as military service people (McKee et al., 2009). Common symptoms include dizziness and disorientation, an increase in aggressive behaviour, as well as a development of parkinsonism manifesting as a loss of motor control as the disease becomes more severe. The age of symptom onset for CTE is lower than other tauopathies due to a closer alignment with environmental factors in etiology (*i.e* sustained head trauma).

1.2 Tau Protein

Tauopathies all share the same common protein, tau, as the pathological driver, however, they differ in protein isoform, pathological spread, disease etiology, symptom and phenotypic presentation, and more.

The microtubule-associated protein tau (MAPT, or just tau) is a protein expressed primarily in the central nervous system. As its name implies, it is largely associated with microtubules in the axons of neurons and modulates microtubule stability and dynamics (Black et al., 1996; Qiang et al., 2018). Tau is an intrinsically disordered protein (IDP) meaning it displays little to no secondary structure and exists natively unfolded. This makes it a prime protein for binding to and associating with other proteins. The region of tau that potentiates binding to microtubules is the microtubule-binding region (MTBR, Figure 1.1). In adults, the MAPT transcript is differentially spliced in the nucleus to

generate six isoforms. Exons 2 and 3 are alternatively spliced to either fully exclude them, only include exon 2, or fully include them. When included, these exons encode for sequence inserts near the N-terminus of the protein. As such, the naming convention for these isoforms relays the number of N-terminal inserts the isoform contains (0N, 1N, or 2N). Exon 10 encodes for a segment in the microtubule-binding region and is alternatively spliced to give rise to tau with either three or four microtubule-binding repeats. The naming convention indicates the number of repeats in the sequence (3R or 4R). In foetal brains, expression of the 3R isoforms is favoured however in adulthood the relative expression of 3R and 4R isoforms equalises (Goedert et al., 1989). The 1N isoforms make up the largest proportion of tau (~50%) followed by the 0N (~40%) and then lastly the 2N isoforms (~10%) (Trabzuni et al., 2012). The presence of a fourth repeat in the microtubule-binding region confers a greater binding ability to the microtubules (Goode et al., 2000; Gustke et al., 1994). This segment also facilitates binding to the negatively charged microtubules by having a higher proportion of positive charges which have specific binding points (Figure 1.2) (Goode et al., 1997; Mukrasch et al., 2007). The expression of tau is also cell-type dependent (Binder et al., 1985), primarily expressed in neurons but also expressed in oligodendrocytes (Goldbaum et al., 2003) and astrocytes (Papasozomenos & Binder, 1987).

1.2.1 Post Translational Modifications

Tau is a host for a myriad of post-translational modifications (PTMs) ranging from methylation, acetylation, glycosylation, ubiquitination, and others (Figure 1.3). The general function of post-translational modifications is to modulate and regulate protein structure, interactions, expression, localization, and degradation (Ramazi & Zahiri, 2021).

Approximately 35% of tau's sequence contains amino acid residues susceptible to PTMs (Alquezar et al., 2021). One particular tau PTM that has been extensively studied is phosphorylation. Insoluble tau obtained from patients is hyperphosphorylated relative to healthy controls (Wesseling et al., 2020). Serine, threonine, and tyrosine make up 10.2%, 7.9%, and 1.1%, respectively, of the sequence of the largest isoform of tau (2N4R), totalling 85 sites for potential phosphorylation. Tau's highly charged nature is imperative for its function as a microtubule-associated protein, so the alteration of its electrostatics in this way can have a marked effect on said function. An increase in phosphorylation of tau leads to a decrease in binding ability to and polymerisation of microtubules (Alonso, Zaidi, Novak, Barra, et al., 2001; Biernat et al., 1993; Lindwall & Cole, 1984). Several sites on tau, including outside the MTBR, show an increase in phosphorylation later on in disease progression aligning with Braak stages V/VI (Neddens et al., 2018). As tau plays a role in microtubule dynamics and axogenesis, a disruption in this function through site-specific phosphorylation leads to aberrant nerve out-growth and cellular processes (Biernat & Mandelkow, 1999). In addition to phosphorylation effects on tau microtubule interactions, *in vitro* experiments have shown that phosphorylation can directly promote the aggregation of tau. Hyperphosphorylation of tau is also capable of spontaneous conversion into aggregates *in vitro* (Alonso, Zaidi, Novak, Grundke-Iqbal, et al., 2001)**.** This indicates that small changes in tau biochemistry can have profound effects on its aggregation and play a crucial role in disease.

Another important PTM implicated in tauopathies is ubiquitination, which is the process of adding the 76 amino acid protein ubiquitin to lysine residues. Most ubiquitination sites identified in tau are within the polyproline region and the MTBR (L. Li

et al., 2022) and tau ubiquitination is increased in AD patients compared to controls (Abreha et al., 2018) with a mixture of mono- and polyubiquitinated chains (Cripps et al., 2006). Ubiquitination of tau likely plays an important role in the aggregation of tau in CTE as ubiquitin is seen in the protease-resistant core of extracted fibrils (Arakhamia et al., 2020).

1.3. Pathological Tau

Protein misfolding diseases are characterised by pathological misfolding of certain proteins in the brain (Hartl, 2017). When the proteins misfold, they are capable of inducing misfolding in other protein molecules forming proteinaceous inclusions which spread throughout the brain. Some of these inclusions are toxic to the cell and lead to cell death contributing to brain atrophy and eventual symptom onset (S. Lee et al., 2020).

1.3.1. Initial Stages of Fibril Formation

Tau natively exists unfolded and associated mainly with microtubules in the axon of the neuron to modulate their stability. The precise mechanism(s) of how tau goes from soluble and microtubule-bound to insoluble amyloidogenic aggregate in disease remains elusive. However, one aspect of aggregation that is crucial is the generation of oligomeric species, an intermediate from monomeric tau to neurofibrillary tangles. Oligomeric species of tau can range in size from three to upwards of 40 protein molecules (Maeda et al., 2007). These oligomeric species exhibit β-sheet rich structures yet do not react with amyloid-binding dyes (Lasagna-Reeves et al., 2010). When neuronal cells are treated with tau oligomers, they confer cytotoxicity through membrane disruption and a decrease in cell viability suggesting oligomers are sufficient for toxicity before mature fibrils even

form (Flach et al., 2012). When oligomers are injected into the brains of mice, impairment in memory, as well as a loss of synaptic connections, were seen (Lasagna-Reeves et al., 2011). The initiation of this process involves a conformational activation of the tau monomer to aggregation competent species (Chen et al., 2019), followed by monomeric addition to the ends of oligomeric and fibrillar species (Arosio et al., 2015).

1.3.2. Mechanisms of Spread

Tauopathies are progressive neurodegenerative diseases meaning they progress from mild to more severe over time with neurofibrillary tangles spreading throughout the brain as the disease progresses. The mechanism by which aggregated tau spreads throughout the brain appears to be disease specific. In Alzheimer's disease, the Braak stages of disease progression are the current standard (Braak et al., 2006; Braak & Braak, 1991). It splits amyloid plaque spread into three stages (A-C) and NFT spread into six (I-VI). Studies in mice suggest that the spread of tau tangles more closely aligns with connectivity between brain regions rather than proximity to affected areas (Ahmed et al., 2014). This connectivity-based spread of aggregated tau was also seen in human patients when studied longitudinally with image-based systems (Franzmeier et al., 2020). The spread of pathological tau throughout the brain via nerve connectivity, as opposed to radial spread, suggests a potential cascade via synaptic transmission. This mechanism of spread from one neuron to the next is observed for smaller order oligomers and aggregates, whereas large fibrillar aggregates may not be taken up in cells due to size limitations of uptake mechanisms (Wu et al., 2013). Once the aggregated protein enters the cell, it is capable of inducing misfolding in the resident tau molecules of the receiver cell and generating seeds that can further go on to spread (Nam & Choi, 2018). The ability

for aggregates to template and induce aggregation is sequence specific (Sanders et al., 2014). Structural features of aggregates are also able to be propagated in a cell line over several passages and these structurally distinct aggregates are also capable of inducing different pathological phenotypes when infected into mice (Sanders et al., 2014). The structural fidelity of templating and differential phenotypic presentation is an important factor to consider when comparing tauopathies, as they exhibit slightly different presentations.

1.3.3. Fibril Structure and Tau Strains

Tau deposits in the brain are insoluble which makes them relatively simple to isolate from patient brain samples. A series of ultracentrifugation steps and treatment with sarkosyl (an anionic detergent) is sufficient to purify a population of higher order, long, mature fibrils from brain homogenate (Diner et al., 2017). In AD, two species of fibrils are seen: paired helical filaments (PHF) and straight filaments (SF) (Figure 1.4A and B) with PHFs making up the majority of aggregates in AD (Falcon et al., 2018). Paired helical filaments exhibit a twisted ribbon shape with a helical pitch of approximately 80 nm (Crowther, 1991). Straight filaments exhibit a more uniform morphology with a subtle helical pitch of approximately 160 nm. Cryogenic electron microscopy modelling indicates that the core of both PHFs and SFs are made up of two protofilaments associating either head-to-head in the paired helical filament or back-to-back in the straight filament (Fitzpatrick et al., 2017). The protofilaments in each appear to be identical and are made up of many tau subunits stacked together with a rise of 4.7 Å and a twist of approximately −1° (Figure 1.4C). The head-to-head association of PHFs exhibit a twofold rotational symmetry with the interface comprising residues P332-Q336 whereas the back-to-back

association of SFs is asymmetric with the interface comprising residues T319-S324 on one protofilament and V313-K317 on the second protofilament (Figure 1.4B, red arrow).

The precise packing and association of individual tau molecules in the core take on a characteristic in-register parallel β-sheet hook shape (Figure 1.4C). This fold appears to be a common fold specific to Alzheimer's disease (Falcon et al., 2018). There are several key interactions within the core of this hook-shape that stabilise it and likely make it a more favourable fold. The interior of the hook tip contains a hydrophobic pocket, and the exterior of the tip contains alternating positively and negatively charged amino acids that interact to stabilise this conformation (Figure 1.4D). Also, the location of the $_{364}PGGG_{367}$ motif allows for the tight kink in the interior of the turn in the curve (Figure 1.4C, purple circle) due to glycine's highly flexible nature owed to its small side chain. It should be noted that this core region resolved by cryo-EM only comprises residues V306 to F378. The rest of the sequence envelopes the fibril core in what's referred to as the "fuzzy coat". This coat is easily accessible to proteases and when proteolysed, the core becomes accessible to antibodies (Falcon et al., 2018). Through the use of antibodies, it was discovered that the N-terminus of the tau protein in these fibrils is protected despite the core of the fibril comprising the MTBR region (Bondareff et al., 1994). This suggested the N-terminus folds back and associates with the core of the fibril. This was corroborated by cryo-EM with additional density seen associating with the core on the periphery (Fitzpatrick et al., 2017).

Cryogenic electron microscopy has continued to resolve a growing collection of tau aggregate structures from tauopathies. The tau aggregate morphology in Pick's Disease is different from AD. The core fold of PiD protofilaments are elongated with a

less pronounced curvature as that in AD and include 21 additional residues on the N-terminal end of the sequence, however residues 275–305 of R2 are not present as PiD is a 3R tauopathy. The narrow Pick filament (NPF) is made up of a single protofilament and the wide Pick filament is made up of two protofilaments bound at their distal tips (Falcon, Zhang, Murzin, et al., 2018). This association is stabilised by van der Waals interactions of the C322-S324 at the interface and not through a disulfide bridge of the neighbouring cysteines as the WPF is stable under reducing conditions.

These structural differences among pathological tau inclusions are reminiscent of strains among prion diseases, which are neurodegenerative diseases caused by exposure to the infectious prion protein. Biochemical assessment of prion infectious material extracted from inoculated hamsters (Bessen & Marsh, 1992) and mice (Kascsak et al., 1985; Telling et al., 1996), as well as from human patients (Gambetti et al., 2003), showing different clinical presentations reveals that the prion protein itself has taken on different properties and may be the source of the variation. Indeed, different conformations of prion protein alone are sufficient to induce different phenotypes (Tanaka et al., 2004). It is presently unclear the significance of these polymorphic structures or how they confer different physical phenotypes. The initial conditions that favour one folding pathway over another resulting in these distinct polymorphs and differential isoform makeups could be the differentiating factor that distinguishes the different tauopathies from each other. Pinpointing the pathways that precede fibril formation of specific aggregate structures would aid in the generation of therapeutic strategies to prevent aggregation from occurring.

1.3.4. Disease-Associated Tau Mutants

As mentioned previously, mutations in tau have been found to lead to the development of FTLD-tau. These mutations are autosomal dominant occurring on the MAPT gene of chromosome seventeen. Many types of mutations have been identified including missense, intronic, silent, and deletions (Table 1.1). However, the majority of them are missense mutations, mostly occurring in the microtubule binding region (Figure 1.5). Three percent of frontotemporal dementia cases can be linked to MAPT mutations. These mutations can vary in their disease presentation as well as physiological effect (Pickering-Brown et al., 2002; Stanford et al., 2004). While mutations in the intronic segments of the MAPT gene do not get expressed in the final protein sequence, they are still associated with disease onset (Pickering-Brown et al., 2002). Some silent mutations have also been shown to alter the 3R:4R ratio in patients (D'Souza et al., 1999; Spillantini et al., 2000). On a biochemical level, missense mutations associated with disease can have profound effects. Mutant tau proteins can promote tau to incorporate more phosphates upon phosphorylation at a faster rate *in vitro* compared to WT (Alonso et al., 2004). The trend for most mutants is a reduction in microtubule assembly from tubulin compared to WT (Combs & Gamblin, 2012; Strang et al., 2019), although the effect of binding to microtubules from these mutations are largely undetermined. Some tau mutations also promote the oligomeric association of tau compared to WT (Maeda et al., 2018), which is significant as oligomeric tau is thought to be the conveyer of toxicity in disease (Flach et al., 2012). When fully fibrillised, tau mutants also exhibit varied fibril morphology when produced *in vitro* (Combs & Gamblin, 2012). Some mutants generated shorter fibrils while not affecting total fibrillisation amounts (e.g., G303V) while one mutant had an overall inhibitory effect on aggregation (K369I). Different mutations in the same

residue can even lead to different diseases. For example, N296N and N296H result in FTLD-tau whereas ΔN296 results in progressive supranuclear palsy (Grover et al., 2002)**.**

One issue in the field of tau mutants is the lack of consistency between studies. They occur under different conditions with different constructs and different reagents. This makes comparison of mutants and their biochemical properties challenging, particularly with aggregation kinetic analysis which depends immensely on the inducer used. There are also many mutants where limited or no biochemical data is available.

1.4. *In Vitro* Assays

The field of protein misfolding has been greatly aided by the advent of *in vitro* techniques to study protein misfolding and aggregation. One parameter that has been of great significance is measuring protein aggregation in real-time. This is traditionally done spectroscopically through the use of certain fluorescent dyes (Sui et al., 2015) or through the detection of the absorbed light caused by turbidity of insoluble aggregates (Dolado et al., 2005). Understanding the molecular basis by which proteins begin to misfold and aggregate can aid in the development of treatments or preventative measures for protein misfolding diseases. One of the benefits of *in vitro* techniques is the ability to control the conditions and control for confounding variables (*e.g* post-translational modifications). However, these conditions often differ substantially from the biological context in which the diseases arise. Cellular studies partially compensate for this limitation and provide a way to study protein misfolding and dynamics in a more biologically relevant system. While no lab environment will ever perfectly mimic the human body, advances in science have brought us very far.

1.4.1. Detection Methods for Aggregation

Soluble proteins in solution will minimally absorb light (aside from slight absorption at 280 nm due to the presence of aromatic amino acids). During the aggregation process of some misfolding proteins, they will generally form long amyloidogenic fibrils which are insoluble. As such, the generation of these fibrils can be monitored by the absorbance of light over time. An increase in absorbed light indicates an increase in the presence of insoluble aggregates. Such assays are non-specific and will generate a signal at any precipitation of the proteins in solution. This is an important caveat when other proteins or added molecules that have low solubility or stability in the buffer conditions of the assay are included in the reaction.

A more specific measure of protein aggregation can be made through the use of fluorescent amyloid binding dyes. These dyes are non-fluorescent in solution as they contain two aromatic rings that rotate freely along the bond axis between them, quenching any excited state due to absorbed light. However, when they bind to amyloidogenic structures, a change in environment causes the structure of the dye to become rigid and this allows for the dye to turn fluorescent which can be detected using a fluorescence spectrometer (Figure 1.6) (Biancalana & Koide, 2010). Some common amyloid binding dyes used in this end are thioflavin S and T as well as congo red (although congo red exhibits apple-green birefringence under polarised light when bound to amyloids, not fluorescence). These dyes can also be used as diagnostic tools by staining brain tissue samples and then detecting the change in spectral properties compared to healthy controls (Skovronsky et al., 2000).

1.4.1.1 Kinetic Assay

When using fluorescent amyloid binding dyes to detect aggregation *in vitro* measured over time, a kinetic curve is generated (Figure 1.5). The curve has three main phases: the lag phase, the elongation phase, and the plateau phase. The lag phase is the initial time after the aggregation process has started and monitoring has begun. During this phase, the proteins are associated with each other as well as any present cofactors and the fluorescent signal is at a minimum. At this time many nuclei for extension are forming as well as oligomeric species (Arosio et al., 2015). Eventually, these nuclei grow enough such that they can be detected by the amyloid dye and the fluorescent signal rapidly increases indicating an elongation of nascent amyloidogenic aggregates (Figure 1.5). The time at which this nucleation event occurs is referred to as the lag time and will vary with buffer conditions, salt concentration, cofactors present, temperature, and protein type. Eventually, the elongation process reaches equilibrium and enters the plateau phase where the fluorescent signal stabilises and reaches its maximal point, referred to as the maximum amplitude of the curve. The aggregation reaction is very amenable to manipulation with the ability to introduce certain inducers, protein chaperones, or vary the buffer conditions. Taken together, the assessment of kinetic parameters of aggregation under different conditions provides valuable insight into the early stages of aggregation and provides a method for testing potential aggregation inhibitors or modulators.

1.4.2 Aggregation Inducers

Tau is a highly charged protein and as such exhibits a high degree of solubility and stability in aqueous solutions over a wide range of pH and temperatures (Greenberg et

al., 1992; Weingarten et al., 1975). A result of tau's hydrophilicity is the difficulty by which wild-type tau can spontaneously convert to insoluble aggregates *in vitro* on its own. A common way to overcome this hurdle is through the use of cofactors. These cofactors, when added to the aggregation reaction, promote the conversion of tau from soluble to insoluble. The more commonly used cofactors are generally negatively charged and act by associating with the highly positively charged regions of the tau molecule (Fichou et al., 2019). Some of these include DNA (Tetz et al., 2020), arachidonic acid (Barracchia et al., 2020), polyphosphate (Wickramasinghe et al., 2019), and heparin.

1.4.2.1. Heparin

Heparin is an endogenously produced sulfated glycosaminoglycan that is contained largely in granules of mast cells involved in immune response and blood coagulant homeostasis (M. S. Lee & Kong, 2015; Nader et al., 1999). Heparan sulphates associate with tau aggregates in disease and suggest a physiological role in their proliferation (Goedert et al., 1996; Hernández et al., 2002). Heparin may play a role in tau pathology by promoting phosphorylation *via* Glycogen synthase kinase-3 which associates with tau inclusions and is enriched in the sarkosyl-insoluble fraction of brain extracts (Ferrer et al., 2002; Moreno et al., 1995). When combined *in vitro*, heparin promotes rapid tau aggregation into mature amyloidogenic fibrils by acting as a chemical chaperone promoting an aggregation-prone structural conversion in monomeric tau which is more amenable to self-association (Fichou et al., 2019). This process is understood to start with the association of tau with oligomers that exist as a diverse population (Magnus Kjaergaard et al., 2018). These oligomeric species recruit other molecules of tau and eventually grow into mature amyloid fibrils. The role of heparin in the later stages of this

process is presently unclear, however, it appears to associate with and help stabilise the mature fibril (Fichou, Lin, et al., 2018). The structures of the aggregates generated using heparin are different from those found in patient-derived fibrils as well as are more heterogeneous (Fichou, Vigers, et al., 2018; Zhang et al., 2019). The core region of the heparin-induced aggregates comprises R2 and R3 of the MTBR but the core of AD derived aggregates is made up of R3 and R4 (Andronesi et al., 2008; L. Li et al., 2002). This difference in the core structure suggests that the folding pathway by which tau aggregates *in vitro* when induced by heparin differs from a disease state.

1.4.2.2 Cofactor-Less Aggregation

While wild-type tau does not spontaneously aggregate *in vitro*, other conditions allow for this conversion. Some tau mutants (such as P301L and ΔK280) are so aggregation-prone that they are capable of spontaneously aggregating in the absence of any inducer or cofactor. More recently, certain truncated constructs of tau in differing buffer conditions have been shown to generate aggregates *in lieu* of cofactor that also mimic aggregates found in disease (Lövestam et al., 2022). Various conditions were able to recapitulate AD, CTE, and GGT core structures. However, these aggregates generated from truncation constructs do not have the fuzzy coat surrounding the aggregate which may reduce toxicity to cells as has been seen in other truncation constructs (Shammas et al., 2015).

1.4.3 Methods for Studying Fibril Structure

1.4.3.1 Electron Microscopy

Electron microscopy initially gained popularity for analysing fibrils due to its capacity for high-resolution and higher magnification images (Harris, 2015). Negative stain electron microscopy of neurofibrillary tangles extracted from patients and generated *in vitro* exhibited a long, fibrillar morphology characteristic of amyloids with a twisted ribbon structure (Crowther, 1991; Wille et al., 1992). This technique utilises a heavy metal salt solution (such as uranyl acetate) to encapsulate the fibril and reveal structural elements with a resolution in the range of ~20 Å. Developments in computer software allows for image analysis and 3D reconstruction of negative stained samples to increase resolution to ~10 Å (Frank et al., 1996; Ludtke et al., 1999). The sample is destroyed upon staining using this technique so its ability to gain any high-resolution information is limited. The advent of cryogenic electron microscopy (cryo-EM) allowed for a preservation of the biological material by suspending it within vitreous water. Analysis of amyloidogenic proteins utilizing cryo-EM generated structures with near-atomic resolutions of ~3 Å (Fitzpatrick et al., 2017; Guerrero-Ferreira et al., 2018).

1.4.3.2 Limited Proteolysis

One feature of amyloidogenic fibrils is their resistance to protease digestion. The tight packing of the core blocks accessibility to the protease rendering the core most segments of the protein protected while the extraneous segments are free to be digested. This method has been used to determine prion strain types of human PrP samples (Morales et al., 2007). When tau aggregates, the fibrils have two components: the core and the fuzzy coat. The loosely packed fuzzy coat surrounds the core of the fibril and when treated with a protease (such as trypsin), the fuzzy coat is digested. The remaining core is able to be resolved by SDS-PAGE and thus reveal structural and sequence

information by exhibiting different banding patterns. This procedure is capable of determining strain differences between patient-derived aggregates and aggregates passaged through cell seeding assays (Nam & Choi, 2018). Sarkosyl insoluble aggregates from patients of several tauopathies also exhibit structural differences using this method, confirming previous cryo-EM studies (Taniguchi-Watanabe et al., 2016). Through sequence analysis, the identity of the peptides resolved by limited proteolysis can be determined and mapped back to the protein sequence, thus indicating which segments were protected from digestion. Another way to obtain sequence information is through antibody labelling. The fibrils can be treated with protease for various time points and through the use of dot blotting, the ablation of certain epitope reactivity can indicate its proximity to the protease resistant core (Arakhamia et al., 2020).

1.5 Goals for this Project

The concept of prion strains is a well-accepted concept in the prion field. It describes the phenomena of a single misfolding protein being capable of inducing subtly different disease states and symptoms depending on several factors. As with prion disease, it has been noted that other protein misfolding diseases exhibit this strain phenomenon. This has been demonstrated with tau (Shi et al., 2021), alpha-synuclein (Bousset et al., 2013), and most recently with beta-amyloid (Lu et al., 2013; Maxwell et al., 2021). So, it stands that a complex event that would cause a protein to misfold in these cases could also produce various conditions favouring certain folding pathways leading to conformational differences. A common feature of these proteins is that they are largely disordered, showing little secondary structure. This allows for a variety of

interactions and modifications that can alter charge distribution, pI, localization, and function. All of these factors play a role in configuring the conditions necessary to cause the proteins to misfold. Their disordered nature makes these proteins a blank canvas on which cellular processes and signalling pathways can cultivate any number of final aggregate structures. The precise conditions that select for different conformations over others as well as the importance of these specific conformations are presently unknown.

One thing that is known is the link between certain point mutations in tau leading to disease, in the case of FTLD-tau. If there is no secondary structure that the mutation could disturb, then what allows these mutations to promote pathological tau formation? With this project, I endeavoured to do a comprehensive analysis of the relationship between the tau sequence and its aggregate properties including fibril structure as well as aggregation kinetics. To that end, I planned on performing saturation mutagenesis on a segment of the tau sequence to generate hundreds to thousands of mutants to give a fuller picture of which regions of the sequence play a crucial role in aggregation and whether certain mutations can dictate which fibril structures get produced. To perform this mutant screen, a robust workflow was optimised that allowed for the expression and purification of tau in a high-throughput manner as well as the ability to characterise their kinetic parameters efficiently and reproducibly. An assay was also developed that allowed us to compare fibril structure profiles of each mutant in a scalable format that is amenable for high-throughput analysis.

A starting point for verifying the reproducibility of this assay was to study the disease-associated tau mutants that have been reported thus far. Limited biochemical data is available on these mutants, so our optimised assay has the ability to contribute

valuable insight into the aggregation process for tau *in vitro*. Comparing our results to what has been reported in the literature provides a threshold for the success of this assay.
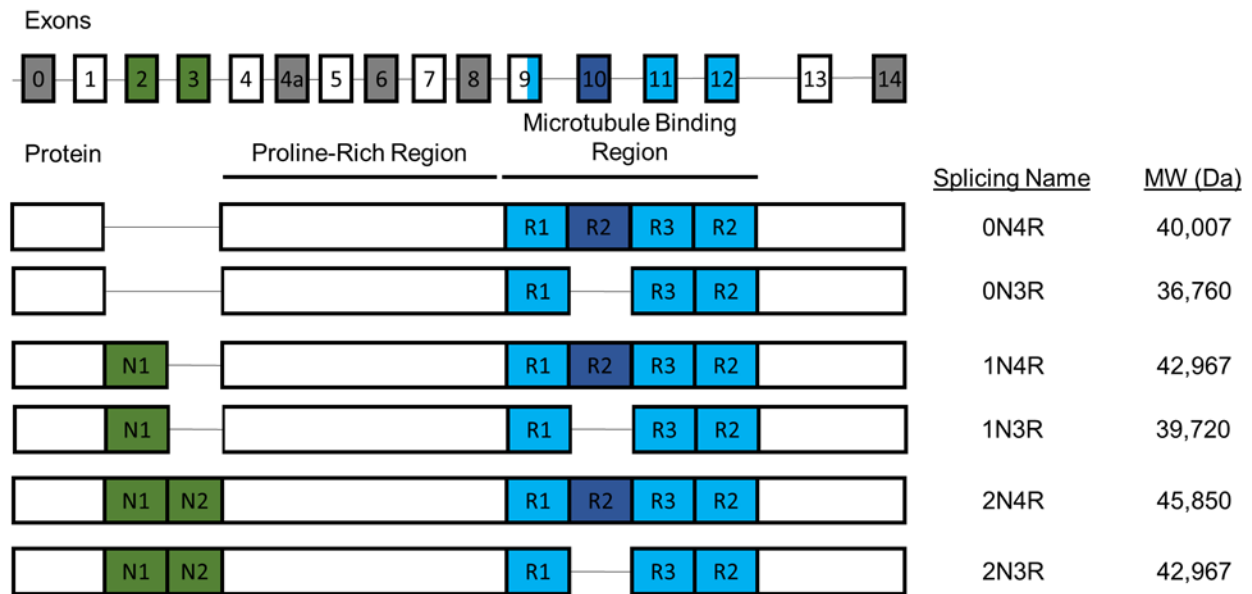
Figure 1.1: **The MAPT gene is alternatively spliced in the brain giving rise to six tau isoforms.** Two inserts at the N-terminal region corresponding to exons 2 and 3 (coloured green) are either fully included (2N), partially included (1N), or fully excluded (0N). Within the microtubule binding region (MTBR) exists four sequence repeats (R1-R4) that are coloured in blue. The second repeat (R2) corresponding to exon 10 (coloured dark blue) can be included (4R) or excluded (3R). Different combinations of the splicing variations at the N-terminus and MTBR in the tau pre-mRNA result in the six isoforms expressed in adults in the CNS. Tau also contains a proline-rich region that is enriched with over 16% proline residues. Indicated to the right of each tau isoform is their name based on their splicing pattern and MW (Da). Areas coloured in white are common to all isoforms.
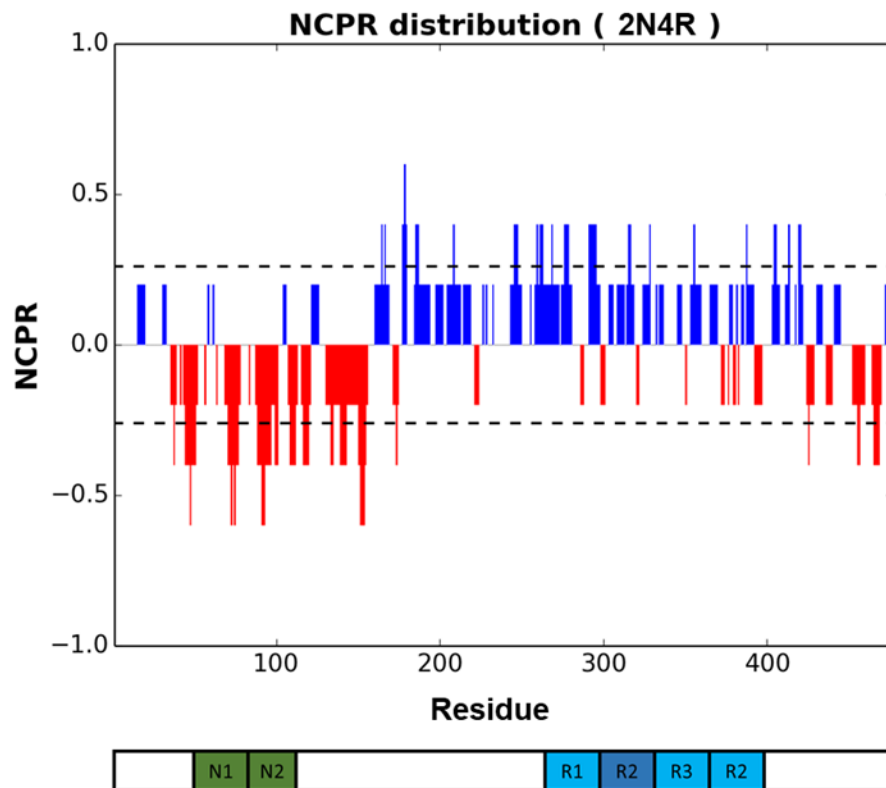
Figure 1.2: **Charge per residue of 2N4R tau.** Shown above is the net charge per residue graphed along the sequence of the largest tau isoform, 2N4R. A value of zero indicates a net 0 charge and a positive or negative NCPR value indicates a positive or negative net charge for that region. The charge in the N-terminal region is highly negative and the net charge in the MTBR region is highly positive. Figure obtained using CIDER (http://pappulab.wustl.edu/CIDER/analysis/, Holehouse et al., 2017).

Figure 1.3: **Post-translational modifications of tau identified in AD**. Insoluble tau was extracted from post-mortem Angular Gyrus (BA39) tissues of Alzheimer's patients and PTM profiles were assessed using mass spectrometry. Phosphorylation, ubiquitination, acetylation, and methylation modifications are shown as their frequency occurring among AD patients. This figure was reproduced and adapted with permission from SpringerNature Copyright Clearance Center licence from (Wesseling et al., 2020)

Figure 1.4: **Core structural fold of Alzheimer's patient derived tau filaments.** Filaments extracted from AD patients take on two morphologies: paired helical filaments (A) and straight filaments (B). A single protofilament is shared between them but they differ in how they associate. *C*. Tau fibrils exhibit an in-register parallel β-sheet where each molecule is aligned with each other along the fibril axis. *D*. This figure was reproduced and adapted with permission from SpringerNature Copyright Clearance Center licence from Fitzpatrick et al., 2017.
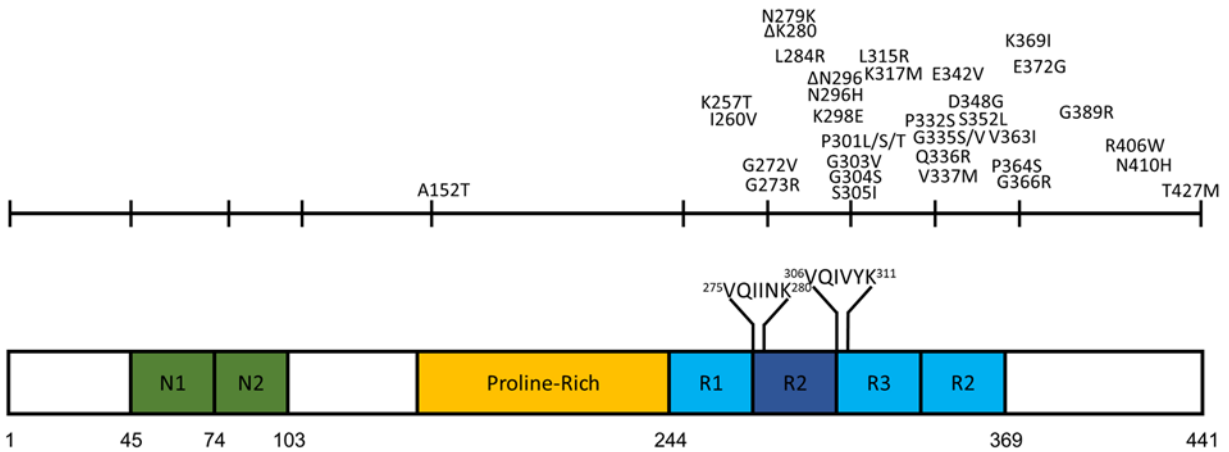
Figure 1.5: **Schematic of tau sequence highlighting disease associated missense mutations.** Frontotemporal lobar degeneration (FTLD-tau) has been linked to several missense mutations in tau, selected ones shown above. Most disease-associated missense mutants are clustered around the MTBR region which makes up the core of aggregated tau filaments.
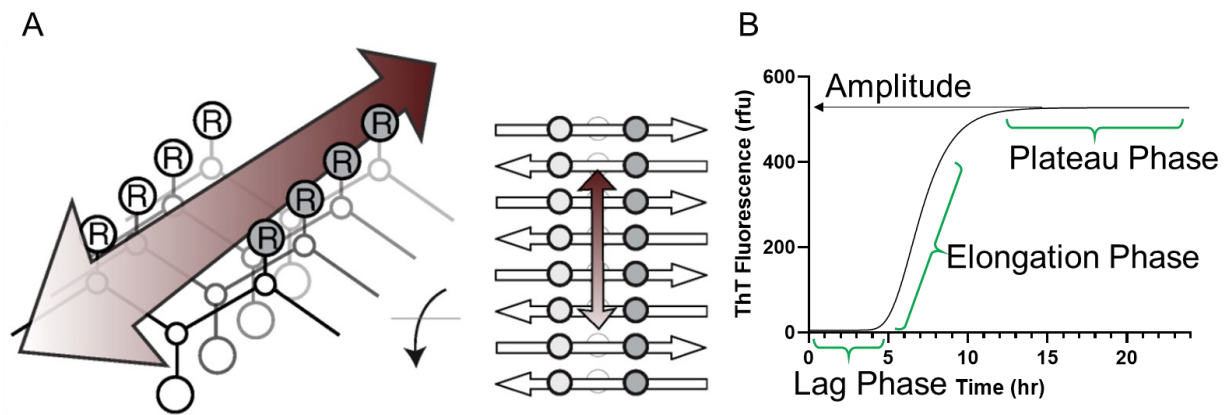
Figure 1.6: **Thioflavin T is used to assess kinetic parameters of aggregation.** *A*. Thioflavin T (ThT) is an amyloid binding dye that exhibits a fluorescent shift upon binding to amyloid fibrils. The binding site of ThT along the amyloid fibril exists along the axis between constituent residue side chains grooves. *B*. Once induced to aggregate, the reaction exhibits a lag phase where transient interactions are taking place and no signal is seen. Then a nucleation event occurs, and the reaction enters the elongation phase where rapid increase in fluorescent signal indicates an elongation of the fibril. The time it takes for this nucleation event to occur is known as the lag time. Eventually, the reaction reaches equilibrium, and it enters the plateau phase indicated by a flattening and stabilisation of the fluorescent signal. This final signal is known as the amplitude of the curve. The image in panel A was reproduced and adapted with permission from SpringerNature Copyright Clearance Center licence from Biancalana & Koide, 2010**.**

Table 1.1**: Number of mutant types of MAPT identified in patients.** (obtained from AlzForum Mutant Database, https://www.alzforum.org/mutations/search?genes[]=492&diseases =&keywords-entry=&keywords=#results)

Missense	Intronic	Silent	Deletion
58	13	13	3

Chapter 2

MATERIALS AND METHODS

2.1. Cloning of Tau Isoforms

Tau exists as six isoforms, generated by alternative splicing of the MAPT gene. The difference lies in the number of N-terminal repeats (0N, 1N, or 2N) and microtubule binding repeats (3R or 4R). 0N4R and 0N3R tau in the pET28a expression vector with an N-terminal Thrombin-cleavable His tag were used as the backbone for creating the other isoform constructs. Sequences for the N-terminal inserts were obtained and ordered as gBlocks® gene fragments from IDT with BamHI and SacII cut sites on the 5' and 3' end, respectively (Table 2). Both parent vectors were double-digested with SacII and BamHI restriction enzymes (New England BioLabs) and simultaneously treated with antarctic phosphatase (New England BioLabs) at 37 °C for 20 minutes to prevent recircularization, as outlined in table 1. The gene fragments were also digested with SacII and BamHI and column purified. Vectors and inserts were ligated with Quick Ligase (New England Biolabs) at a 3:1 molar ratio.. Once completed, the reaction mixture was transformed into DH5α cells, DNA from positive clones were extracted by miniprep (Truin Science) and the clone sequence was validated by Sanger sequencing.

Table 2.1: Double Digest and Phosphatase Reaction Mixture

Reagent	Quantity
CutSmart® Buffer	5 µL
Phosphatase Buffer	5 µL
DNA	up to 1 µg
SacII enzyme	1 µL
BamHI enzyme	1 µL

Antarctic Phosphatase	1 µL
NucleaseFree Water	up to 50 µL
Total Volume	50 µL

2.2. Plasmid Transformation of *E. coli*

To transform, 1-5 µL of DNA was added to 50 µL of thawed DH5α *E. coli* cells for plasmid purification or to thawed BL21-CodonPlus-RP *E. coli* cells (Agilent) for protein expression. The cells were incubated on ice for 30 minutes. The cells were then placed in a 42 °C water bath for 30 seconds then placed on ice for two minutes. One millilitre of LB was added to the cells, and they were incubated at 37 °C with shaking for 1 hour. When transforming with ligation products, the cells were centrifuged at 12,000xg for 1 minute, 900 µL of the supernatant was removed, and the cells were resuspended in the remaining volume. The cells were spread on antibiotic-containing LB agar plates at a volume of 150 µL and left to dry for 10-20 minutes. The plates were then incubated at 37 °C overnight and single colonies were picked the next day and grown in 3 mL cultures of LB for up to 12 hours. The culture was then mixed 1:1 with 60% glycerol to create a glycerol stock of the transformed *E. coli* for later inoculations.

2.3. High-throughput Site-Directed Mutagenesis

Some mutants were already previously made (Coppola et al., 2012; Ghetti et al., 2015). To generate the remaining mutants in our library, mutagenesis was performed in 96-well plates. The pET28a vector containing the 0N4R tau gene was used as the template. The online Agilent Primer Design tool (https://www.agilent.com/store/primerDesignProgram.jsp) was used to design the

mutagenic primers, ordered from IDT (Table 3). The reactions were set up as follows: 0.2 ng/μL template, 0.5 μM forward primer, 0.5 μM reverse primer, 200 μM dNTPs (Invitrogen), 2 units Q5 polymerase (NEB), 1X Q5 reaction buffer, 1X Q5 GC Enhancer. The reactions were incubated using a thermocycler using the following conditions: 95 °C for 5 minutes, 20 cycles of 95 °C for 10 seconds, 50 °C for 30 seconds, 72 °C for 350 seconds, then 72 °C for 10 minutes. The reactions were supplemented with Anza restriction buffer then DpnI treated for 20 minutes at 37 °C. The reactions were transformed into DH5α cells. Single colonies were picked, and the mutant plasmids were extracted from the cultures using a miniprep DNA extraction kit (Truin Science). The extracted DNA was verified by Sanger sequencing using T7 forward or reverse primers. Once verified, the mutant plasmids were transformed into BL21-CodonPlus-RP competent cells (Agilent) for expression.

Table 2.2: Primer sequences for disease associated tau mutants

	Forward	Reverse
K257T	GAC CTG AAG AAT GTC ACG TCC AAG ATC GGC TCC	GGA GCC GAT CTT GGA CGT GAC ATT CTT CAG GTC
I260V	AGA ATG TCA AGT CCA AGG TCG GCT CCA CTG AGA AC	GTT CTC AGT GGA GCC GAC CTT GGA CTT GAC ATT CT
G273R	CAG CCG GGA GGC AGG AAG GTG CAG A	TCT GCA CCT TCC TGC CTC CCG GCT G
ΔN296	AGT GTG GCT CAA AGG ATA TCA AAC ACG TCC CGG	CCG GGA CGT GTT TGA TAT CCT TTG AGC CAC ACT
N296H	AGT GTG GCT CAA AGG ATC ATA TCA AAC ACG TCC CG	CGG GAC GTG TTT GAT ATG ATC CTT TGA GCC ACA CT
K298E	TGT GGC TCA AAG GAT AAT ATC GAG CAC GTC CCG GGA GGC	GCC TCC CGG GAC GTG CTC GAT ATT ATC CTT TGA GCC ACA
P301T	AAT ATC AAA CAC GTC ACG GGA GGC GGC AGT G	CAC TGC CGC CTC CCG TGA CGT GTT TGA TAT T

	Forward	Reverse
G304S	CGT CCC GGG AGG CAG CAG TGT GCA AAT	ATT TGC ACA CTG CTG CCT CCC GGG ACG
S305I	TCC CGG GAG GCG GCA TTG TGC AAA TAG TC	GAC TAT TTG CAC AAT GCC GCC TCC CGG GA
G335S	ATC CAT CAT AAA CCA GGA GGT AGC CAG GTG GAA G	CTT CCA CCT GGC TAC CTC CTG GTT TAT GAT GGA T
Q336R	AAA CCA GGA GGT GGC CGG GTG GAA GTA AAA TCT G	CAG ATT TTA CTT CCA CCC GGC CAC CTC CTG GTT T
E342V	CAG GTG GAA GTA AAA TCT GTG AAG CTT GAC TTC AAG GAC	GTC CTT GAA GTC AAG CTT CAC AGA TTT TAC TTC CAC CTG
S352L	AAG GAC AGA GTC AGT TG AAG ATT GGG TCC CTG	CAG GGA CCC AAT CTT CAA CTG GAC TCT GTC CTT
V363I	GAC AAT ATC ACC CAC ATC CCT GGC GGA GGA A	TTC CTC CGC CAG GGA TGT GGG TGA TAT TGT C
G366R	CAC CCA CGT CCC TGG CAG AGG AAA TAA AAA GAT T	AAT CTT TTT ATT TCC TCT GCC AGG GAC GTG GGT G
K369I	GTC CCT GGC GGA GGA AAT ATA AAG ATT GAA ACC CAC	GTG GGT TTC AAT CTT TAT ATT TCC TCC GCC AGG GAC
E372G	GCG GAG GAA ATA AAA AGA TTG GAA CCC ACA AGC TGA CCT T	AAG GTC AGC TTG TGG GTT CCA ATC TTT TTA TTT CCT CCG C
N410H	CAC GGC ATC TCA GCC ATG TCT CCT CCA CC	GGT GGA GGA GAC ATG GCT GAG ATG CCG TG
T427M	GCC CCA GCT CGC CAT GCT AGC TGA CG	CGT CAG CTA GCA TGG CGA GCT GGG GC

2.4. Large Scale Tau Expression and Purification

Constructs were transformed into BL21-CodonPlus-RP competent cells (Agilent). Transformants were grown overnight at 37 °C in Terrific Broth containing 50 µg/mL Kanamycin and 34 µg/mL Chloramphenicol. The culture was then diluted 1:50 in four litres of Kanamycin-containing Terrific Broth. Once the absorbance of the cultures at 600 nm reached 0.6, a small molecule chaperone solution of Betaine and NaCl were added

to 1.66 mM and 83 mM, respectively, to each litre of culture and incubated for another 30 minutes. The cultures were then induced with 300 µM IPTG for 1.5 hours. The cells were harvested by centrifugation at 6000xg for 10 minutes and resuspended in 50 mL of ice-cold resuspension buffer (20 mM MES pH 6.8, 1 mM EGTA, 0.2 mM MgCl2, 5 mM DTT, 1 mM PMSF). The suspension was homogenised in a Dounce homogenizer and lysed by Emulsiflex (Avestin) under 15,000psi. NaCl was added to 0.5 M and the lysate was submerged in boiling water and boiled for 30 minutes. The boiled lysate was centrifuged at 20,000xg at 4 °C for 45 minutes. The clarified supernatant containing soluble tau (90-110mL) was placed into 3500 MWCO dialysis tubing (ThermoFisher) and dialyzed into 4 L of Cation Exchange Buffer A (20 mM MES pH 6.8, 50 mM NaCl, 1 mM EGTA, 1 mM MgCl2, 2 mM DTT, 1 mM PMSF) overnight.

The dialyzed lysate was then purified by cation exchange chromatography via application to an SP Sepharose column (GE Life Sciences) and the flow-through was discarded. The column was washed with 2.5 CV of Cation Buffer A then 2.5 CV of 14% Cation Buffer B (20 mM MES pH 6.8, 1 M NaCl, 1 mM EGTA, 1 mM MgCl2, 2 mM DTT). Tau was eluted using a gradient of 14-60% Buffer B and collected into 7.5 mL fractions. Samples of eluted fractions were resolved using SDS-PAGE and stained for total protein with Coomassie Brilliant Blue (VWR). The fractions containing full-length tau were pooled, concentrated with a 3 kDa cut-off centrifugal filter unit (Pall), and frozen in 1 mL aliquots. Prior to use, aliquots were thawed and dialyzed in 1X DPBS (Gibco) with 2 mM DTT.

2.5. Small Scale Tau Expression and Purification

Transformed BL21-CodonPlus-RP competent cells (Agilent) were inoculated into 1 mL of TB containing 50 µg/mL Kanamycin and 34 µg/mL Chloramphenicol and grown

overnight at 37 °C. The culture was then diluted 1:50 in 40 mL of Kanamycin-containing TB. Once the absorbance of the cultures at 600 nm reached 0.6, the cultures were then induced with 500 µM IPTG and incubated for 1 hour. The cells were harvested by centrifugation at 3000xg for 15 minutes and resuspended in 500 µL of Small-Scale Buffer A (2.7 mM KCl, 1.5 mM KH2PO4, 8 mM Na2HPO4, 5 mM DTT, 2 mM PMSF, pH 7.2). The suspension was lysed with lysozyme and three freeze-thaw cycles using liquid nitrogen and a 42 °C water bath. To reduce viscosity, the lysates were treated with Benzonase for 20 minutes at RT and boiled for 20 minutes. The boiled lysates were then centrifuged at 21,000xg for 60 minutes to clear cell debris and precipitated proteins.

The clarified supernatant containing soluble tau was isolated and 100 µL of SP Sepharose resin (GE Life Sciences) was added to it. The suspension was incubated with agitation for 20 minutes at 4 °C. The suspension was added to a 1.2 µm 96-well filter plate (Pall) and vacuum suction was applied to remove flow-through. The resin was washed with 5% Small-Scale Buffer B (2.7 mM KCl, 1 M NaCl, 1.5 mM KH2PO4, 8 mM Na2HPO4, 2 mM DTT, pH 7.2) then 15% Small-Scale Buffer B applying suction each time to remove flow-through. The tau was eluted by adding 35% Buffer B and incubating for 10 minutes then applying suction and collecting the flow-through in a deep 96-well plate. Due to the high concentration of salt in the elution buffer, direct application of the eluate is not amenable for downstream assays as the salt can affect the aggregation reaction and play an inhibitory role. Thus, the purified proteins were buffer exchanged into 1XDPBS+ 2mM DTT with the 3K MWCO filter plates (Pall) by centrifugation at 3,200xg until approximately ¼ volume remained and then approximately three volumes of DPBS was added and

concentrated again in this manner two more times. Quantification of final protein concentrations were obtained with DTT-compatible BCA protein assay (ThermoFisher)

2.6. SDS-PAGE Electrophoresis

Samples to be resolved were prepared by adding SDS Sample Buffer to a 1X concentration (62.5 mM Tris pH 6.8, 10% glycerol, 2% SDS, 5% 2-mercaptoethanol, 0.002% bromophenol blue) and heated to 95 °C for 5 minutes. Samples were loaded onto 12% acrylamide gels or precast 4-20% BioRad TGX™ gels. A constant voltage of 270V was applied to the gel for 25 minutes until the dye front reached the bottom of the gel. The gel was then stained with Coomassie stain (0.5% Coomassie BB, 50% methanol, 10% acetic acid) and then destained by submerging in boiling deionized water for 10-20 minutes until sufficiently destained.

2.7. Aggregation Assay

Tau was diluted to 10 µM in assay buffer (1X DPBS, 2 mM DTT) and induced with 0.04 mg/mL heparin (SantaCruz) in low-binding 1.7 mL microfuge tubes (Denville). Reactions were incubated at 37 °C with shaking at 800 rpm (Benchmark ORBI-Shaker with tube adapters) for 24-48 hours. Once complete, reactions were transferred to non-binding 1.7 mL microfuge tubes (MIDSCI) and stored at 4 °C. To measure thioflavin T fluorescence, reactions were diluted 1:1 with 10 µM ThT in triplicate in a black 384-well plate and read with an excitation wavelength of 444 nm, emission wavelength of 485 nm, and a cut-off of 475 nm.

2.8. Kinetic Assay

All components used in the assay were prepared in assay buffer (1X DPBS, 2 mM DTT) and filtered using a 0.22 µm MCE filter (Millipore). Heparin (SantaCruz) was used

as the aggregation inducer and was made to 0.44 mg/mL and prepared fresh for every assay. The concentration of tau stock solutions was obtained with the BCA Protein Assay (ThermoFisher, Reducing Agent Compatible). The components were mixed in black 96- or 384-well plates in triplicate as follows: 10 µM tau, 10 µM thioflavin T, 88 µg/mL heparin. Assay buffer was added instead of heparin for non-induced controls. The plate was covered with an optically clear film (VWR) and placed in a plate reader to be read with an excitation wavelength of 444 nm, emission wavelength of 485 nm, and a cut-off of 475 nm with intermittent shaking at 37 °C for 120 seconds in a SpectraMax M5 plate reader (Molecular Devices). Measurements were taken every five minutes for 24 hours.

2.8.1. Kinetic Analysis

Resultant curves were plotted using GraphPad Prism software. Curves were treated individually and fit to the following Gompertz growth equation (Necula & Kuret, 2004; Winsor, 1932):

$$Y = A_0 + A_1 e^{-e^{\frac{A_2 - t}{A_3}}}$$

where Y is the fluorescence in raw fluorescent units (rfu) at time t, A_0 is the minimum fluorescence value in rfu for the whole assay, A_1 is the maximum fluorescence value in rfu (maximum amplitude). The lag time is defined as the time it takes for the elongation phase to begin and is calculated by $A_2 - A_3$, in hours. The elongation rate constant is calculated by $\frac{1}{A_3}$, in hr^{-1}. Replicate values for each parameter were averaged. Statistical analysis was done through GraphPad Prism and are outlined in the figure legends where they occur.

2.9. Trypsin Digestion and Capillary Gel Electrophoresis

Tau aggregate solutions were treated with 0.03 mg/mL trypsin (ThermoFisher) in DPBS and incubated at 37 °C for three hours with gentle agitation. Due to the nature of high-throughput analysis utilising smaller sample volumes, a method more sensitive and more reproducible than traditional SDS-PAGE was needed. The ProteinSimple capillary gel electrophoresis system requires very little sample to be resolved and has significantly higher sensitivity than traditional SDS-PAGE staining methods. The digested fibrils were mixed with the ProteinSimple 5X sample buffer, which contains a fluorescent protein standard for calibration, then boiled for 5 minutes. ProteinSimple Wes plates were set up according to manufacturer specifications and 3 μL of digested samples were resolved using the 2-40 kDa Wes capillary cartridges (13 or 25 capillary) and visualised by the ProteinSimple Total Protein Dye. This dye biotinylates all proteins that have been resolved in the capillary and a streptavidin-HRP conjugate binds to the biotinylated proteins and is detected by chemiluminescence.

2.9.1. Trypsin Digest Analysis

Resulting chromatograms representing the protease-resistance segments of the fibril were extracted from the CompassSW software and plotted in GraphPad Prism. To assess the similarities of the digest patterns of different samples, a program based on the GelJ (Heras et al., 2015, https://sourceforge.net/projects/gelj/) was utilised to unbiasedly compare and group samples. All source code for the current version of the program is deposited on GitHub (https://github.com/joheras/TauComparison). The program analyses the digest chromatograms and similarity is determined using a correlation coefficient. The program then groups the samples and outputs a dendrogram. Our analysis used the

Jaccard coefficient which compares the common peaks between two given samples with the peaks that differ. This coefficient can be output as a matrix, or heat map, comparing all analysed samples to each other. Dendrograms were generated by hierarchical clustering in the program using the mean linkage. The samples were then clustered into bins using a threshold of 0.85.

Chapter 3

SCREEN OPTIMISATION

Introduction

In vitro aggregation is a molecular process by which protein molecules self-associate and assemble into higher-order structures. This process can be expedited through the use of chemical inducers. *In vitro* methods provide the user the ability to manipulate the environment and better isolate variables and assess their effects on aggregation. As such, the molecular environment in which this process occurs is highly sensitive. Minor differences in buffer conditions, ionic strength, temperature, protein purity, vessel used, agitation, *et cetera* can have drastic effects on aggregation. An example of this is in a cautionary tale shared by Dr. Sue-Ann Mok where a manufacturer altered their plate composition which caused the previously seen aggregation effects to become inconsistent. So, it is crucial that conditions remain consistent between experiments. I first aimed to purify all six isoforms of human tau protein recombinantly as well as two disease associated mutants. I then characterised their *in vitro* aggregation properties such as their kinetic parameters and protease resistance. This would provide a benchmark to compare future results against by establishing the conditions in which these assays occur.

Results

3.1 Large Scale Tau Purification

Our first objective was to purify the tau isoforms recombinantly by large-scale traditional methods to serve as a baseline to compare against for our high-throughput screen. As tau is a protein that contains several arginine and proline codons with low frequency usage in *E. coli*, a special strain of *E. coli* was used for protein expression. BL21-CodonPlus (DE3)-RP competent cells are an expression strain that carry an extra plasmid containing extra copies of the argU and proL tRNA genes. This increases the availability of rarer tRNAs which would normally pose as a limiting factor during peptide elongation steps of translation. Following expression and lysis of cells transformed with a tau expression vector, tau was purified using column-based affinity purification and resulted in a prominent elution peak, measured by A_{280} values (Figure 3.1A). As tau does not contain any tryptophan residues and has a low amount of tyrosine residues, it has a relatively low extinction coefficient (7450 $M^{-1}cm^{-1}$) which leads to lower A_{280} readings. Eluted fractions covering the tau peak from the chromatogram were resolved by SDS-PAGE and a prominent band at ~60 kDa was seen (Figure 3.1B). It is important to note that the tau isoforms resolve at a larger apparent molecular weight due to their high positive charge. Typical yields ranged from approximately 10-20 mg of purified protein per litre of culture expressed after fractions with highest tau concentration were pooled.

3.2 Aggregate Properties of Tau Isoforms

With an optimised large-scale purification protocol, I endeavoured to purify the six tau isoforms and confirm the effect the sequence differences between them have on

aggregation that has been seen in the literature. Plasmids encoding the six isoforms of tau were generated by cloning the N-terminal inserts into the 0N4R and 0N3R plasmids (described in section 2.1). All isoforms were expressed and purified to >90% purity by comparing the full-length band to any present lower molecular weight bands. Successful cloning was also verified by the stepwise increase of apparent molecular weight when resolved by SDS-PAGE (Figure 3.2). In order to measure the propensity and degree of aggregation among the different isoforms, they were subjected to the thioflavin T assay at 10 μM to assess their aggregation kinetics with the inducer heparin (Figure 3.3A and B). Isoforms that contained the second microtubule repeat (4R) showed significantly lower lag times than those without the repeat (3R), mirroring results shown previously (Zhong et al., 2012). Of the 3R isoforms, greater inhibition was seen as the number of N-terminal inserts increased. 0N3R was the fastest of the three with a lag time of 3.3 hours, followed by 1N3R with a lag time of 12 hours (Figure 3.3C). 2N3R exhibited no detectable aggregation over the time scale of the assay. However, 2N3R does eventually aggregate when incubated for longer periods of time (>48 hours). I saw a similar, albeit significantly less pronounced relationship in the 4R isoforms where a subtle increase in lag time was observed as more N-terminal inserts are included with lag times of 1.2 hours, 2.2 hours, and 2.7 hours for the 0N4R, 1N4R, and 2N4R isoforms respectively.

Differences in folding structure and core packing of fibrillar aggregates can be assessed with trypsin digestion due to their protease resistant nature. Trypsin digestion cleaves after all accessible lysines lying outside of the fibril core. Upon treatment with SDS sample buffer and boiling, the protected peptide fragments in the fibril core unfold and can be resolved using SDS-PAGE. This technique was used to determine the

structural differences of the aggregated isoforms. I verified that the unaggregated tau monomer does not exhibit any resistance to trypsin and is completely digested into peptide fragments smaller than 5 kDa, leaving only trypsin which can be seen at 23 kDa. (Figure 3.4, far right lane). Tau that was induced to aggregate was treated with trypsin and when resolved by SDS-PAGE, multiple molecular weight bands between 9 and 25 kDa can be seen which were not present in the unaggregated control lane. The 4R isoforms exhibited the same fragment pattern upon digestion, suggesting they form the same fibrillar structure. The 3R isoforms exhibited similar banding patterns with subtle differences in relative band intensity. The significance of the differences in intensity are unclear. These results match the aggregation kinetic results where the 4R isoforms exhibited similar properties and the 3R isoforms were slightly varied.

3.3 Bacterial Peptide Aggregation Inhibitor

New methods for expressing and purifying many tau mutants in high throughput needed to be optimised in order to carry out the mutagenesis screen. It was previously reported that tau protein present in minimally processed bacterial lysate after expression in *E. coli* was sufficient for *in vitro* aggregation studies and did not behave differently from tau purified by additional common chromatography-based purification techniques such as size exclusion, Nickel affinity, or phosphocellulose affinity with respect to their *in vitro* aggregation kinetics. (KrishnaKumar & Gupta, 2017). Their purification method requires only boiling the cells as a method of lysis and removing the cellular debris by centrifugation. Further lysis of cells is also achievable by treating with lysozyme (Figure 3.5A). Following centrifugation, the clarified tau is present in the supernatant. I next sought to validate this reported simplified purification method.

Expression and purification by boiling in a small scale yielded relatively pure tau with average yields of 75 µg per millilitre of expression culture (Figure 3.5B). Upon boiling, lysozyme does not remain in the supernatant and is undetectable by SDS-PAGE (Figure 3.5B). As lysozyme has been shown to form amyloidogenic structures, I performed two control experiments using our *in vitro* kinetic aggregation assays. Lysozyme alone or in the presence of our tau aggregation inducer, heparin, did not produce any ThT fluorescence signals in our standard assay (Figure 3.6A). The addition of increasing amounts of lysozyme to our standard tau aggregation assay also did not significantly alter tau (10 µM) aggregation kinetics when up to 6.25 µM of lysozyme was added (Figure 3.6B) suggesting that any residual lysozyme in our purified tau samples would not affect our assay results.

Interestingly, the crude lysate, while containing sufficient protein yield for kinetic analysis, did not produce the expected aggregation curve in our kinetic aggregation assay (Figure 3.7A). There appeared to be a hockey stick-shaped curve with the highest fluorescence signal (~800 rfu) occurring within the first hour and then tapering off to a baseline with very high background signal (~200 rfu). I attempted to isolate the component of the lysate that was preventing aggregation from occurring as well as contributing to high background by performing size exclusion chromatography. Crude tau lysate was purified, and the elution profile revealed fractions that had high A_{280} readings near the end of the run (Figure 3.8A), which correspond to molecules with molecular weights <10 kDa. These fractions also exhibited a yellow tint whereas all other fractions were colourless. When fluorescence of the fractions was assessed with an excitation wavelength of 444 nm and detecting and emission wavelength of 485 nm (the fluorescent profile of thioflavin

T bound to amyloid), the fractions that corresponded to a high A_{280} signal and <10 kDa in size also exhibited high fluorescence, with the highest fluorescent signal coming from fraction 45 (Figure 3.8B). Due to the small apparent size of the components of this fraction, MALDI-TOF was used to get an accurate measure of the molecular weight. Two major peaks were seen with mass to charge ratios of 1582.9 and 1612.9 (Figure 3.9).

To measure the inhibitory effects of this molecule, 10 µM tau was aggregated in increasing amounts of the fraction with the highest fluorescence (fraction 45) and the degree of aggregation was measured by thioflavin T reactivity. Increasing amounts of fraction 45 present in the reaction led to a decrease in thioflavin T fluorescence (Figure 3.10A). To rule out the possibility that fraction 45 was simply affecting the interaction of the thioflavin T dye with the aggregates, the reactions were tested for their protease resistance and resolved by SDS-PAGE. When fibrils generated in the absence of fraction 45 were digested, the characteristic banding pattern of tau aggregates established in the previous section was seen (Figure 3.10B). However, as fraction 45 was introduced to the reaction the bands became less and less intense with increasing amounts of fraction 45, suggesting the formation of the protease-resistant fibrils is being inhibited. This indicates a dose-dependent inhibitory effect of fraction on aggregation.

3.4 Optimised High-Throughput Tau Purification and Fibrillisation Protocol

Our discovery of an aggregation inhibiting peptide in crude bacterial lysate necessitated further purification of the protein extracts to allow for fibrillization. The two options were to use a scaled down version of the cation exchange affinity purification used in the batch purifications as in section 3.1 or to utilise the His-tag that exists on the

47

expressed tau and capture it using His-binding resin (e.g., Ni-NTA). First, I tested whether the imidazole used in the elution of His-tagged proteins from Ni-NTA resin would have an effect on aggregation, as it would remain in the eluate and be present in downstream assays. Tau was incubated in varying concentrations of imidazole after induced with heparin for 24 hours and thioflavin T measurements were taken. The presence of imidazole in the reaction led to a decrease in thioflavin T signal indicating a reduction in aggregation (Figure 3.11). The presence of as little as 50 mM imidazole was enough to inhibit tau aggregation. Since the typical concentration of imidazole in elution buffers ranges from 200-350 mM, this made Ni-NTA resin an unsuitable candidate for downstream applications.

The other candidate method for purification was cation exchange chromatography. A scaled down form of the purification using 96-well plates and microfuge tubes was optimised (Figure 3.12, described in Materials and Methods) and found to yield sufficiently pure tau at yields of approximately 7 µg per millilitre of culture (Figure 3.13). The tau purified by this method was also able to aggregate in the thioflavin T assay (Figure 3.14A). However, it was noted that the ΔK280 mutant, which was shown previously to be the fastest aggregating mutant when induced with heparin (Kumar et al., 2014), showed little to no aggregation (Figure 3.14A). The salt concentration used in the elution buffer is higher than that used in kinetics assays from previous studies, so I tested whether the increased salt was having a confounding effect. Indeed, when ΔK280 was aggregated in increasing salt concentrations, there was a decrease in aggregation as the salt concentration went up (Figure 3.14B). Aggregation was almost completely ablated at 250 mM NaCl. This suggests some mutants may be particularly sensitive to the buffer

environment as compared to others. A panel of disease associated mutants was expressed and purified on a small scale in duplicate and aggregated in elution buffer (high salt) or buffer exchanged into DPBS and aggregated in DPBS (standard salt). The lag times when normalised to WT revealed four mutants that had a statistically significant difference between the conditions (Figure 3.15). Those mutants are ΔK280, L284R, ΔN296, and E342V. ΔK280 showed an increase in lag time (reduction in aggregation propensity) in high salt conditions however, the other three showed a decrease in lag time (increase in aggregation propensity). So as to remove this variable from analysis, a buffer exchange step was introduced into the workflow to reduce the salt in the buffer. This brought the results back in line with previous results I and other labs have found (Figure 3.15). Introducing this step also allowed for less variability in the aggregation kinetics (Figure 3.15) which allowed us to scale down the assay even further to a 384-well plate, increasing the number of mutants that can be processed at one time and strengthening the fidelity of the assay.

3.5 Trypsin Digestion and ProteinSimple WES Optimisation

As described in section 3.2, trypsin digestion of aggregated tau is a way to assess structural variation between samples. I sought to utilise this feature to provide structural information in the mutant screen that is also amenable to high-throughput applications. The Wes by ProteinSimple is an automated capillary gel electrophoresis system that resolves protein samples based on molecular weight and can be detected by immunological staining or total protein, similar to traditional SDS-PAGE and Western blotting methods. The benefits of this system are that it allows for more consistent data between experiments with the use of internal molecular weight standards as well as the

digitization of the data which allows us to analyse the data algorithmically in an unbiased manner.

Firstly, the length of time for the trypsin digestion needed to be established. Fibrils were subjected to a trypsin treatment at a ratio of 1:20 enzyme:fibril at varying times (1, 3, 5, and 24 hours) and then resolved with the Wes and visualised using the total protein method. The resulting banding pattern remained largely unchanged over the 3-24 hour time points aside from a slight decrease in overall signal intensity (Figure 3.16). Trypsin itself does not produce a significant signal by the total protein reagent likely because the lysine residues on the trypsin protein have been modified to prevent autolysis which inhibits the biotinylation reactions used to detect the peptides. With considerations of time and stability of digestion, a reaction length of three hours was used for all fibril digestions except where otherwise stated.

To assess whether the fragment patterns would be resolved consistently between experiments and could be standardised, three separate fibril preparations were digested with trypsin as described above and resolved using the Wes with the total protein detection. The three preps all exhibited the same banding pattern with peaks at 10, 17, and 29 kDa (Figure 3.17). This suggested that the Wes is capable of reliably and reproducibly resolving the digestion reactions and allows for more thorough and streamlined analysis with the assistance of gel banding analysis software such as GelJ (Heras et al., 2015). The Wes is also capable of resolving 72-96 samples in one day making it perfectly compatible with our high-throughput assays.

Our workflow involves digesting the aggregates derived from the kinetic assay, so it was crucial to know whether the conditions of the assay (presence of thioflavin T and the plate used) had any confounding effect on the structure of the fibrils produced. I expressed two common tau mutants, N279K and P301L, and aggregated them in a plate and a microfuge tube, both in the presence and absence of thioflavin T. The aggregates were treated with trypsin and resolved by the Wes. The resulting banding pattern did not change significantly for any of the conditions tested (Figure 3.18). This suggests that the conditions of the kinetic assay have no effect on the final fibril structure and any differences between mutants would be solely because of the point mutation.
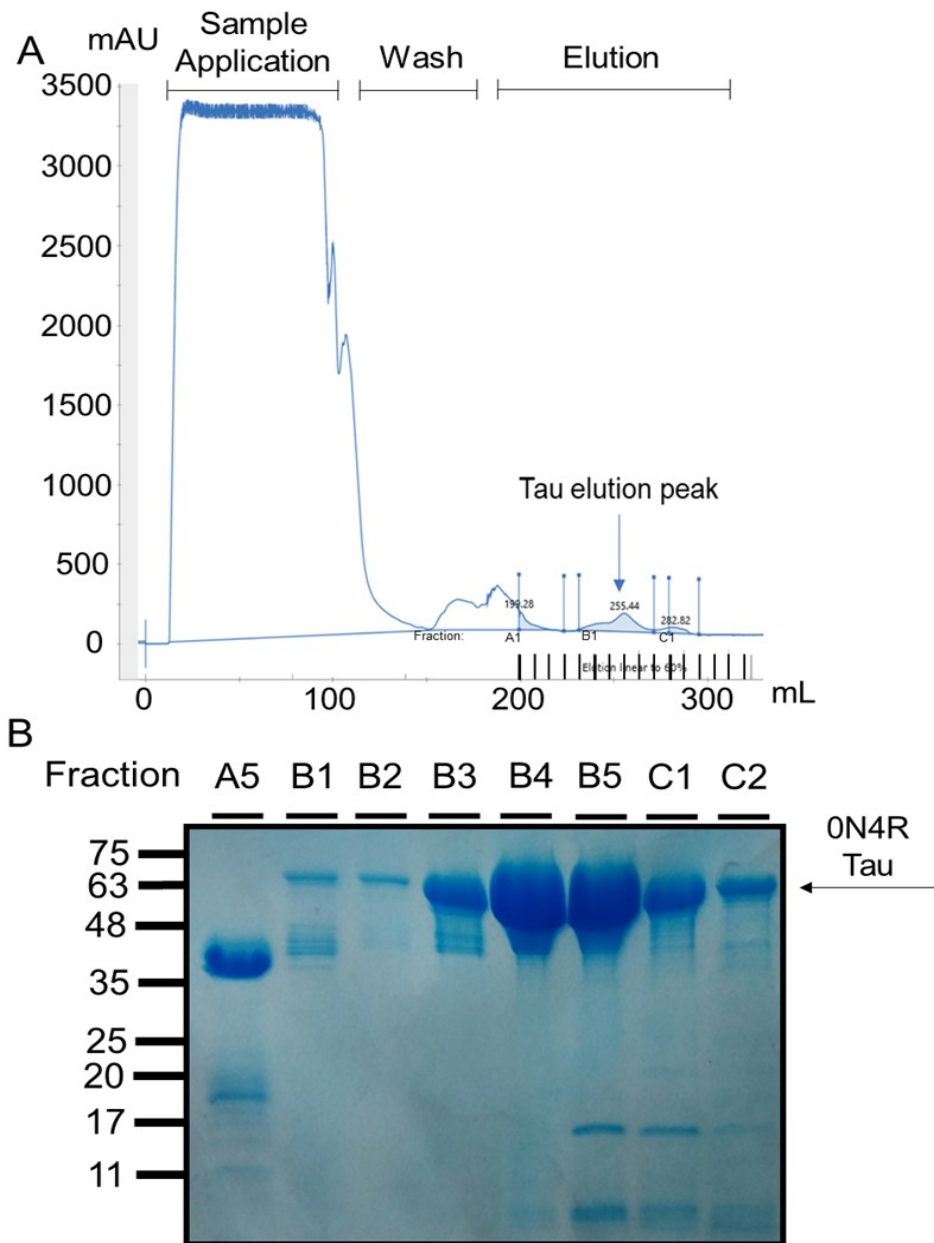
Figure 3.1: **Representative chromatogram and gel of tau purification by cation exchange chromatography.** *A.* Representative chromatogram of purification process of tau bacterial lysate with A_{280} values graphed by volume applied to column. Major purification steps and fractions are indicated. *B.* SDS-PAGE of selected fractions from purification as indicated in A. Note that tau's overall high positive charge causes it to run at a higher apparent molecular weight (~58 kDa for 0N4R).
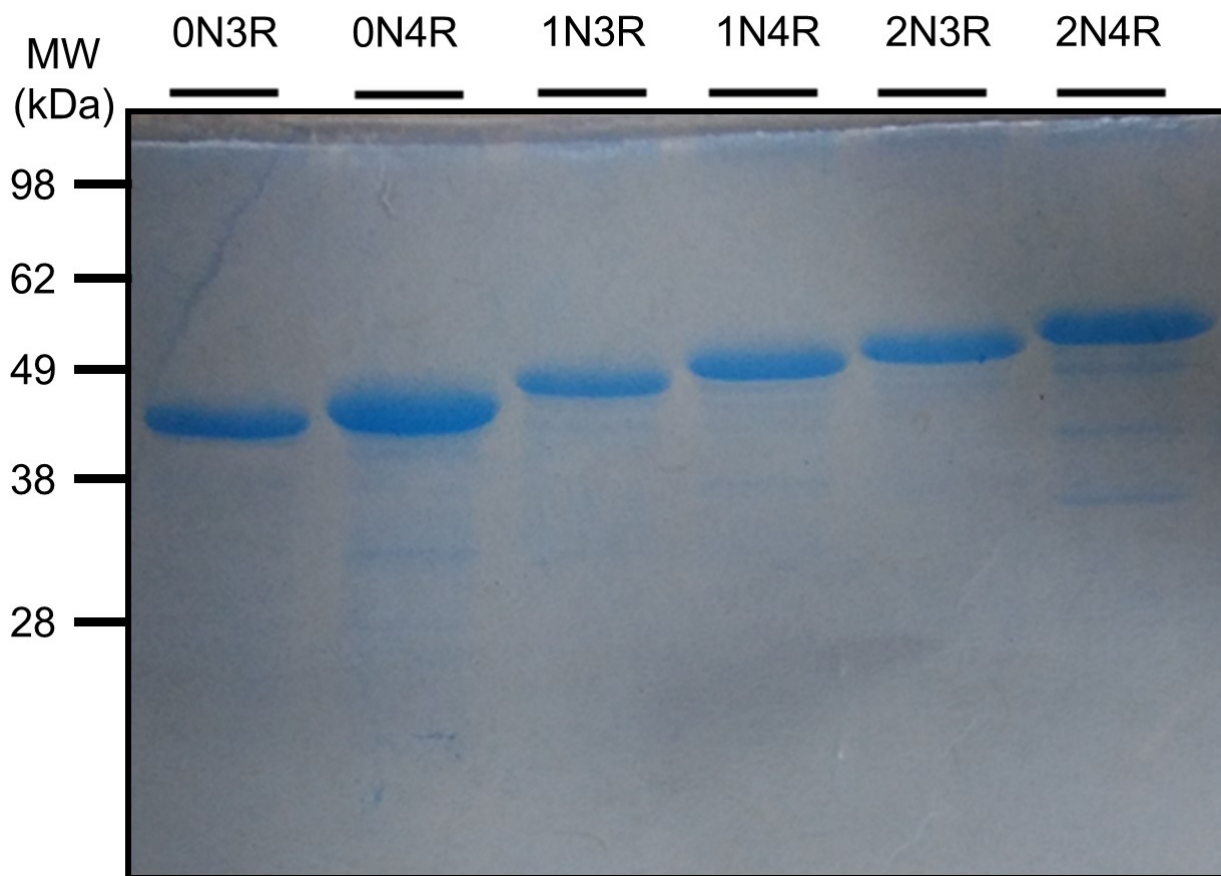
Figure 3.2: **Purified Tau Isoforms.** The six tau isoforms were purified as described by cation exchange and purified samples were resolved by SDS-PAGE. Tau's high overall positive charge gives it a higher apparent molecular weight to the same relative amount for the isoforms.
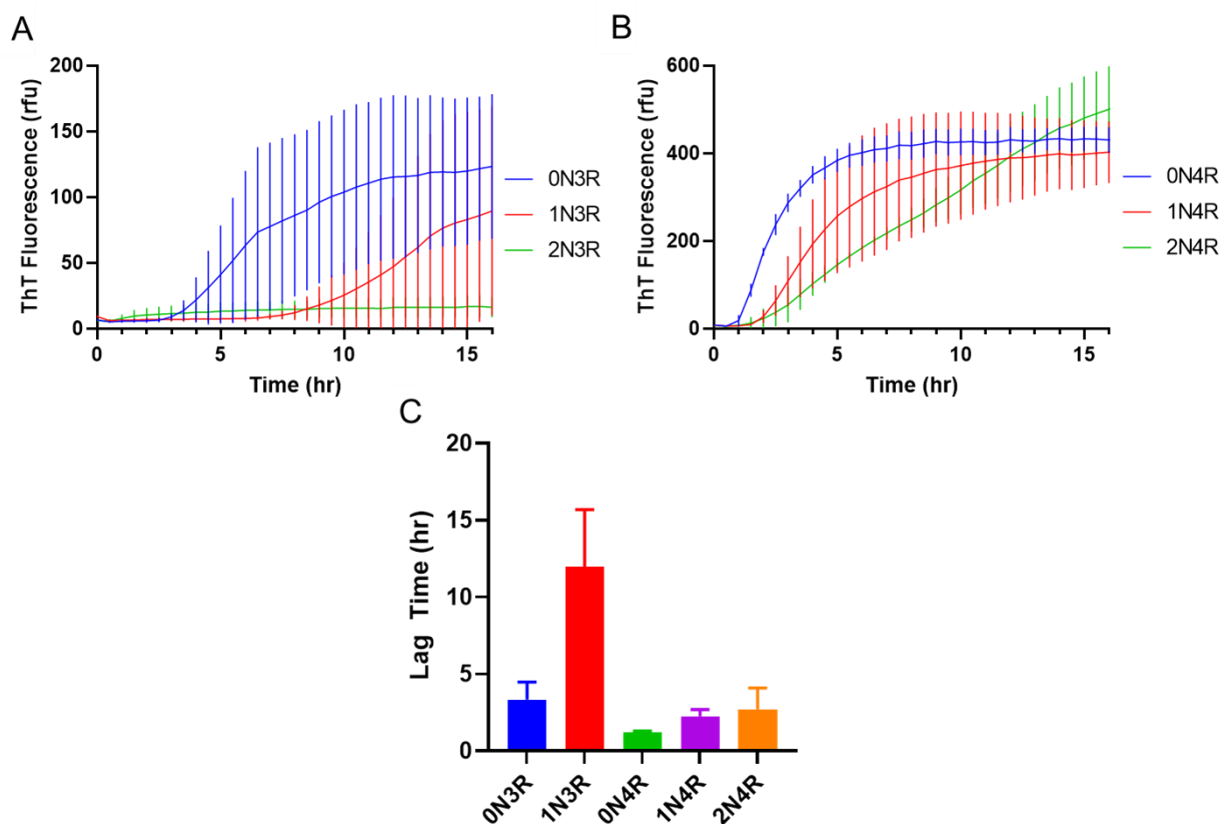
Figure 3.3: **Presence of R2 confers greater aggregation propensity in tau.** Tau isoforms (*A*: 0N3R, 1N3R, 2N3R *B*: 0N4R, 1N4R, 2N4R) were aggregated at 10 μM by the addition of the inducer heparin and the aggregation reaction was monitored by thioflavin T fluorescence every five minutes. Values are averages of three replicate reactions ± SD. *C*. Curves from individual replicates were fitted with a nonlinear regression as described in section 2.8.1. Lag times were calculated from the regression and values represent averages of three replicate reactions ± SD. Results representative of three independent experiments.
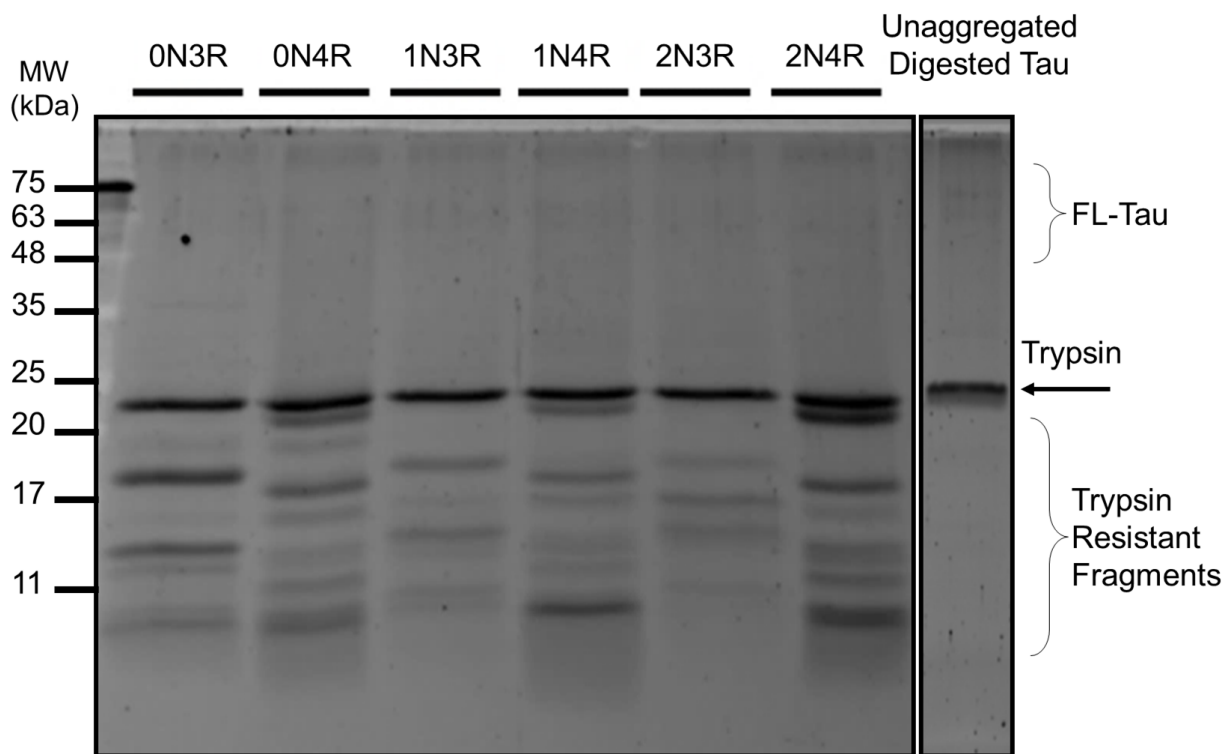
Figure 3.4: **Trypsin digestion patterns of six tau isoforms.** Tau isoforms (10µM) were aggregated by the addition of the inducer heparin. Resultant aggregates were digested with trypsin at a 1:20 enzyme:protein ratio for 3 h, at 37 °C and resolved by SDS-PAGE stained with SYPRO™ Ruby Protein Gel Stain. The panel on the right is the digestion of unaggregated monomeric tau protein. The migration of full-length tau (FL-tau), trypsin, and trypsin resistant fragments are indicated. Results representative of two independent experiments.
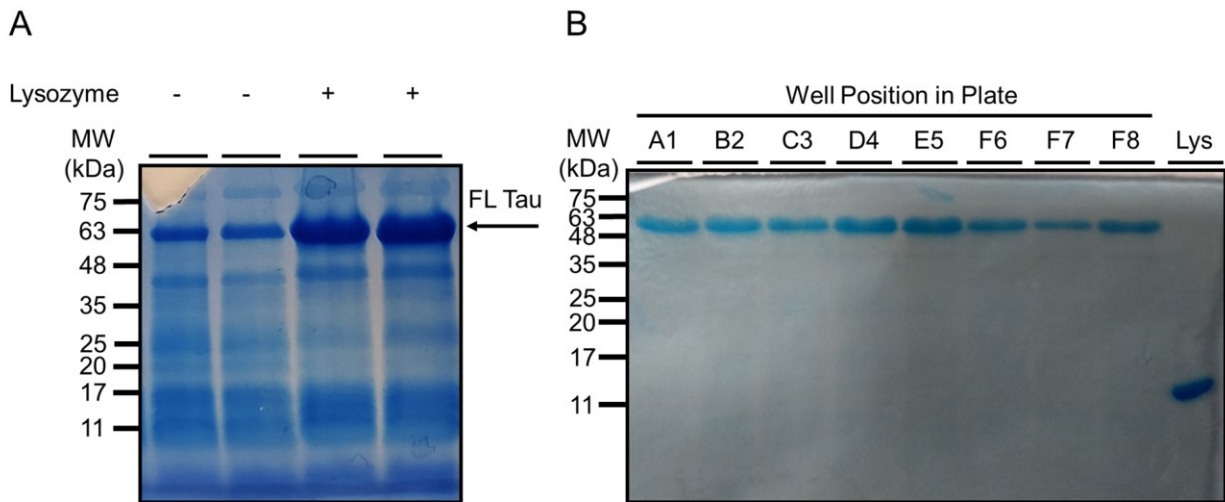
Figure 3.5: **Lysozyme aids in cell lysis.** *A*. Tau (0N4R) was expressed in 40 mL *E. coli* cultures and resuspended cells were either treated without (left two lanes) or with (right two lanes) lysozyme in duplicate. Samples were then boiled for 20 minutes and centrifuged to remove cell debris. Clarified supernatants were resolved by SDS-PAGE. Results representative of two independent experiments. *B*. Tau (0N4R) was expressed in 3 mL cultures in a 48-well plate and lysed with lysozyme and direct boiling. The lysates were clarified by centrifugation and the supernatants were resolved by SDS-PAGE. A clear band corresponding to the tau protein is seen at ~58 kDa. In the far-right lane, a sample of lysozyme was loaded to demonstrate that it is not detected in purified tau samples.
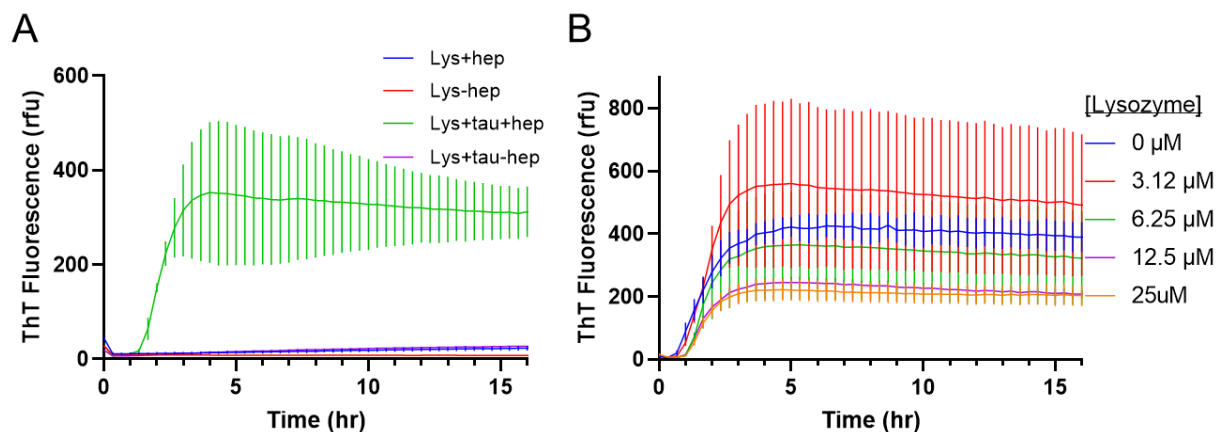
Figure 3.6: **Residual lysozyme does not significantly alter aggregation kinetics of tau.** *A.* Lysozyme (65 µM) was aggregated with or without tau with the inducer heparin and monitored by ThT. Results shown are averages of three replicate reactions ± SD. *B.* Large-scaled purified 0N4R tau was aggregated in the presence of indicated concentrations of lysozyme and monitored by ThT with readings being taken every 5 minutes. Results shown are averages of three replicate reactions ± SD. Results representative of one independent experiment.
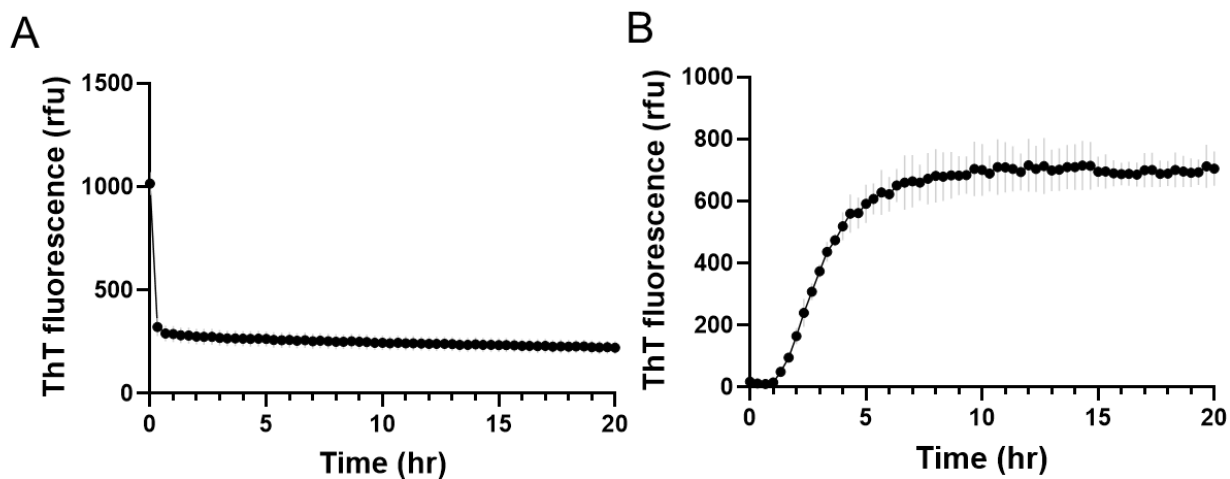
Figure 3.7: **Kinetic curves of purified tau versus directly boiled tau.** *A.* Expressed 0N4R tau was purified by the simplified method of boiling lysis and centrifugation (KrishnaKumar & Gupta, 2017). The clarified lysate containing tau was directly used in a kinetic assay induced with heparin and monitored by ThT fluorescence over 24 hours. Results shown are averages of three replicate reactions with standard deviations, representative of three independent experiments. B) For comparison, the kinetic assay results of large-scale purified tau aggregated with the same conditions as in A, is plotted.
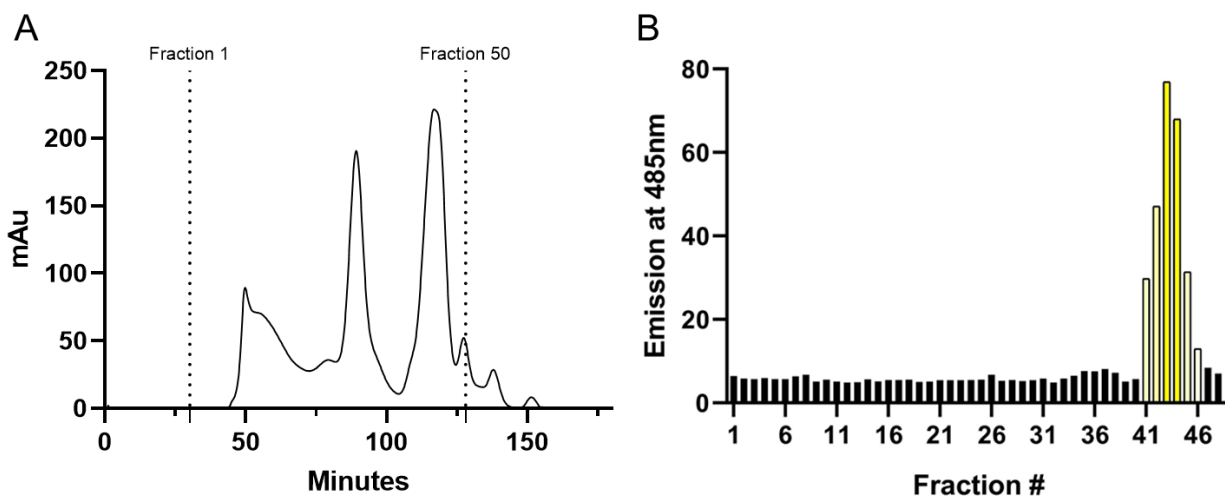
Figure 3.8: **SEC chromatogram of clarified tau bacterial lysate and fluorescent measurements of eluted fractions.** *A*. Tau was expressed in *E. coli* and lysed as described in section 2.4. The clarified lysate was then resolved by size-exclusion chromatography using a HiLoad 16/60 Superdex 200 prep grade and 2 mL fractions were collected, with the 1st and 50th fraction times indicated. Highlighted fractions (1-50) were used for further analysis. *B*. Selected fractions from *A* were measured for fluorescence with an excitation wavelength of 444 nm and an emission wavelength of 485 nm. Fractions exhibiting higher fluorescence are coloured yellow to reflect their yellow tint.

m/z	Intens.	Area	S/N
609.030	1672	5634	3
659.488	1645	6039	3
675.547	2153	8323	4
951.473	21559	91627	8
961.184	20247	30408	6
967.409	21475	52731	5
984.221	22444	66655	5
999.826	18645	48962	3
1010.960	19881	51279	4
1026.464	24582	96654	6
1034.763	24110	57479	6
1050.684	28731	149831	9
1066.973	28740	80802	9
1072.793	27833	55767	9
1080.870	19404	61125	4
1089.680	28512	111823	9
1111.085	21098	60210	5
1237.683	27564	71964	8
1253.222	31647	70329	10
1383.592	34334	72273	11
1399.552	45818	94266	17
1405.774	26422	50607	8
1421.794	30814	80714	10
1483.800	23665	60223	6
1582.944	26156	65719	8
1596.942	635349	2.034476e6	281
1612.931	812721	2.817631e6	364
1635.013	156273	551550	68
1653.482	47181	284849	18
1669.957	33005	156407	12
1682.661	65489	294918	28
1698.171	88868	328479	41
1720.344	20804	74165	6
1742.147	14822	35801	3
1768.109	16631	32851	5
1784.199	20975	48687	7

Figure 3.9: **MALDI-TOF of Fraction 45.** Clarified tau lysate was purified by size exclusion chromatography and eluted fraction 45 was diluted 1:100 with 50% acetonitrile and 0.1% trifluoroacetic acid. The diluted sample was spotted onto a matrix plate and allowed to dry. The plat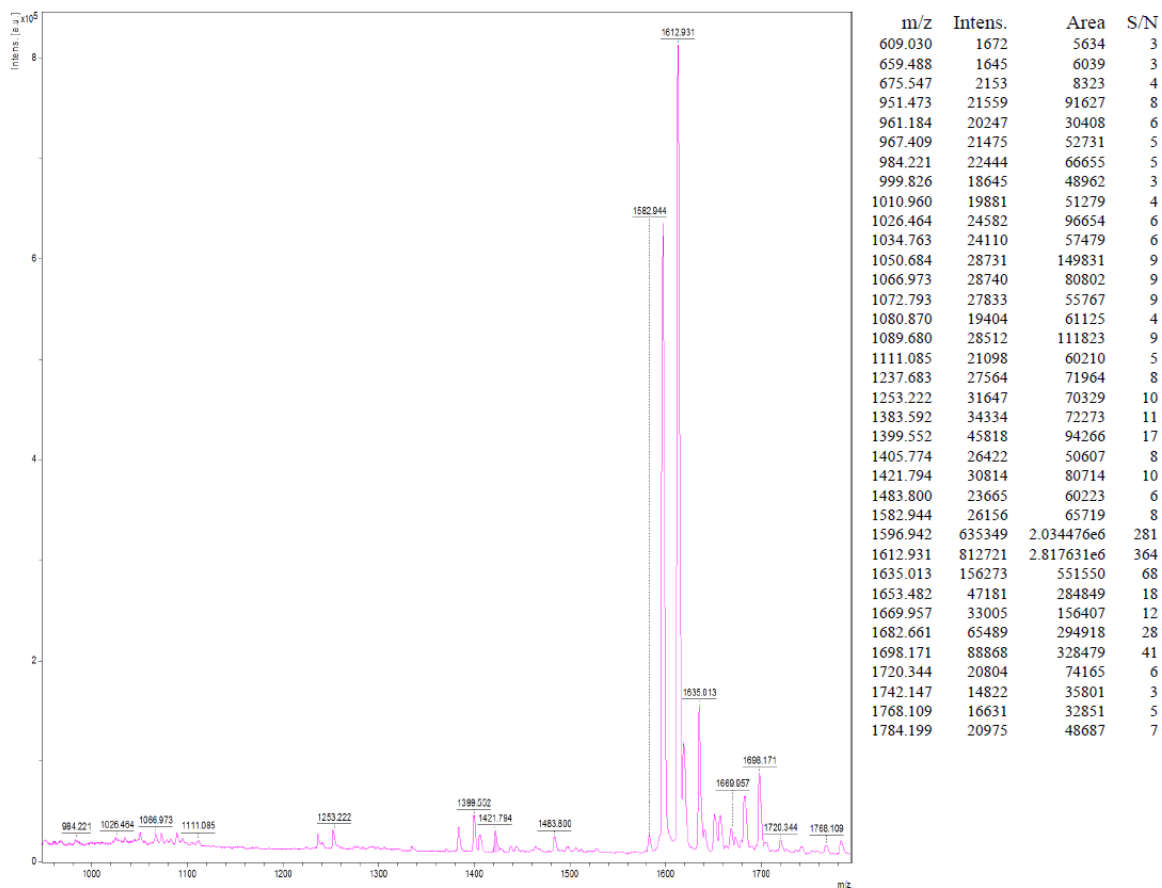e was then placed into the autoflex™ speed MALDI-TOF machine and the spectrum was obtained. Two major peaks could be seen at 1583 kDa and 1613 kDa.
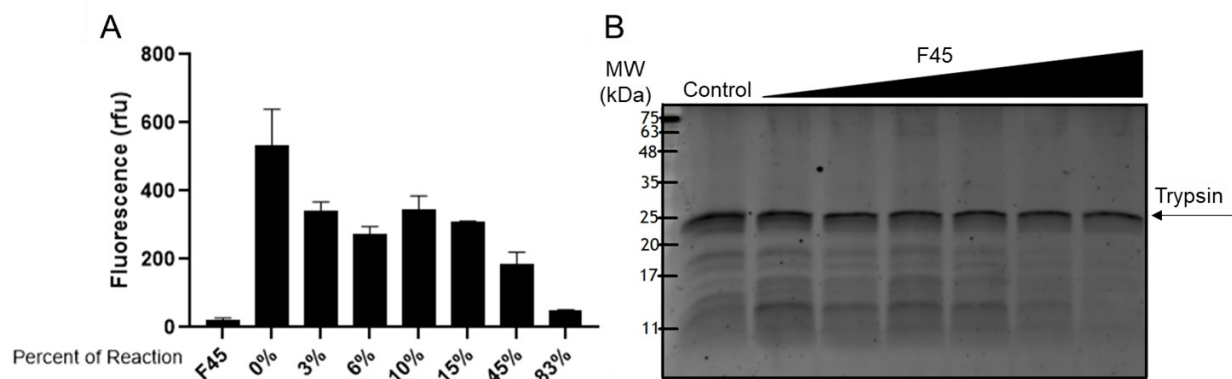
Figure 3.10: **Fraction 45 has a dose-dependent inhibitory effect on tau aggregation.**
A. Tau was aggregated in the presence of heparin and increasing amounts of fraction 45 from SEC purified tau bacterial lysate, as indicated. The fractions were then mixed with 5 µM Thioflavin T and the fluorescence was measured. Data is averages of three replicate measurements representing one independent experiment. *B.* The reactions from A were treated with trypsin and incubated for three hours. Control refers to the reaction with no fraction 45 (0%). The digests were then resolved on a 15% SDS-PAGE gel and stained with SYPRO™ Ruby Protein Gel Stain. The band corresponding to trypsin is highlighted.
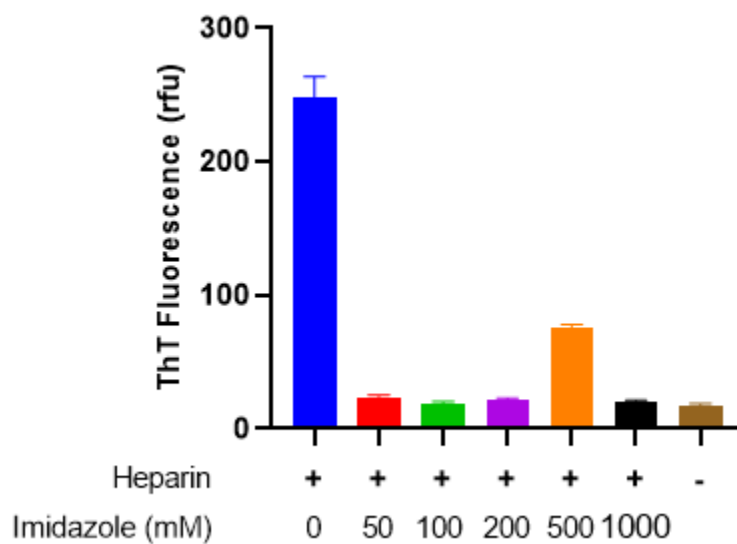
Figure 3.11: **Effect of imidazole on tau aggregation.** Tau was incubated with the indicated concentrations of imidazole and induced to aggregate with heparin. The degree of aggregation was measured with thioflavin T after 48 hours. Data shown is averages of three replicate measurements ± SD, representing one experiment.
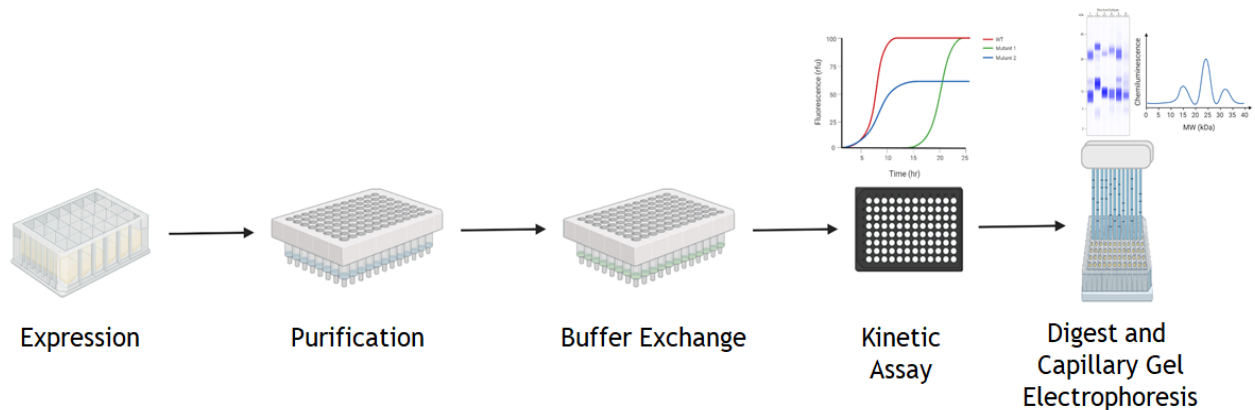
Figure 3.12 **Optimised workflow for small-scale tau purification and aggregation analysis.** The protocol used in this project to purify tau variants and assess kinetic and structural information was optimised as described in section 3.4 and 3.5. Tau variants are expressed in deep-well plates. Cells are then lysed and clarified by centrifugation. Tau is then purified from the supernatant using cation exchange resin (Capto™ SP ImpRes) and buffer exchanged using 96-well filter plates into commercial DPBS to remove excess salt. Buffer exchanged tau is then assayed for aggregation kinetics followed by digestion with trypsin and resolved by capillary gel electrophoresis.
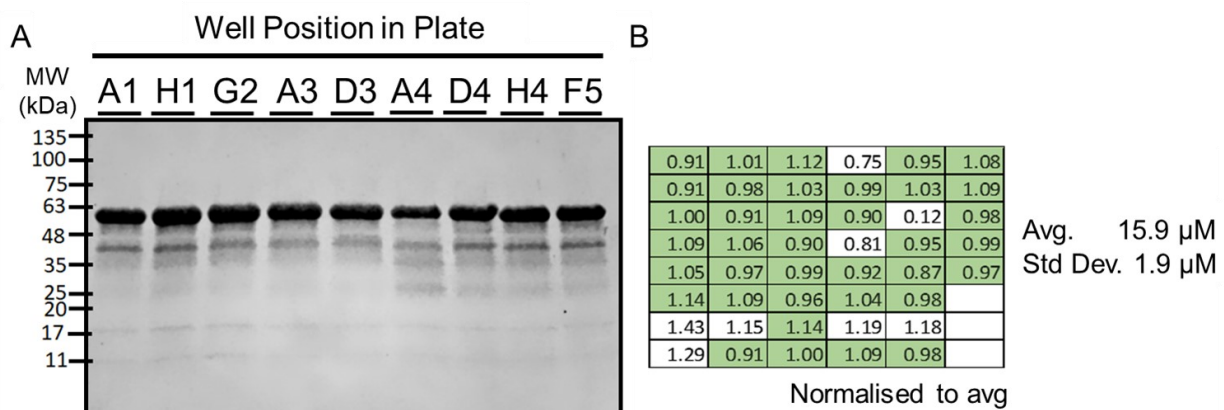
Figure 3.13: **Purity and yield of small-scale purified tau mutants.** *A*. A panel of tau mutants were expressed and purified using the optimised small-scale protocol. Select tau mutants were resolved by SDS-PAGE to assess purity. *B*. A BCA assay was performed on the panel to obtain yield. Calculated concentration values are normalised to the plate average (set to 1.00) to demonstrate deviation of individual wells. The average concentration of purified samples was 15.9±1.9 µM, or 275 µg in total per mutant. Highlighted cells are within one standard deviation of the average.
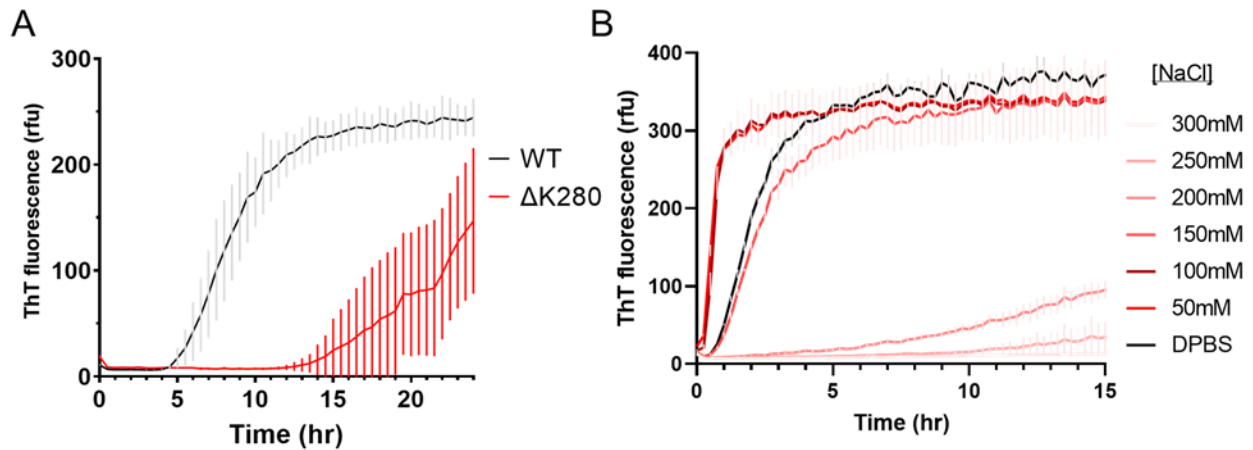
Figure 3.14: **Kinetic assay of ΔK280 in varying concentrations of NaCl.** *A.* WT and ΔK280 tau were expressed and purified in small scale as described in section 2.5 and aggregated at 10 μM with the inducer heparin monitored by ThT. Data shown is averages of three replicate reactions ± SD, representative of four individual experiments. *B.* ΔK280 tau was aggregated (10 μM) in the presence of indicated concentrations of NaCl induced with heparin and monitored over time with thioflavin T. Data shown represents averages of three replicate reactions ± SD, representative of two individual experiments. Note the black line represents aggregation done in commercially obtained DPBS.
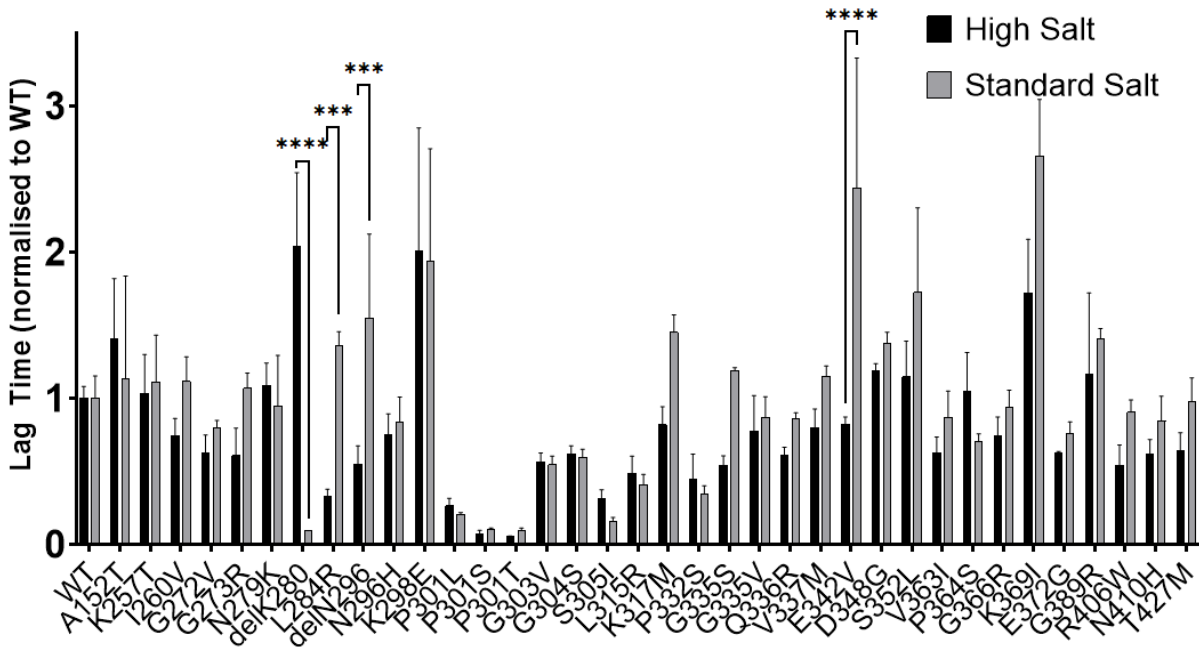
Figure 3.15: **Effect of salt concentration on aggregation lag time is mutant dependent.** Thirty-seven disease-associated tau variants were expressed and purified small-scale and either used directly in elution buffer (high salt) or buffer exchanged into commercial DPBS (standard salt). The mutants were aggregated with heparin and monitored with ThT. The resultant curves were analysed as described in section 2.8.1 and lag times were calculated for each of three replicate reactions and normalised to WT to account for variations in absolute lag time and averaged. A two-way ANOVA was performed on the normalised lag times with Šídák's multiple comparisons test to compare mutants and salt conditions, ***P=0.0002, ***P<0.0001. Results representative of two independent experiments.
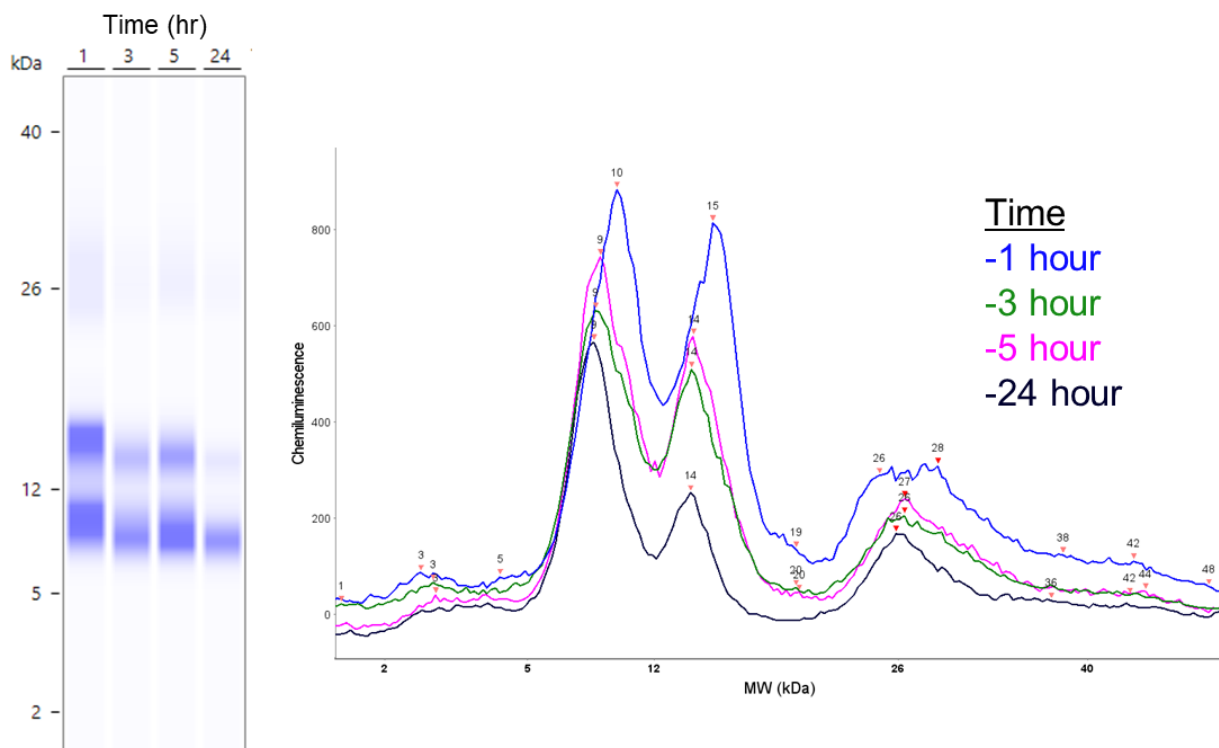
Figure 3.16: **Trypsin digestion time course of WT tau fibrils**. WT tau fibrils induced with heparin were treated with trypsin at a 1:20 enzyme:protein ratio for indicated times. At each time point, the corresponding reaction was frozen to stop the digestion. Once complete, the reactions were resolved by the ProteinSimple capillary gel electrophoresis system using total protein detection. The signal is represented as a virtually generated gel view on the left and a chromatogram on the right a. The solvent-accessible fuzzy coat is digested away and the protected fragments from the fibril core are resolved to generate a banding pattern dependent on the specific core packing. Results representative of three independent experiments.
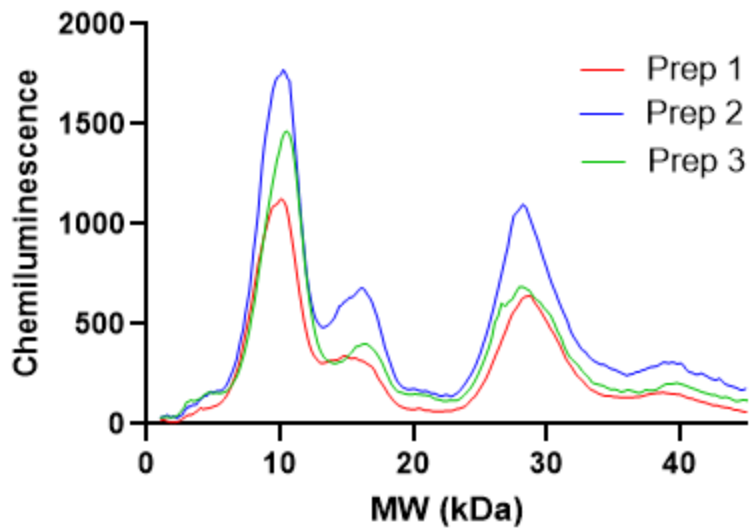
Figure 3.17: **Digestion of fibrils with trypsin yields consistent and reproducible results.** WT 0N4R tau was aggregated with heparin as a cofactor on three separate days (preps 1, 2, and 3). The resultant aggregates were treated with trypsin at a 1:20 enzyme:protein ratio for 3 hours at 37 °C and resolved by capillary gel electrophoresis. The peaks in the chromatogram represent the sizes of the remaining fragments that are resistant to protease digestion. The three separate preps results in comparable banding patterns indicating a high degree of reproducibility in the trypsin digest and gel electrophoresis.
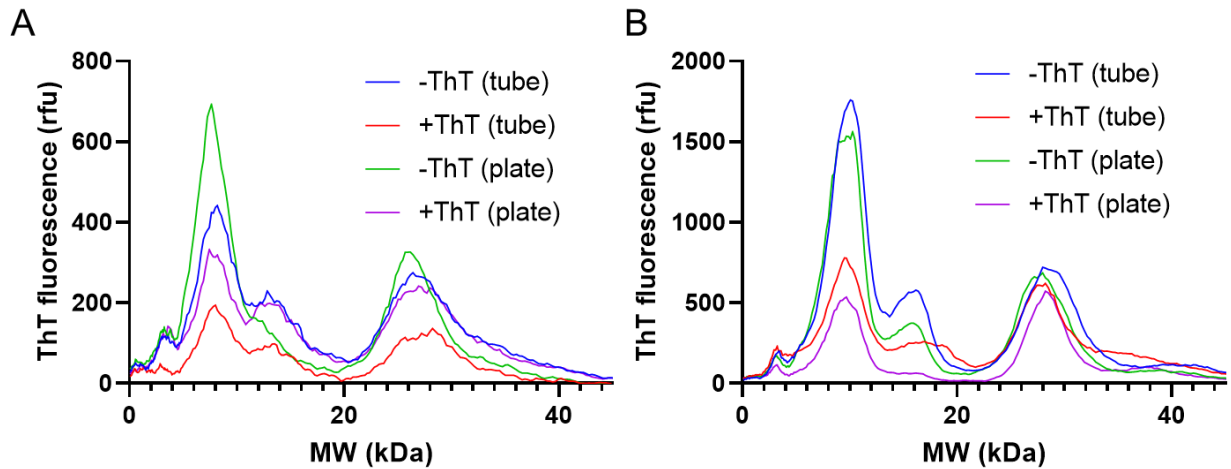
Figure 3.18: **Presence of Thioflavin T in assay does not affect final aggregate structure.** N279K (A) and P301L (B) tau was aggregated in the presence or absence of ThT in microfuge tubes or a black plate used for kinetic assays. The reactions were then treated with trypsin as described in section 2.9 and resolved by capillary gel electrophoresis. Results representative of one independent experiment.

Chapter 4

FAMILIAL MUTANT TAU SCREEN

Introduction

The primary aim of this project was to establish a protocol for purifying tau in high-throughput and to apply that protocol for a mutagenesis screen. As missense mutations in tau have been described and found in tauopathies, I used these mutations as a preliminary screen to assess the robustness of our protocol. I provide a comprehensive study of the structural and kinetic properties of aggregates generated by disease-associated tau mutants, which have only been partially characterised previously. Biochemical data for disease-associated tau mutants is disparate within the literature and herein I describe a way to better standardise assaying the properties of these aggregates.

Results

4.1 Kinetic Parameters of Disease-Associated Mutants

With our high-throughput tau purification protocol, I next sought to directly compare the biochemical and structural properties of tau mutants. There are >30 point mutations in tau that are associated with disease in FTLD-tau (Strang et al., 2019) so I chose that as a starting point to test the robustness of our protocol. This would also contribute valuable biochemical information for how these tau mutants behave *in vitro* compared to the existing literature. I assembled a panel of 36 tau variants comprising disease-associated mutations in the context of the 0N4R isoform using site-directed mutagenesis. The mutant tau proteins were expressed and purified using the small-scale protocol optimised in section 3.4 (Figure 3.13). Purified tau variants were aggregated *in vitro via* the addition of the standard aggregation accelerant heparin (Ahanger et al., 2021) and aggregation kinetics were monitored in the presence of Thioflavin T (Gade Malmos et al., 2017). The aggregation curves generated in the ThT assay were analysed by nonlinear regression (described in 2.8.1) to calculate the lag time, elongation rate constant, and amplitude. For the fitted parameters of the 36 mutants, I observed that most mutants did not statistically differ from WT (Figure 4.1). There were seven mutants that exhibited significantly faster lag times than WT (ΔK280, P301L, P301S, P301T, S305I, L315R, and P332S) and four mutants that had slower lag times than WT (K298E, E342V, S352L, and K369I) (Figure 4.1A). For the elongation rate constant, the only statistically significant shift was an increase in eleven mutants (ΔK280, ΔN296, P301L, P301S, P301T, G304S, L315R, P332S, Q336R, E372G, and R406W) (Figure 4.1B). There were seven mutants that exhibited significantly increased amplitudes (G272V, ΔK280, P301L, P301T, G304S,

S305I, and G335V) (Figure 4.1C). These results match previously reported results for select mutants (Combs & Gamblin, 2012; Goedert et al., 1999). Some of the mutants that promoted aggregation (short lag times) also had an increased final amplitude of the curve (ΔK280, P301L/T, and S305I) however G304S, G335V, and most significantly G272V showed increased amplitudes yet did not have significantly different lag times when compared to WT. None of the mutants tested exhibited significantly decreased elongation rate constants or amplitudes compared to WT. The kinetic aggregation experiment was carried out twice using different batches of purified mutant proteins. When the results were plotted against each other, the data showed a strong correlation between mutants analysed from different preparations with respect to calculated lag time and elongation rate constant values (Figure 4.2A and B) with a p-value less than 0.0001 and an R^2 value of 0.85 and 0.69, respectively. This indicates a high degree of reproducibility for the kinetic assay. In contrast, there appeared to be no significant correlation for amplitude values between experiments (Figure 4.2C). There were two mutants (G272V and ΔN296) that yielded consistent and reproducible lag times and elongation rate constants however they showed extreme variability in the amplitude. This may be due to these mutants exhibiting more heterogeneity in fibril packing and therefore potentially having multiple folding pathways it can go down leading to differences in how the ThT interacts with it resulting in varied fluorescence.

When the kinetic parameters (lag time, elongation rate constant, amplitude) for individual mutants are graphed on the same plot, there appears to be three major populations (Figure 4.3). There is 1) a WT-like cluster, 2) a cluster with significantly slower kinetics (low lag times and elongation rate constants) than WT yet also have increased

amplitude, and 3) a cluster with faster aggregation kinetics than WT. The sample size of mutants analysed in this study is limited so an expanded screen of point mutations and their effects on aggregation kinetics will need to be done to explore this further.

A relationship of note was the effect of the mutations and their relative position along the protein sequence (Figure 4.4). The second and third repeat of the microtubules binding domain (R2 and R3) are known to make up the core of tau fibrils produced *in vitro* (Andronesi et al., 2008; L. Li et al., 2002). The mutations that significantly increased tau's aggregation propensity were clustered in the R2/R3 region. Whereas most of the mutations that inhibited aggregation were found in R4 and beyond, the region that makes up the fuzzy coat. The sample is limited in scope covering only a handful of mutants in a region that is known to make up the core of the aggregate so more thorough analysis of mutation type and position in this region may further elucidate this relationship.

4.2 Trypsin Digest Patterns

The next part of this project was to assess the structural elements of the disease-associated mutant tau fibrils with the optimised limited proteolysis and gel electrophoresis protocol described in section 3.5. Tau mutants were expressed and purified on a small scale as before. The proteins were aggregated with heparin monitored by ThT and were treated directly with trypsin and resolved with the ProteinSimple Wes capillary gel electrophoresis system. Due to the protease resistant nature of amyloidogenic aggregates, the remaining fragments resolved on the capillary represent the segments of the protein that comprise the core region and are protected from said protease activity. All 36 mutants, when digested, yielded discrete banding patterns ranging from 4-28 kDa

(Figure 4.5). Recall, the modified trypsin used for the digests is not detected by the ProteinWes total protein detection system.

In order to define similarities between trypsin banding patterns of the mutants, an algorithm-based method modified from the GelJ software was employed to cluster the mutants into bins using the chromatogram data generated by the Wes system. This method described in 2.9.1 unbiasedly sorts the mutants based on how similar their overall banding patterns match, using the Jaccard coefficient. When this was done, a dendrogram was generated that hierarchically clusters the mutants (Figure 4.6). The method was able to categorize the mutant panel into 10 distinct groups of trypsin banding types (Table 4.1). As was seen with the aggregation kinetics, a majority of the mutants aligned with WT and their trypsin banding patterns were not significantly altered. Five mutants generated their own unique structures (K369I, G273R, P301L, R406W, G272V). When the structural subtypes are separated and plotted according to amino acid position, there did not appear to be a significant relationship between the location of mutant along the tau sequences and the structure generated (Figure 4.7A). When the kinetic data from section 4.1 is correlated with the structural subtypes, we see a trend of mutants which had structures similar to wild-type also had kinetics that aligned with WT kinetics although several exceptions to this trend were observed (Figure 4.7B). Mutants that had significantly altered kinetics also tended to exhibit altered structural patterns when compared to WT. For example, P301L/S/T and ΔK280 all are quite fast aggregators and also produce different structures. However, a limited sample size of mutants prevents a more definitive conclusion to be drawn from the presented data. A summary of results

detailing kinetic parameters (lag time, elongation rate constant, amplitude) and structural

subtype by trypsin digestion can be found in table 4.2.

Figure 4.1: **Normalised lag times, elongation rate constants, and amplitudes for disease-associated mutants.** A panel of 36 disease-associated mutants were expressed and small-scale purified. They were aggregated with the inducer heparin and monitored with ThT every five minutes for 24 hours. The resultant curves were analysed as described in section 2.8.1. The lag times (A), elongation rate constant (B), and amplitude (C) were calculated from the nonlinear regression and normalised to WT. Data shown are averages of three replicate reactions ± SD, representative of two independent experiments. Statistical analysis was done using one-way ANOVA with Dunnett's multiple comparisons test to compare each mutant to WT, *P<0.05. Dotted lines represent one standard deviation above and below the mean for WT.

Figure 4.2: **Correlation of kinetic parameters between two replicate experiments.**
The panel of 36 disease-associated mutants were aggregated with heparin and monitored
by ThT in two independent experiments. The curves were analysed by nonlinear
regression described in section 2.8.1 and the lag times, elongation rate constants, and
amplitudes were calculated. The values were averaged from three replicate reactions per
experiment and a correlation graph was generated by plotting the values for lag time (A),
elongation rate constant (B), and amplitude (C) of each mutant against itself between the
two experiments. A linear regression was performed on the correlations and the best-fit
lines are shown with 95% confidence intervals, P values, and R^2. Red dots in C.
correspond to two mutants exhibiting significantly variable amplitude values between
replicates.
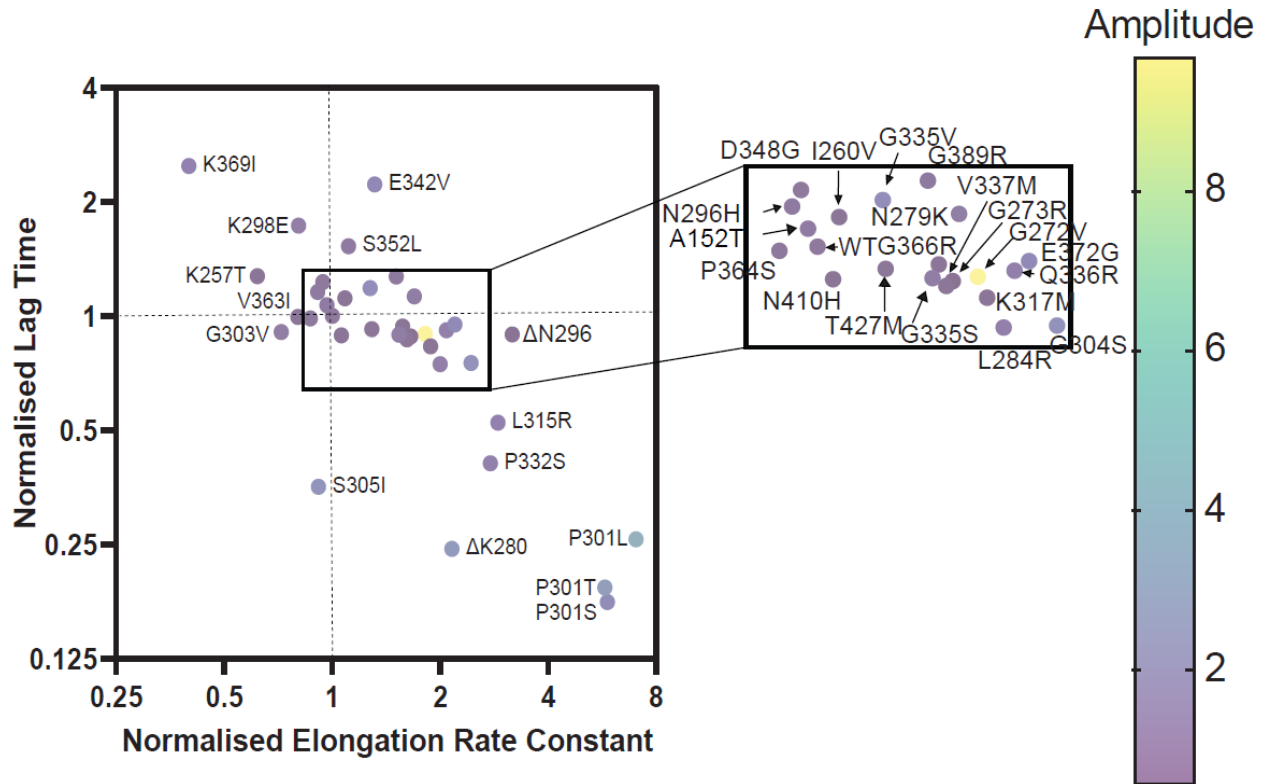
Figure 4.3: **Relationship of lag time, elongation rate constant, and amplitude**. Normalised lag time, elongation rate constant, and amplitude from 36 disease-associated mutants were assessed as described in figure 4.1. Lag times normalised to WT are graphed against elongation rate constant and each point is coloured by normalised amplitude. Data are averages of three replicate reactions from one trial, representative of two independent experiments. Note that the X and Y axes are log scaled with a base of 2.
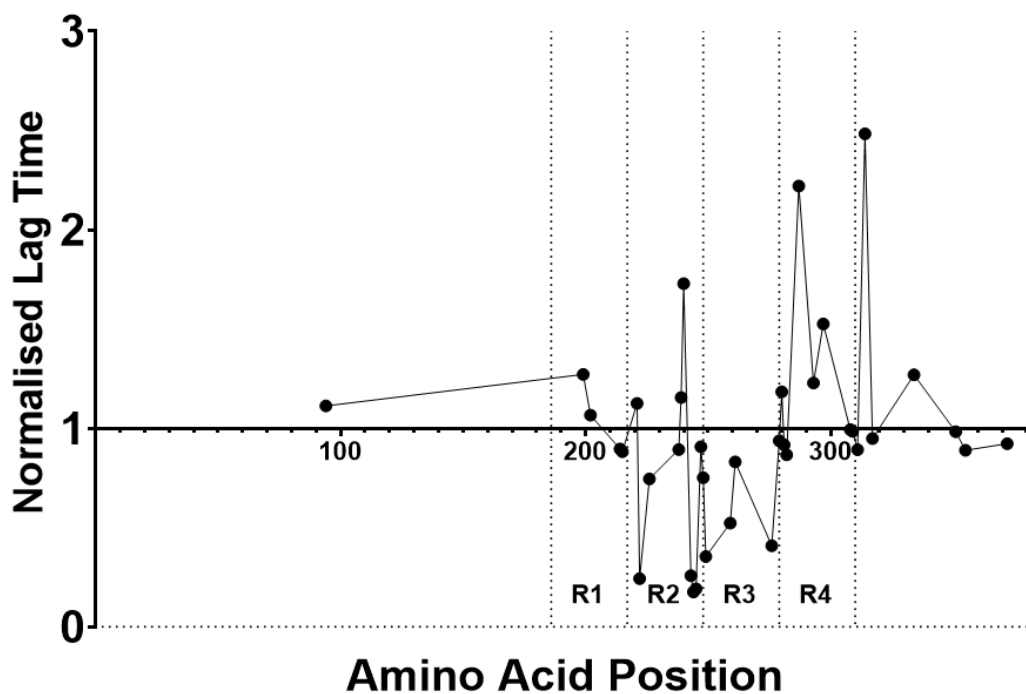
Figure 4.4: **Normalised lag time graphed along amino acid position.** Lag times were calculated from aggregating disease-associated tau mutants with heparin and normalised to WT. Those values are graphed in relation to the position of the mutant along the protein sequence with one tick representing 10 residues. Mutant numberings are in references to 2N4R tau, so their corresponding position will be different on 0N4R (e.g., A125T occurs on residue 94). The microtubule binding region is highlighted with the boundaries of the repeats R1-4 indicated (dashed lines).
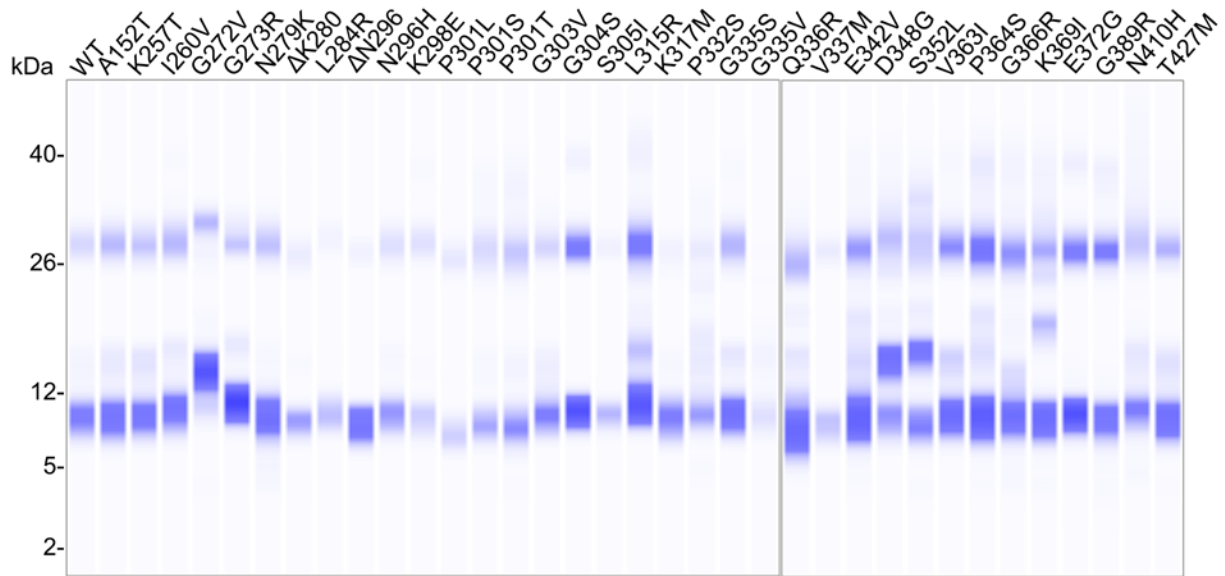
Figure 4.5: **Capillary gel electrophoresis of digested disease-associated tau mutants.** Disease-associated tau mutants were aggregated with heparin and treated with trypsin at a 1:20 enzyme:protein ratio for 3 hours at 37 °C. The protease resistant peptide fragments were resolved by the ProteinSimple capillary gel electrophoresis system and visualized using total protein detection. Data is representative of two independent experiments.
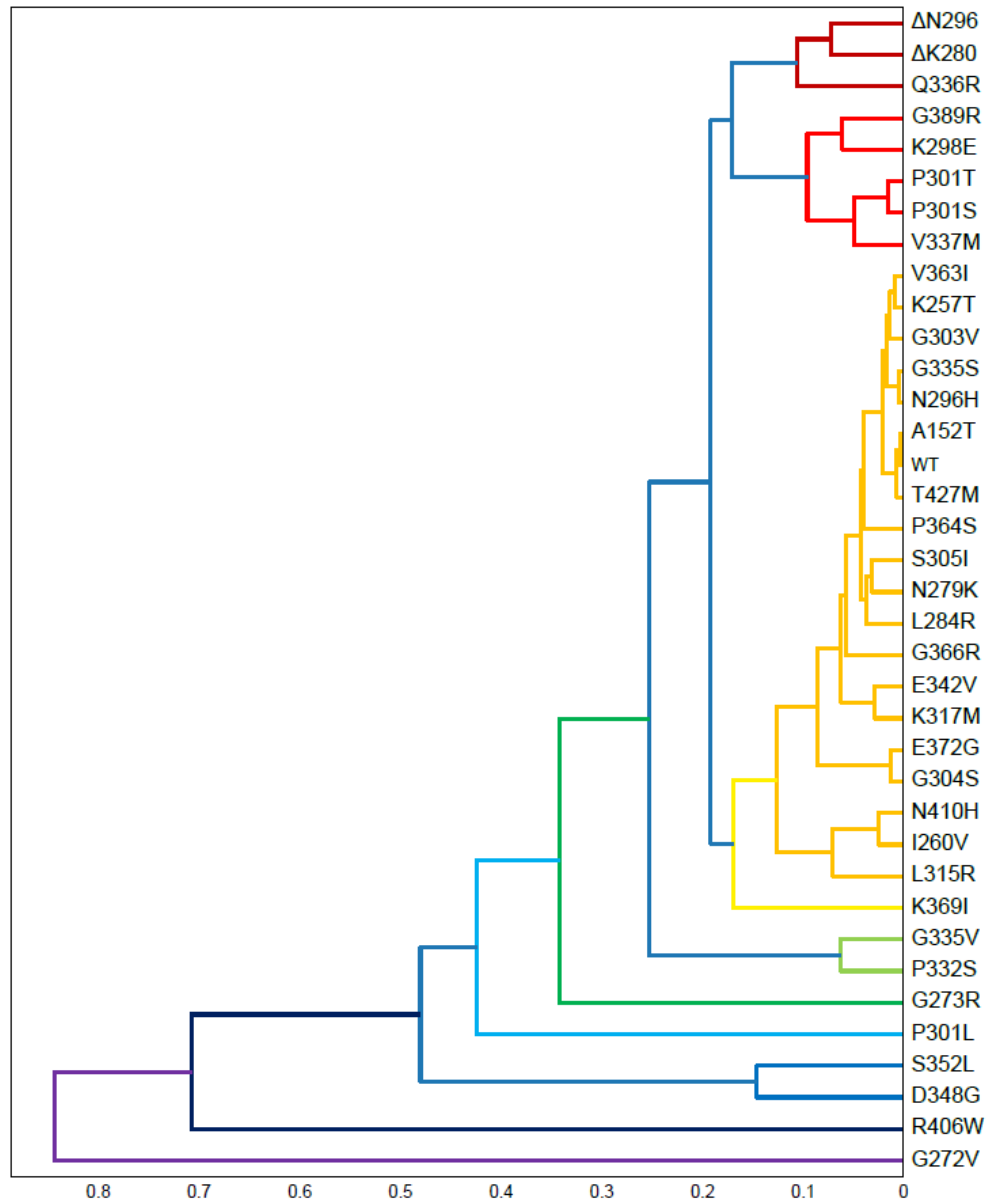
Figure 4.6: **Hierarchical analysis of mutant tau fibril digests by GelJ-based program.**
Mutant digest profiles were compared using a GelJ-based program as described in section 2.9.2. Colours represent groups of similar mutants based on a 0.85 threshold of the Jaccard coefficient.
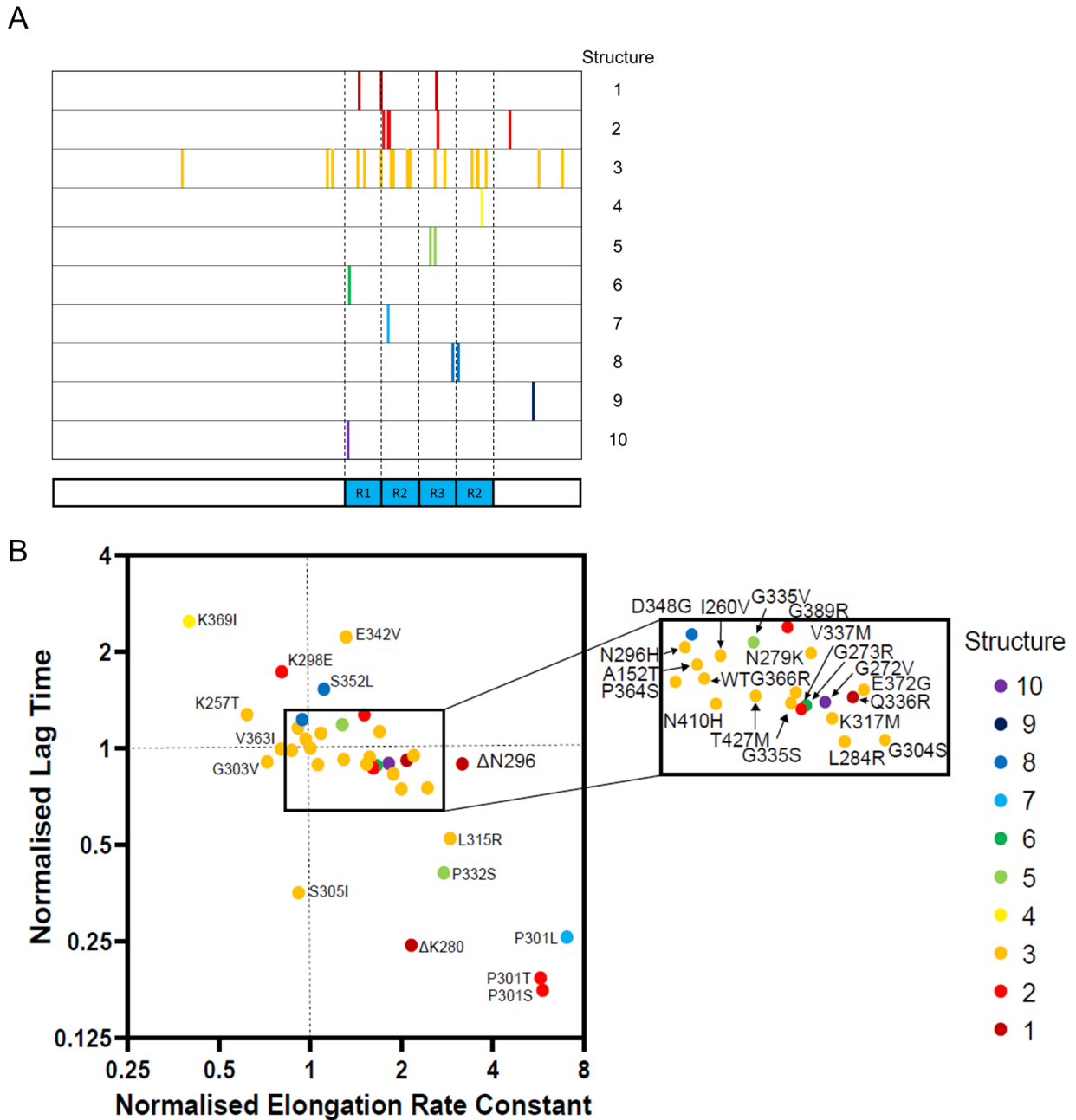
Figure 4.7 **Structural subtypes plotted by sequence alignment and kinetic data**. *A*.
Mutant location charted along the protein sequence (0N4R, shown underneath) grouped
by structure subtype as shown in figure 4.6. *B*. Normalised lag times and elongation rate
constants were assessed as shown in figure 4.3 and points coloured by structure subtype.
Dotted lines indicate a normalised value of 1, equal to WT.

Table 4.1: **Groupings of disease-associated tau mutants by trypsin banding pattern.**

1	2	3	4	5	6	7	8	9	10
ΔN296 ΔK280 Q336R	G389R K298E P301T P301S V337M	WT V363I K257T G303V G335S N296H A152T T427M P364S S305I N279K L284R G366R E342V K317M E372G G304S N410H I260V L315R	K369I	G335V P332S	G273R	P301L	D348G S352L	R406W	G272V

Table 4.2: **Summary of results for kinetic and structural assays**.

	Lag Time	Elongation	Amplitude	Structure
WT	-	-	-	3
A152T	-	-	-	3
K257T	-	-	-	3
I260V	-	-	-	3
G272V	-	-	↑	10
G273R	-	-	-	6
N279K	-	-	-	3
ΔK280	↑	↑	↑	1
L284R	-	-	-	3
ΔN296	-	↑	-	1
N296H	-	-	-	3
K298E	↓	-	-	2
P301L	↑	↑	↑	7
P301S	↑	↑	-	2
P301T	↑	↑	↑	2
G303V	-	-	-	3
G304S	-	↑	↑	3
S305I	↑	-	↑	3
L315R	-	↑	-	3
K317M	-	-	-	3
P332S	↑	↑	-	5
G335S	-	-	-	3
G335V	-	-	↑	5
Q336R	-	↑	-	1
V337M	-	-	-	2
E342V	↓	-	-	3
D348G	-	-	-	8
S352L	↓	-	-	8
V363I	-	-	-	3
P364S	-	-	-	3
G366R	-	-	-	3
K369I	↓	-	-	4
E372G	-	↑	-	3
G389R	↓	-	-	2
N410H	-	-	-	3
T427M	-	-	-	3

Chapter 5

DISCUSSION

5.1 General Results

5.1.1 Influence of Exons 2, 3, and 10 on Aggregation

Kinetic analysis of the six tau isoforms revealed an inhibitory effect of the N-terminal inserts where the propensity to aggregate was 0N>1N>2N (Figure 3.4). This relationship was especially pronounced in the 3R isoforms. One particular explanation for this may be tau's native conformation. While tau is an intrinsically disordered protein, a paper clip-like native conformation has been proposed where the N-terminus folds back and associates with the C-terminus (Jeganathan et al., 2006), Figure 5.1). This interaction may modulate the kinetics of aggregation by obscuring the intermolecular interactions upon induction to aggregate, preventing both nucleation and monomer addition to elongate the fibrils thus reducing the overall aggregation. With the addition of more N-terminal inserts, this alters the charge distribution by introducing more negative charges to the N-terminus and therefore favouring interactions between the more positively charged C-terminus (Figure 1.2). To test for this, the binding potential for the N-terminal inserts to the MTBR and C-terminus region would need to be assessed, which can be done with techniques such as pull-down assays, whereby the N-terminal insert segment of the protein can be expressed and when introduced with the full-length protein, a direct association could be detected with antibodies, or a Fluorescence resonance energy transfer (FRET) assay. The 4R isoforms have an extra microtubule binding repeat and a second aggregation motif which increases its propensity to aggregate in relation to the 3R isoforms. The increased kinetics for the 4R isoforms may be able to overcome most of the inhibitory effects of the N-terminal inserts therefore leading to a reduction in this relationship. Mutations outside of the microtubule binding domain are also capable of

influencing aggregation kinetics and microtubule assembly which may be caused by destabilising the paper-clip conformation of tau (Combs & Gamblin, 2012; Poorkaj et al., 2002). With respect to fibril core packing, the main driving force in determining what folding pathways the reaction would take appeared to be the presence of R2. When aggregated tau isoforms were digested and resolved by SDS-PAGE, the greatest differences in the banding patterns is observed between the 3R and 4R isoforms (Figure 3.6). The effect that the N-terminal inserts played in determining the banding pattern was minimal. A reduction in the total number of bands for the 3R isoform profiles compared to the 4R isoforms suggest these structures are truly different and not simply truncated forms of the same structure. These data suggest that the N-terminal inserts play a role in facilitating the degree to which monomers of tau will interact with each other thus affecting the kinetics. However, the mechanisms by which the fibril core packs is largely unaffected.

5.1.2 Novel Bacterial Inhibitor of Aggregation

One particularly interesting discovery was of a potential inhibitor peptide expressed in bacterial lysate. Other proteins, such as lysozyme or bovine serum albumin, present in the reaction don't affect the rate or degree of aggregation, suggesting the interaction between tau and this bacterial peptide or small molecule is specific. Peptides have been raised to specifically inhibit tau amyloidogenic aggregation using phage display (Malhis et al., 2021). The sequence of one of the peptides raised was DPLKARHTSVWY, which was able to significantly reduce the amount of ThS positive aggregates by shuttling the aggregation reaction towards the production of amorphous aggregates. With a MW of 1472.67, this peptide is within the range of the peptide(s) observed using MALDI-TOF which has a MW of ~1600 Da (Figure 3.9). While the bacterial inhibitor is almost certainly

not the peptide identified in Malhis *et al*, the ability for a peptide natively expressed by cells to inhibit tau aggregation is a promising discovery. A potential role for this peptide could be in therapies targeting protein aggregates in their nascent stages to prevent the production of highly stable amyloidogenic fibrils, allowing for the more amorphous aggregates or small misfolded species to be better handled by the cell's degradation network. For example, the protease trypsin was able to effectively degrade any tau species in our reactions containing the inhibitor (Figure 3.10B). Further work would need to be done to verify the identity of this molecule and whether it is indeed a peptide or simply a small molecule. If it is indeed a peptide, obtaining the sequence and its specificity with which it can inhibit aggregation would need to be verified.

5.2 Disease Associated Tau Mutations

5.2.1 Buffer Conditions Can Significantly Affect Tau Aggregation Kinetics

A major aspect of this project was optimizing a workflow by which I could analyse tau variant kinetics and structures in high-throughput. Many steps were taken to ensure the results generated by this procedural workflow would be reproducible and scalable. The buffer conditions of the assay proved to be a major component of the optimisation. The presence of high amounts of salt in the buffer appeared to have effects on the aggregation of only select tau variants (Figure 3.15, Figure 3.16). The reasons for this are unclear and have not been previously reported. The mutants that were specifically affected did not have any traits in common. One removed a positive charge (ΔK280), one introduced a positive charge (L284R), one was neutral with respect to charge (ΔN296), and one removed a negative charge and replaced it with a hydrophobic amino acid

(E342V). The effect salt had on aggregation was also not consistent. For ΔK280 the presence of increased salt had a pronounced inhibitory effect whereas for the others, higher salt promoted aggregation (Figure 3.16). The inhibition of aggregation at higher concentrations of salt has been demonstrated previously for a truncated construct of tau (Lin et al., 2020). This would suggest that buffer conditions and ionic strength are important factors in the aggregation reaction and could be a source of variability in the field between labs performing assays at differing conditions, specifically when studying tau variants. A comprehensive study on the effects of different salt concentrations and cations found that they indeed play a role in generating alternate core structures (Lövestam et al., 2022). The question of salt concentration with respect to tau aggregation would be especially relevant in the context of a neuron where the local salt concentrations are constantly in flux. A decrease in white matter in the brain with age may disrupt the neuron's saltatory conduction capability thus affecting the local salt concentration along the axon, providing a potential for pathogenicity of tau, and possibly more specifically for tau variants in FTLD-tau (Kohama et al., 2012).

5.2.2 Kinetic Screen of Disease Associated Tau Mutants

With the newly optimised high-throughput workflow, I generated a panel of 36 disease associated mutants which I purified and assessed aggregation properties. This will have been the first study to date to directly compare the aggregate properties of this many tau variants. A majority of the mutants did not significantly differ from WT in the lag time, or the degree of aggregation as measured by the ThT signal (Figure 4.1). The mutants that increased tau's aggregation propensity seemed to be clustered in R2 and R3 while the mutations that decreased its aggregation propensity clustered in R4 (Figure

4.4). The mutants that altered aggregation kinetics using our workflow were corroborated by previous assessments of these mutants (Barghorn et al., 2000; Combs & Gamblin, 2012). Specifically, ΔK280, P301L, and K369I. The core of heparin induced fibrils comprise R2 and R3 (Zhang et al., 2019). Although it's not clear the way in which mutations in this region are able to increase aggregation propensity, they most likely increase tau's ability for self-association by stabilising those interactions. Or for the P301 and P332 mutations specifically, the substitution of a proline for either a leucine, serine, or threonine may increase the ability to generate beta sheets for amyloid formation as proline is inhibitory to beta sheet formation due to the phi angles of its uniquely shaped backbone (S. C. Li et al., 1996). While P364S also removes a proline, it likely did not exhibit the same inducing effect due to it lying outside the region that forms beta sheets in the core of the fibril. Despite some mutations exhibiting an inhibitory effect on aggregation, they remain disease-associated suggesting the inhibitory effect is not sufficient to prevent pathology and eventually disease. Therefore, it's likely some other mechanism may lead to the overcoming of this phenomena. A limitation of this study is the selection bias implicit in the generation of the panel. Because the mutants selected are disease-associated and have a connection to aberrant folding and/or pathology, they are more likely to exhibit deviant aggregate characteristics. Larger sequence connections cannot be made to aggregation behaviour until a more comprehensive screen of tau variants which are systematically replaced (e.g., saturation mutagenesis) is done.

5.2.3 Structural Assessment of Disease Associated Mutants

The core structures of aggregates tau from patient samples have only recently been reported at a high resolution using cryogenic electron microscopy. The diseases

that have been elucidated are Alzheimer's disease, corticobasal degeneration, Pick's disease, chronic traumatic encephalopathy, and argyrophilic grain disease (Shi et al., 2021). The structure of recombinant tau fibrils induced by heparin has also been reported and found to differ from any disease structure (Zhang et al., 2019). Structural effects of disease associated mutations in tau have been elucidated at the fibril level (Combs & Gamblin, 2012) but a more comprehensive assessment of how they specifically affect core packing and conformation has not at present been tackled. One limitation is the sheer number of mutants. Other tauopathies, such as AD, share the relative simplicity of being comprised of WT protein and therefore minimising interpatient heterogeneity. With over 30 mutants implicated in FTLD-tau, using methods such as cryo-EM becomes more challenging to get a high-resolution structure. Also, with these MAPT mutations being relatively rare, obtaining patient samples with these is challenging. Taking advantage of the protease resistant nature of aggregated tau allowed a method by which we were able to get insight into the specific core packing of the mutated proteins in a high throughput and reproducible manner. This method has also been used for patient derived samples and indeed a change in resolved peptides after protease digestion indicated an altered core structure which was then corroborated by cryo-EM studies (Taniguchi-Watanabe et al., 2016).

In this study, I identified 10 unique structural subtypes that the 36 tested mutants fell into with a majority showing the same resistance pattern as WT (Table 4.1). Certain point mutations induce morphological changes to the fibril structure compared to WT so that appears to also confer ultrastructural variance. Based on the kinetic data, it was expected that most structures would not deviate from WT. Mutants that did not have

significantly altered kinetics also did not generally result in an altered banding pattern after trypsin digestion. Two exceptions are S305I and E342V which had significantly altered kinetics (increased and decreased, respectively) but produced aggregates with a WT-like structure. There were also mutants that had aggregation kinetics similar to WT but produced a different structure (G272V, G273R, G335V, V337M, D348G). The comparison of aggregation kinetics to structure suggests these are two separate processes that may have different nucleating events. One event can trigger a mutant to begin aggregating at the same time as WT yet the process that determines what fold is generated may be separate. As with the kinetics, a systematic mutation scan of the tau sequence could elucidate this relationship further and allow us to study these processes more definitively. With the optimised protocol developed and described in this thesis, that should be more than possible to accomplish.
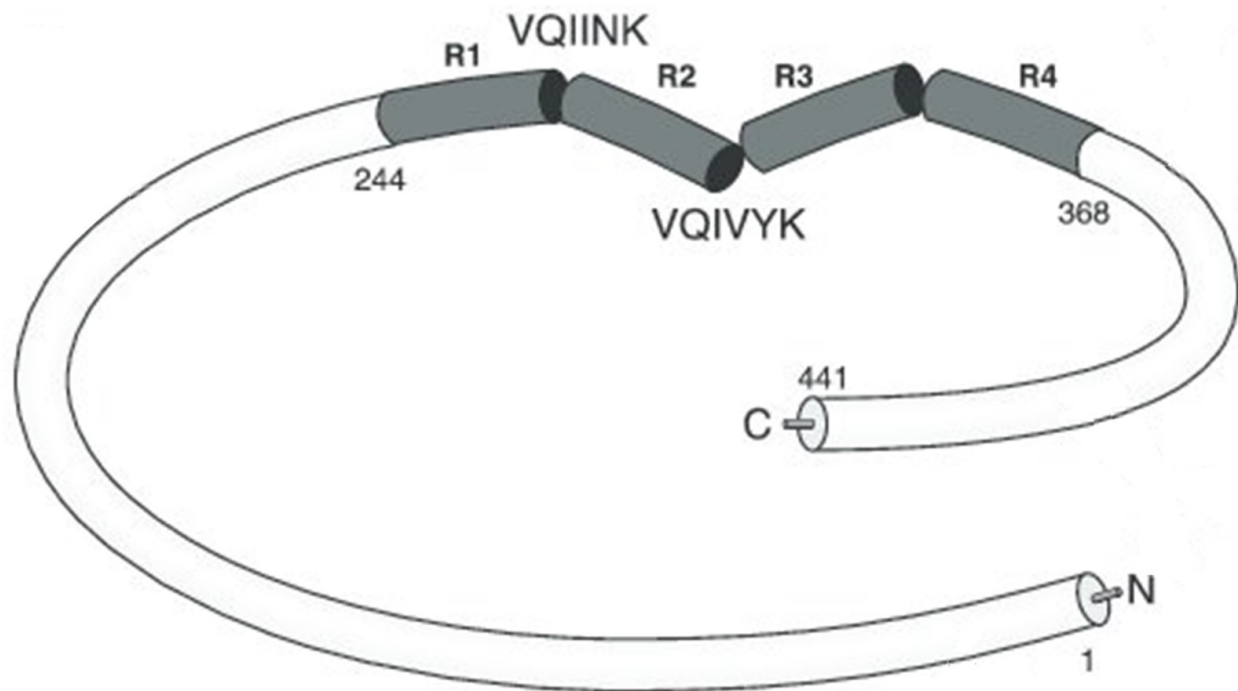
Figure 5.1: **Hairpin conformation of tau.** A proposed conformation of tau in solution involving the amino and carboxy termini folding back, stabilised by electrostatic interactions. This figure was reproduced and adapted with permission from SpringerNature Copyright Clearance Center licence from (De Strooper, 2010).

Chapter 6

CONCLUSIONS AND FUTURE DIRECTIONS

6.1 Conclusions

The primary aim of this work was to establish a high-throughput protocol for generating and studying tau mutants for their aggregation properties. I assayed 36 tau variants associated with FTLD-tau and analysed their aggregation kinetics which revealed a majority of mutants were similar to WT. There were select mutants that increased tau's propensity to aggregate (ΔK280, P301L/S/T, S305I, and P332S) as well as decreased tau's propensity to aggregate (K298E, E342V, S352L, K369I, and G389R). One discovery in this study was the effect of salt concentration on the ability for certain mutants to aggregate (ΔK280, L284R, ΔN296, and E342V). While salt concentration is a common consideration for protein aggregation, this is the first reporting of a specific sensitivity to higher salt for some mutants over others for tau. The structure of these mutants was also assessed through the use of a limited proteolysis assay. On this basis we were able to group the mutants into ten subtypes using a tailored GelJ-based sorting program. When the results of the kinetic analysis and the structural analysis are cross examined, it appears that the mechanism which determines the structure and the mechanism which determines the time and rate of aggregation are separate processes. An additional discovery in this study was a novel bacterial inhibitor of tau aggregation.

6.2 Future Directions

This work provides a scalable method for performing mutant screens of the tau protein (as well as potentially other proteins). A limitation of this study was the small sample size of mutants to make any conclusions based on mutant type or location. Therefore, a worthwhile endeavour would be to perform a saturation mutagenesis scan

of tau whereby each amino acid in a given segment of the protein is systematically substituted with the 19 other possible amino acids. This would generate a library of hundreds of mutants that could easily be purified and assayed for aggregation kinetics and structure. A screen of this scale would provide valuable insight into the sequence-aggregate relationship of tau and may reveal certain areas outside of the MTBR (which makes up the core of the aggregate) which can impact aggregation. Just as well, this screen will likely generate multiple structural variants. Assessing their cytotoxicity could reveal structures that confer a higher or lower degree of toxicity potentially having an implication in disease.

Utilising other techniques to probe the structural elements of these protein aggregates would greatly improve the robustness of our method. One such technique is Fluorescent Amyloid Multiple Emission Spectra (FLAMES) microscopy (Stöhr et al., 2017). This method uses amyloid binding dyes and confocal microscopy to study the structural and conformational elements of these aggregates based on spectral shifts upon binding. Our lab has already begun work on optimising this procedure. Another method that could aid in elucidating conformational differences between mutants is the use of conformation-dependent antibodies and dot blotting. There exist several conformation-dependent antibodies for aggregated tau such as MC1 and Alz50 (Shahani et al., 2006) which would highlight any mutant aggregates that possess a similar fold to the disease derived aggregates that the antibodies were raised against and recognise. These techniques in tandem with the limited proteolysis assay would provide multiple axes to analyse aggregate structure that is also amenable to high-throughput application.

Lastly, we would like to compare the structure of the mutant aggregates to those found in patients. We have access to human patient brain samples of patients with Alzheimer's and FTLD-tau and after extracting the aggregated material from the brain homogenate, we can analyse the structure using our optimised techniques.

REFERENCES

Abreha, M. H., Dammer, E. B., Ping, L., Zhang, T., Duong, D. M., Gearing, M., Lah, J. J., Levey,
    A. I., & Seyfried, N. T. (2018). Quantitative Analysis of the Brain Ubiquitylome in
    Alzheimer's Disease. *PROTEOMICS*, *18*(20), 1800108.
    https://doi.org/10.1002/pmic.201800108

Ahanger, I. A., Parray, Z. A., Nasreen, K., Ahmad, F., Hassan, Md. I., Islam, A., & Sharma, A.
    (2021). Heparin Accelerates the Protein Aggregation via the Downhill Polymerization
    Mechanism: Multi-Spectroscopic Studies to Delineate the Implications on
    Proteinopathies. *ACS Omega*, *6*(3), 2328–2339.
    https://doi.org/10.1021/acsomega.0c05638

Ahmed, Z., Cooper, J., Murray, T. K., Garn, K., McNaughton, E., Clarke, H., Parhizkar, S.,
    Ward, M. A., Cavallini, A., Jackson, S., Bose, S., Clavaguera, F., Tolnay, M., Lavenir, I.,
    Goedert, M., Hutton, M. L., & O'Neill, M. J. (2014). A novel in vivo model of tau
    propagation with rapid and progressive neurofibrillary tangle pathology: The pattern of
    spread is determined by connectivity, not proximity. *Acta Neuropathologica*, *127*(5),
    667–683. https://doi.org/10.1007/s00401-014-1254-6

Alonso, A. del C., Mederlyova, A., Novak, M., Grundke-Iqbal, I., & Iqbal, K. (2004). Promotion of
    hyperphosphorylation by frontotemporal dementia tau mutations. *The Journal of
    Biological Chemistry*, *279*(33), 34873–34881. https://doi.org/10.1074/jbc.M405131200

Alonso, A. del C., Zaidi, T., Novak, M., Barra, H. S., Grundke-Iqbal, I., & Iqbal, K. (2001).
    Interaction of Tau Isoforms with Alzheimer's Disease Abnormally Hyperphosphorylated
    Tau and in VitroPhosphorylation into the Disease-like Protein *. *Journal of Biological
    Chemistry*, *276*(41), 37967–37973. https://doi.org/10.1074/jbc.M105365200

Alonso, A. del C., Zaidi, T., Novak, M., Grundke-Iqbal, I., & Iqbal, K. (2001).
    Hyperphosphorylation induces self-assembly of τ into tangles of paired helical
    filaments/straight filaments. *Proceedings of the National Academy of Sciences*, *98*(12),
    6923–6928. https://doi.org/10.1073/pnas.121119298

Alquezar, C., Arya, S., & Kao, A. W. (2021). Tau Post-translational Modifications: Dynamic

    Transformers of Tau Function, Degradation, and Aggregation. *Frontiers in Neurology*,

    11. https://www.frontiersin.org/article/10.3389/fneur.2020.595532

Alzheimer, A., Stelzmann, R. A., Schnitzlein, H. N., & Murtagh, F. R. (1995). An English

    translation of Alzheimer's 1907 paper, "Uber eine eigenartige Erkankung der Hirnrinde."

    Clinical Anatomy (New York, N.Y.), *8*(6), 429–431. https://doi.org/10.1002/ca.980080612

Andronesi, O. C., von Bergen, M., Biernat, J., Seidel, K., Griesinger, C., Mandelkow, E., &

    Baldus, M. (2008). Characterization of Alzheimer's-like paired helical filaments from the

    core domain of tau protein using solid-state NMR spectroscopy. *Journal of the American*

    Chemical Society, *130*(18), 5922–5928. https://doi.org/10.1021/ja7100517

Arakhamia, T., Lee, C. E., Carlomagno, Y., Kumar, M., Duong, D. M., Wesseling, H., Kundinger,

    S. R., Wang, K., Williams, D., DeTure, M., Dickson, D. W., Cook, C. N., Seyfried, N. T.,

    Petrucelli, L., Steen, J. A., & Fitzpatrick, A. W. P. (2020). Posttranslational Modifications

    Mediate the Structural Diversity of Tauopathy Strains. *Cell*, *180*(4), 633-644.e12.

    https://doi.org/10.1016/j.cell.2020.01.027

Arosio, P., Knowles, T. P. J., & Linse, S. (2015). On the lag phase in amyloid fibril formation.

    Physical Chemistry Chemical Physics, *17*(12), 7606–7618.

    https://doi.org/10.1039/C4CP05563B

Barghorn, S., Zheng-Fischhöfer, Q., Ackmann, M., Biernat, J., von Bergen, M., Mandelkow, E.-

    M., & Mandelkow, E. (2000). Structure, Microtubule Interactions, and Paired Helical

    Filament Aggregation by Tau Mutants of Frontotemporal Dementias. *Biochemistry*,

    39(38), 11714–11721. https://doi.org/10.1021/bi000850r

Barracchia, C. G., Tira, R., Parolini, F., Munari, F., Bubacco, L., Spyroulias, G. A., D'Onofrio, M.,

    & Assfalg, M. (2020). Unsaturated Fatty Acid-Induced Conformational Transitions and

    Aggregation of the Repeat Domain of Tau. *Molecules*, *25*(11), 2716.

    https://doi.org/10.3390/molecules25112716

Bessen, R. A., & Marsh, R. F. (1992). Biochemical and physical properties of the prion protein

from two strains of the transmissible mink encephalopathy agent. *Journal of Virology*,

66(4), 2096–2101. https://doi.org/10.1128/JVI.66.4.2096-2101.1992

Biancalana, M., & Koide, S. (2010). Molecular mechanism of Thioflavin-T binding to amyloid

fibrils. *Biochimica et Biophysica Acta (BBA) - Proteins and Proteomics*, *1804*(7), 1405–

1412. https://doi.org/10.1016/j.bbapap.2010.04.001

Biernat, J., Gustke, N., Drewes, G., Mandelkow, E.-., & Mandelkow, E. (1993). Phosphorylation

of Ser262 strongly reduces binding of tau to microtubules: Distinction between PHF-like

immunoreactivity and microtubule binding. *Neuron*, *11*(1), 153–163.

https://doi.org/10.1016/0896-6273(93)90279-Z

Biernat, J., & Mandelkow, E.-M. (1999). The Development of Cell Processes Induced by tau

Protein Requires Phosphorylation of Serine 262 and 356 in the Repeat Domain and Is

Inhibited by Phosphorylation in the Proline-rich Domains. *Molecular Biology of the Cell*,

10(3), 727–740. https://doi.org/10.1091/mbc.10.3.727

Binder, L. I., Frankfurter, A., & Rebhun, L. I. (1985). The distribution of tau in the mammalian

central nervous system. *The Journal of Cell Biology*, *101*(4), 1371–1378.

https://doi.org/10.1083/jcb.101.4.1371

Black, M. M., Slaughter, T., Moshiach, S., Obrocka, M., & Fischer, I. (1996). Tau Is Enriched on

Dynamic Microtubules in the Distal Region of Growing Axons. *Journal of Neuroscience*,

16(11), 3601–3619. https://doi.org/10.1523/JNEUROSCI.16-11-03601.1996

Bondareff, W., Harrington, C., Wischik, C. M., Hauser, D. L., & Roth, M. (1994).

Immunohistochemical staging of neurofibrillary degeneration in Alzheimer's disease.

Journal of Neuropathology and Experimental Neurology, *53*(2), 158–164.

https://doi.org/10.1097/00005072-199403000-00007

Bousset, L., Pieri, L., Ruiz-Arlandis, G., Gath, J., Jensen, P. H., Habenstein, B., Madiona, K.,

Olieric, V., Böckmann, A., Meier, B. H., & Melki, R. (2013). Structural and functional

characterization of two alpha-synuclein strains. *Nature Communications*, *4*, 2575. https://doi.org/10.1038/ncomms3575

Braak, H., Alafuzoff, I., Arzberger, T., Kretzschmar, H., & Del Tredici, K. (2006). Staging of Alzheimer disease-associated neurofibrillary pathology using paraffin sections and immunocytochemistry. *Acta Neuropathologica*, *112*(4), 389–404. https://doi.org/10.1007/s00401-006-0127-z

Braak, H., & Braak, E. (1991). Neuropathological stageing of Alzheimer-related changes. *Acta Neuropathologica*, *82*(4), 239–259. https://doi.org/10.1007/BF00308809

Brion, J.-P., Passareiro, H., Nunez, J., & Flament-Durand, J. (1985). Mise en évidence immunologique de la protéine tau au niveau des lésions de dégénérescence neurofibrillaire de la maladie d'Alzheimer. Arch Biol. *Arch.Biol.(Brux)*, *95*, 229–235.

Chen, D., Drombosky, K. W., Hou, Z., Sari, L., Kashmer, O. M., Ryder, B. D., Perez, V. A., Woodard, D. R., Lin, M. M., Diamond, M. I., & Joachimiak, L. A. (2019). Tau local structure shields an amyloid-forming motif and controls aggregation propensity. *Nature Communications*, *10*(1), 2493. https://doi.org/10.1038/s41467-019-10355-1

Combs, B., & Gamblin, T. C. (2012). FTDP-17 tau mutations induce distinct effects on aggregation and microtubule interactions. *Biochemistry*, *51*(43), 8597–8607. https://doi.org/10.1021/bi3010818

Coppola, G., Chinnathambi, S., Lee, J. J., Dombroski, B. A., Baker, M. C., Soto-Ortolaza, A. I., Lee, S. E., Klein, E., Huang, A. Y., Sears, R., Lane, J. R., Karydas, A. M., Kenet, R. O., Biernat, J., Wang, L.-S., Cotman, C. W., Decarli, C. S., Levey, A. I., Ringman, J. M., … Geschwind, D. H. (2012). Evidence for a role of the rare p.A152T variant in MAPT in increasing the risk for FTD-spectrum and Alzheimer's diseases. *Human Molecular Genetics*, *21*(15), 3500–3512. https://doi.org/10.1093/hmg/dds161

Cripps, D., Thomas, S. N., Jeng, Y., Yang, F., Davies, P., & Yang, A. J. (2006). Alzheimer Disease-specific Conformation of Hyperphosphorylated Paired Helical Filament-Tau Is

Polyubiquitinated through Lys-48, Lys-11, and Lys-6 Ubiquitin Conjugation *. *Journal of Biological Chemistry*, *281*(16), 10825–10838. https://doi.org/10.1074/jbc.M512786200

Crowther, R. A. (1991). Straight and paired helical filaments in Alzheimer disease have a common structural unit. *Proceedings of the National Academy of Sciences of the United States of America*, *88*(6), 2288–2292.

De Strooper, B. (2010). Proteases and Proteolysis in Alzheimer Disease: A Multifactorial View on the Disease Process. *Physiological Reviews*, *90*(2), 465–494. https://doi.org/10.1152/physrev.00023.2009

Debnath, M., Dey, S., Sreenivas, N., Pal, P. K., & Yadav, R. (2022). Genetic and Epigenetic Constructs of Progressive Supranuclear Palsy. *Annals of Neurosciences*, 09727531221089396. https://doi.org/10.1177/09727531221089396

Devenney, E. M., Ahmed, R. M., Hodges, J. R. (2019). Frontotemporal dementia. In Handbook of Clinical Neurology (pp. 279–299). Elsevier. http://dx.doi.org/10.1016/b978-0-12-804766-8.00015-7

Diner, I., Nguyen, T., & Seyfried, N. T. (2017). Enrichment of Detergent-insoluble Protein Aggregates from Human Postmortem Brain. *Journal of Visualized Experiments : JoVE*, *128*, 55835. https://doi.org/10.3791/55835

Dolado, I., Nieto, J., Saraiva, M. J. M., Arsequell, G., Valencia, G., & Planas, A. (2005). Kinetic Assay for High-Throughput Screening of In Vitro Transthyretin Amyloid Fibrillogenesis Inhibitors. *Journal of Combinatorial Chemistry*, *7*(2), 246–252. https://doi.org/10.1021/cc049849s

D'Souza, I., Poorkaj, P., Hong, M., Nochlin, D., Lee, V. M., Bird, T. D., & Schellenberg, G. D. (1999). Missense and silent tau gene mutations cause frontotemporal dementia with parkinsonism-chromosome 17 type, by affecting multiple alternative RNA splicing regulatory elements. *Proceedings of the National Academy of Sciences of the United States of America*, *96*(10), 5598–5603. https://doi.org/10.1073/pnas.96.10.5598

Falcon, B., Zhang, W., Schweighauser, M., Murzin, A. G., Vidal, R., Garringer, H. J., Ghetti, B., Scheres, S. H. W., & Goedert, M. (2018). Tau filaments from multiple cases of sporadic and inherited Alzheimer's disease adopt a common fold. *Acta Neuropathologica*, *136*(5), 699–708. https://doi.org/10.1007/s00401-018-1914-z

Ferrer, I., Barrachina, M., & Puig, B. (2002). Glycogen synthase kinase-3 is associated with neuronal and glial hyperphosphorylated tau deposits in Alzheimer's disease, Pick's disease, progressive supranuclear palsy and corticobasal degeneration. *Acta Neuropathologica*, *104*(6), 583–591. https://doi.org/10.1007/s00401-002-0587-8

Fichou, Y., Lin, Y., Rauch, J. N., Vigers, M., Zeng, Z., Srivastava, M., Keller, T. J., Freed, J. H., Kosik, K. S., & Han, S. (2018). Cofactors are essential constituents of stable and seeding-active tau fibrils. *Proceedings of the National Academy of Sciences*, *115*(52), 13234–13239. https://doi.org/10.1073/pnas.1810058115

Fichou, Y., Oberholtzer, Z. R., Ngo, H., Cheng, C.-Y., Keller, T. J., Eschmann, N. A., & Han, S. (2019). Tau-Cofactor Complexes as Building Blocks of Tau Fibrils. *Frontiers in Neuroscience*, *13*. https://www.frontiersin.org/article/10.3389/fnins.2019.01339

Fichou, Y., Vigers, M., Goring, A. K., Eschmann, N. A., & Han, S. (2018). Heparin-induced tau filaments are structurally heterogeneous and differ from Alzheimer's disease filaments. *Chemical Communications*, *54*(36), 4573–4576. https://doi.org/10.1039/C8CC01355A

Fitzpatrick, A. W. P., Falcon, B., He, S., Murzin, A. G., Murshudov, G., Garringer, H. J., Crowther, R. A., Ghetti, B., Goedert, M., & Scheres, S. H. W. (2017). Cryo-EM structures of tau filaments from Alzheimer's disease. *Nature*, *547*(7662), 185–190. https://doi.org/10.1038/nature23002

Flach, K., Hilbrich, I., Schiffmann, A., Gärtner, U., Krüger, M., Leonhardt, M., Waschipky, H., Wick, L., Arendt, T., & Holzer, M. (2012). Tau Oligomers Impair Artificial Membrane Integrity and Cellular Viability. *The Journal of Biological Chemistry*, *287*(52), 43223–43233. https://doi.org/10.1074/jbc.M112.396176

Frank, J., Radermacher, M., Penczek, P., Zhu, J., Li, Y., Ladjadj, M., & Leith, A. (1996).

    SPIDER and WEB: Processing and Visualization of Images in 3D Electron Microscopy

    and Related Fields. *Journal of Structural Biology*, *116*(1), 190–199.

    https://doi.org/10.1006/jsbi.1996.0030

Franzmeier, N., Dewenter, A., Frontzkowski, L., Dichgans, M., Rubinski, A., Neitzel, J., Smith,

    R., Strandberg, O., Ossenkoppele, R., Buerger, K., Duering, M., Hansson, O., & Ewers,

    M. (2020). Patient-centered connectivity-based prediction of tau pathology spread in

    Alzheimer's disease. *Science Advances*, *6*(48). https://doi.org/10.1126/sciadv.abd1327

Gade Malmos, K., Blancas-Mejia, L. M., Weber, B., Buchner, J., Ramirez-Alvarado, M., Naiki,

    H., & Otzen, D. (2017). ThT 101: A primer on the use of thioflavin T to investigate

    amyloid formation. *Amyloid: The International Journal of Experimental and Clinical*

    Investigation: The Official Journal of the International Society of Amyloidosis, *24*(1), 1–

    16. https://doi.org/10.1080/13506129.2017.1304905

Gambetti, P., Kong, Q., Zou, W., Parchi, P., & Chen, S. G. (2003). Sporadic and familial CJD:

    Classification and characterisation. *British Medical Bulletin*, *66*, 213–239.

    https://doi.org/10.1093/bmb/66.1.213

Gavett, B. E., Stern, R. A., & McKee, A. C. (2011). Chronic Traumatic Encephalopathy: A

    Potential Late Effect of Sport-Related Concussive and Subconcussive Head Trauma.

    Clinics in Sports Medicine, *30*(1), 179–188. https://doi.org/10.1016/j.csm.2010.09.007

Ghetti, B., Oblak, A. L., Boeve, B. F., Johnson, K. A., Dickerson, B. C., & Goedert, M. (2015).

    Invited review: Frontotemporal dementia caused by microtubule-associated protein tau

    gene (MAPT) mutations: a chameleon for neuropathology and neuroimaging.

    Neuropathology and Applied Neurobiology, *41*(1), 24–46.

    https://doi.org/10.1111/nan.12213

Goedert, M., Jakes, R., & Crowther, R. A. (1999). Effects of frontotemporal dementia FTDP-17

    mutations on heparin-induced assembly of tau filaments. *FEBS Letters*, *450*(3), 306–

311. https://doi.org/10.1016/s0014-5793(99)00508-6

Goedert, M., Jakes, R., Spillantini, M. G., Hasegawa, M., Smith, M. J., & Crowther, R. A. (1996).

    Assembly of microtubule-associated protein tau into Alzheimer-like filaments induced by

    sulphated glycosaminoglycans. *Nature*, *383*(6600), 550–553.

    https://doi.org/10.1038/383550a0

Goedert, M., Spillantini, M. G., Potier, M. C., Ulrich, J., & Crowther, R. A. (1989). Cloning and

    sequencing of the cDNA encoding an isoform of microtubule-associated protein tau

    containing four tandem repeats: Differential expression of tau protein mRNAs in human

    brain. *The EMBO Journal*, *8*(2), 393–399.

Goldbaum, O., Oppermann, M., Handschuh, M., Dabir, D., Zhang, B., Forman, M. S.,

    Trojanowski, J. Q., Lee, V. M.-Y., & Richter-Landsberg, C. (2003). Proteasome Inhibition

    Stabilizes Tau Inclusions in Oligodendroglial Cells that Occur after Treatment with

    Okadaic Acid. *The Journal of Neuroscience*, *23*(26), 8872–8880.

    https://doi.org/10.1523/JNEUROSCI.23-26-08872.2003

Goode, B. L., Chau, M., Denis, P. E., & Feinstein, S. C. (2000). Structural and Functional

    Differences between 3-Repeat and 4-Repeat Tau Isoforms: IMPLICATIONS FOR

    NORMAL TAU FUNCTION AND THE ONSET OF NEURODEGENERATIVE DISEASE*.

    Journal of Biological Chemistry, *275*(49), 38182–38189.

    https://doi.org/10.1074/jbc.M007489200

Goode, B. L., Denis, P. E., Panda, D., Radeke, M. J., Miller, H. P., Wilson, L., & Feinstein, S. C.

    (1997). Functional interactions between the proline-rich and repeat regions of tau

    enhance microtubule binding and assembly. *Molecular Biology of the Cell*, *8*(2), 353–

    365. https://doi.org/10.1091/mbc.8.2.353

Greaves, C. V., & Rohrer, J. D. (2019). An update on genetic frontotemporal dementia. *Journal*

    of Neurology, *266*(8), 2075–2086. https://doi.org/10.1007/s00415-019-09363-4

Greenberg, S. G., Davies, P., Schein, J. D., & Binder, L. I. (1992). Hydrofluoric acid-treated tau

PHF proteins display the same biochemical properties as normal tau. *Journal of Biological Chemistry*, *267*(1), 564–569. https://doi.org/10.1016/S0021-9258(18)48531-6

Grover, A., DeTure, M., Yen, S. H., & Hutton, M. (2002). Effects on splicing and protein function of three mutations in codon N296 of tau in vitro. *Neuroscience Letters*, *323*(1), 33–36. https://doi.org/10.1016/s0304-3940(02)00124-6

Guerrero-Ferreira, R., Taylor, N. M., Mona, D., Ringler, P., Lauer, M. E., Riek, R., Britschgi, M., & Stahlberg, H. (2018). Cryo-EM structure of alpha-synuclein fibrils. *ELife*, *7*, e36402. https://doi.org/10.7554/eLife.36402

Gustke, N., Trinczek, B., Biernat, J., Mandelkow, E.-M., & Mandelkow, E. (1994). Domains of tau Protein and Interactions with Microtubules. *Biochemistry*, *33*(32), 9511–9522. https://doi.org/10.1021/bi00198a017

Harris, J. R. (2015). Transmission electron microscopy in molecular structural biology: A historical survey. *Archives of Biochemistry and Biophysics*, *581*, 3–18. https://doi.org/10.1016/j.abb.2014.11.011

Hartl, F. U. (2017). Protein Misfolding Diseases. *Annual Review of Biochemistry*, *86*, 21–26. https://doi.org/10.1146/annurev-biochem-061516-044518

Heras, J., Domínguez, C., Mata, E., Pascual, V., Lozano, C., Torres, C., & Zarazaga, M. (2015). GelJ – a tool for analyzing DNA fingerprint gel images. *BMC Bioinformatics*, *16*(1), 270. https://doi.org/10.1186/s12859-015-0703-0

Hernández, F., Pérez, M., Lucas, J. J., & Avila, J. (2002). Sulfo-glycosaminoglycan content affects PHF-tau solubility and allows the identification of different types of PHFs. *Brain Research*, *935*(1–2), 65–72. https://doi.org/10.1016/s0006-8993(02)02455-1

Hippius, H., & Neundörfer, G. (2003). The discovery of Alzheimer's disease. *Dialogues in Clinical Neuroscience*, *5*(1), 101–108.

Holehouse, A. S., Das, R. K., Ahad, J. N., Richardson, M. O. G., & Pappu, R. V. (2017). CIDER: Resources to Analyze Sequence-Ensemble Relationships of Intrinsically Disordered

Proteins. *Biophysical Journal*, *112*(1), 16–21. https://doi.org/10.1016/j.bpj.2016.11.3200

Jeganathan, S., von Bergen, M., Brutlach, H., Steinhoff, H.-J., & Mandelkow, E. (2006). Global

Hairpin Folding of Tau in Solution. *Biochemistry*, *45*(7), 2283–2293.

https://doi.org/10.1021/bi0521543

Kascsak, R. J., Rubenstein, R., Merz, P. A., Carp, R. I., Wisniewski, H. M., & Diringer, H.

(1985). Biochemical differences among scrapie-associated fibrils support the biological

diversity of scrapie agents. *The Journal of General Virology*, *66 (Pt 8)*, 1715–1722.

https://doi.org/10.1099/0022-1317-66-8-1715

Kohama, S. G., Rosene, D. L., & Sherman, L. S. (2012). Age-related changes in human and

non-human primate white matter: From myelination disturbances to cognitive decline.

AGE, *34*(5), 1093–1110. https://doi.org/10.1007/s11357-011-9357-7

KrishnaKumar, V. G., & Gupta, S. (2017). Simplified method to obtain enhanced expression of

tau protein from E. coli and one-step purification by direct boiling. *Preparative*

Biochemistry & Biotechnology, *47*(5), 530–538.

https://doi.org/10.1080/10826068.2016.1275012

Kumar, S., Tepper, K., Kaniyappan, S., Biernat, J., Wegmann, S., Mandelkow, E.-M., Müller, D.

J., & Mandelkow, E. (2014). Stages and Conformations of the Tau Repeat Domain

during Aggregation and Its Effect on Neuronal Toxicity *. *Journal of Biological Chemistry*,

289(29), 20318–20332. https://doi.org/10.1074/jbc.M114.554725

Lasagna-Reeves, C. A., Castillo-Carranza, D. L., Guerrero-Muoz, M. J., Jackson, G. R., &

Kayed, R. (2010). Preparation and characterization of neurotoxic tau oligomers.

Biochemistry, 49(47), 10039–10041. https://doi.org/10.1021/bi1016233

Lasagna-Reeves, C. A., Castillo-Carranza, D. L., Sengupta, U., Clos, A. L., Jackson, G. R., &

Kayed, R. (2011). Tau oligomers impair memory and induce synaptic and mitochondrial

dysfunction in wild-type mice. *Molecular Neurodegeneration*, *6*(1), 39.

https://doi.org/10.1186/1750-1326-6-39

Lee, M. S., & Kong, J. (2015). Heparin: Physiology, Pharmacology, and Clinical Application. *Reviews in Cardiovascular Medicine*, *16*(3), 189–199. https://doi.org/10.3909/ricm0778

Lee, S., Choi, M. C., Al Adem, K., Lukman, S., & Kim, T.-Y. (2020). Aggregation and Cellular Toxicity of Pathogenic or Non-pathogenic Proteins. *Scientific Reports*, *10*(1), 5120. https://doi.org/10.1038/s41598-020-62062-3

Li, L., Jiang, Y., Wang, J.-Z., Liu, R., & Wang, X. (2022). Tau Ubiquitination in Alzheimer's Disease. *Frontiers in Neurology*, *12*. https://www.frontiersin.org/article/10.3389/fneur.2021.786353

Li, L., von Bergen, M., Mandelkow, E.-M., & Mandelkow, E. (2002). Structure, stability, and aggregation of paired helical filaments from tau protein and FTDP-17 mutants probed by tryptophan scanning mutagenesis. *The Journal of Biological Chemistry*, *277*(44), 41390–41400. https://doi.org/10.1074/jbc.M206334200

Li, S. C., Goto, N. K., Williams, K. A., & Deber, C. M. (1996). Alpha-helical, but not beta-sheet, propensity of proline is determined by peptide environment. *Proceedings of the National Academy of Sciences*, *93*(13), 6676–6681. https://doi.org/10.1073/pnas.93.13.6676

Lin, Y., Fichou, Y., Zeng, Z., Hu, N. Y., & Han, S. (2020). Electrostatically Driven Complex Coacervation and Amyloid Aggregation of Tau Are Independent Processes with Overlapping Conditions. *ACS Chemical Neuroscience*, *11*(4), 615–627. https://doi.org/10.1021/acschemneuro.9b00627

Lindwall, G., & Cole, R. D. (1984). Phosphorylation affects the ability of tau protein to promote microtubule assembly. *Journal of Biological Chemistry*, *259*(8), 5301–5305. https://doi.org/10.1016/S0021-9258(17)42989-9

Lövestam, S., Koh, F. A., van Knippenberg, B., Kotecha, A., Murzin, A. G., Goedert, M., & Scheres, S. H. (2022). Assembly of recombinant tau into filaments identical to those of Alzheimer's disease and chronic traumatic encephalopathy. *ELife*, *11*, e76494. https://doi.org/10.7554/eLife.76494

Lu, J.-X., Qiang, W., Yau, W.-M., Schwieters, C. D., Meredith, S. C., & Tycko, R. (2013). Molecular structure of β-amyloid fibrils in Alzheimer's disease brain tissue. *Cell*, *154*(6), 1257–1268. https://doi.org/10.1016/j.cell.2013.08.035

Ludtke, S. J., Baldwin, P. R., & Chiu, W. (1999). EMAN: Semiautomated Software for High-Resolution Single-Particle Reconstructions. *Journal of Structural Biology*, *128*(1), 82–97. https://doi.org/10.1006/jsbi.1999.4174

Mackenzie, I. R. A., & Neumann, M. (2016). Molecular neuropathology of frontotemporal dementia: Insights into disease mechanisms from postmortem studies. *Journal of Neurochemistry*, *138*(S1), 54–70. https://doi.org/10.1111/jnc.13588

Maeda, S., Sahara, N., Saito, Y., Murayama, M., Yoshiike, Y., Kim, H., Miyasaka, T., Murayama, S., Ikai, A., & Takashima, A. (2007). Granular Tau Oligomers as Intermediates of Tau Filaments. *Biochemistry*, *46*(12), 3856–3861. https://doi.org/10.1021/bi061359o

Maeda, S., Sato, Y., & Takashima, A. (2018). Frontotemporal dementia with Parkinsonism linked to chromosome-17 mutations enhance tau oligomer formation. *Neurobiology of Aging*, *69*, 26–32. https://doi.org/10.1016/j.neurobiolaging.2018.04.014

Magnus Kjaergaard, Alexander J. Dear, Franziska Kundel, Seema Qamar, Georg Meisl, Tuomas P. J. Knowles, & David Klenerman. (2018). Oligomer Diversity during the Aggregation of the Repeat Region of Tau | ACS Chemical Neuroscience. *ACS Chemical Neuroscience*, *9*(12), 3060–3071. https://doi.org/DOI: 10.1021/acschemneuro.8b00250

Malhis, M., Kaniyappan, S., Aillaud, I., Chandupatla, R. R., Ramirez, L. M., Zweckstetter, M., Horn, A. H. C., Mandelkow, E., Sticht, H., & Funke, S. A. (2021). Potent Tau Aggregation Inhibitor D-Peptides Selected against Tau-Repeat 2 Using Mirror Image Phage Display. *Chembiochem: A European Journal of Chemical Biology*, *22*(21), 3049–3059. https://doi.org/10.1002/cbic.202100287

Maxwell, A. M., Yuan, P., Rivera, B. M., Schaaf, W., Mladinov, M., Prasher, V. P., Robinson, A.

C., DeGrado, W. F., & Condello, C. (2021). Emergence of distinct and heterogeneous strains of amyloid beta with advanced Alzheimer's disease pathology in Down syndrome. *Acta Neuropathologica Communications*, *9*(1), 201. https://doi.org/10.1186/s40478-021-01298-0

McKee, A. C., Cantu, R. C., Nowinski, C. J., Hedley-Whyte, E. T., Gavett, B. E., Budson, A. E., Santini, V. E., Lee, H.-S., Kubilus, C. A., & Stern, R. A. (2009). Chronic Traumatic Encephalopathy in Athletes: Progressive Tauopathy After Repetitive Head Injury. *Journal of Neuropathology & Experimental Neurology*, *68*(7), 709–735. https://doi.org/10.1097/NEN.0b013e3181a9d503

Morales, R., Abid, K., & Soto, C. (2007). The prion strain phenomenon: Molecular basis and unprecedented features. *Biochimica et Biophysica Acta*, *1772*(6), 681–691. https://doi.org/10.1016/j.bbadis.2006.12.006

Moreno, F. J., Medina, M., Pérez, M., Montejo de Garcini, E., & Avila, J. (1995). Glycogen synthase kinase 3 phosphorylates recombinant human tau protein at serine-262 in the presence of heparin (or tubulin). *FEBS Letters*, *372*(1), 65–68. https://doi.org/10.1016/0014-5793(95)00934-2

Mukrasch, M. D., von Bergen, M., Biernat, J., Fischer, D., Griesinger, C., Mandelkow, E., & Zweckstetter, M. (2007). The "Jaws" of the Tau-Microtubule Interaction*. *Journal of Biological Chemistry*, *282*(16), 12230–12239. https://doi.org/10.1074/jbc.M607159200

Nader, H. B., Chavante, S. F., dos-Santos, E. A., Oliveira, F. W., de-Paiva, J. F., Jerônimo, S. M. B., Medeiros, G. F., de-Abreu, L. R. D., Leite, E. L., de-Sousa-Filho, J. F., Castro, R. a. B., Toma, L., Tersariol, I. L. S., Porcionatto, M. A., & Dietrich, C. P. (1999). Heparan sulfates and heparins: Similar compounds performing the same functions in vertebrates and invertebrates? *Brazilian Journal of Medical and Biological Research*, *32*, 529–538. https://doi.org/10.1590/S0100-879X1999000500005

Nam, W.-H., & Choi, Y. P. (2018). In vitro generation of tau aggregates conformationally distinct

from parent tau seeds of Alzheimer's brain. *Prion*, *13*(1), 1–12. https://doi.org/10.1080/19336896.2018.1545524

Necula, M., & Kuret, J. (2004). Pseudophosphorylation and Glycation of Tau Protein Enhance but Do Not Trigger Fibrillization in Vitro*. *Journal of Biological Chemistry*, *279*(48), 49694–49703. https://doi.org/10.1074/jbc.M405527200

Neddens, J., Temmel, M., Flunkert, S., Kerschbaumer, B., Hoeller, C., Loeffler, T., Niederkofler, V., Daum, G., Attems, J., & Hutter-Paier, B. (2018). Phosphorylation of different tau sites during progression of Alzheimer's disease. *Acta Neuropathologica Communications*, *6*(1), 52. https://doi.org/10.1186/s40478-018-0557-6

Nelson, P. T., Alafuzoff, I., Bigio, E. H., Bouras, C., Braak, H., Cairns, N. J., Castellani, R. J., Crain, B. J., Davies, P., Tredici, K. D., Duyckaerts, C., Frosch, M. P., Haroutunian, V., Hof, P. R., Hulette, C. M., Hyman, B. T., Iwatsubo, T., Jellinger, K. A., Jicha, G. A., … Beach, T. G. (2012). Correlation of Alzheimer Disease Neuropathologic Changes With Cognitive Status: A Review of the Literature. *Journal of Neuropathology & Experimental Neurology*, *71*(5), 362–381. https://doi.org/10.1097/NEN.0b013e31825018f7

Olszewska, D. A., Lonergan, R., Fallon, E. M., & Lynch, T. (2016). Genetics of Frontotemporal Dementia. *Current Neurology and Neuroscience Reports*, *16*(12), 107. https://doi.org/10.1007/s11910-016-0707-9

Papasozomenos, S. C., & Binder, L. I. (1987). Phosphorylation determines two distinct species of Tau in the central nervous system. *Cell Motility and the Cytoskeleton*, *8*(3), 210–226. https://doi.org/10.1002/cm.970080303

Pickering-Brown, S. M., Richardson, A. M. T., Snowden, J. S., McDonagh, A. M., Burns, A., Braude, W., Baker, M., Liu, W.-K., Yen, S.-H., Hardy, J., Hutton, M., Davies, Y., Allsop, D., Craufurd, D., Neary, D., & Mann, D. M. A. (2002). Inherited frontotemporal dementia in nine British families associated with intronic mutations in the tau gene. *Brain: A Journal of Neurology*, *125*(Pt 4), 732–751. https://doi.org/10.1093/brain/awf069

Poorkaj, P., Muma, N. A., Zhukareva, V., Cochran, E. J., Shannon, K. M., Hurtig, H., Koller, W.
C., Bird, T. D., Trojanowski, J. Q., Lee, V. M.-Y., & Schellenberg, G. D. (2002). An R5L τ
mutation in a subject with a progressive supranuclear palsy phenotype. *Annals of
Neurology*, *52*(4), 511–516. https://doi.org/10.1002/ana.10340

Qiang, L., Sun, X., Austin, T. O., Muralidharan, H., Jean, D. C., Liu, M., Yu, W., & Baas, P. W.
(2018). Tau Does Not Stabilize Axonal Microtubules but Rather Enables Them to Have
Long Labile Domains. *Current Biology*, *28*(13), 2181-2189.e4.
https://doi.org/10.1016/j.cub.2018.05.045

Ramazi, S., & Zahiri, J. (2021). Post-translational modifications in proteins: Resources, tools
and prediction methods. *Database*, *2021*, baab012.
https://doi.org/10.1093/database/baab012

Rohrer, J. D., Guerreiro, R., Vandrovcova, J., Uphill, J., Reiman, D., Beck, J., Isaacs, A. M.,
Authier, A., Ferrari, R., Fox, N. C., Mackenzie, I. R. A., Warren, J. D., Silva, R. de,
Holton, J., Revesz, T., Hardy, J., Mead, S., & Rossor, M. N. (2009). The heritability and
genetics of frontotemporal lobar degeneration. *Neurology*, *73*(18), 1451–1456.
https://doi.org/10.1212/WNL.0b013e3181bf997a

Sanders, D. W., Kaufman, S. K., DeVos, S. L., Sharma, A. M., Mirbaha, H., Li, A., Barker, S. J.,
Foley, A. C., Thorpe, J. R., Serpell, L. C., Miller, T. M., Grinberg, L. T., Seeley, W. W., &
Diamond, M. I. (2014). Distinct Tau Prion Strains Propagate in Cells and Mice and
Define Different Tauopathies. *Neuron*, *82*(6), 1271–1288.
https://doi.org/10.1016/j.neuron.2014.04.047

Sergeant, N., David, J.-P., Lefranc, D., Vermersch, P., Wattez, A., & Delacourte, A. (1997).
Different distribution of phosphorylated tau protein isoforms in Alzheimer's and Pick's
diseases. *FEBS Letters*, *412*(3), 578–582. https://doi.org/10.1016/S0014-
5793(97)00859-4

Shahani, N., Subramaniam, S., Wolf, T., Tackenberg, C., & Brandt, R. (2006). Tau Aggregation

and Progressive Neuronal Degeneration in the Absence of Changes in Spine Density and Morphology after Targeted Expression of Alzheimer's Disease-Relevant Tau Constructs in Organotypic Hippocampal Slices. *Journal of Neuroscience*, *26*(22), 6103–6114. https://doi.org/10.1523/JNEUROSCI.4245-05.2006

Shammas, S. L., Garcia, G. A., Kumar, S., Kjaergaard, M., Horrocks, M. H., Shivji, N., Mandelkow, E., Knowles, T. P. J., Mandelkow, E., & Klenerman, D. (2015). A mechanistic model of tau amyloid aggregation based on direct observation of oligomers. *Nature Communications*, *6*(1), 7025. https://doi.org/10.1038/ncomms8025

Shi, Y., Zhang, W., Yang, Y., Murzin, A. G., Falcon, B., Kotecha, A., van Beers, M., Tarutani, A., Kametani, F., Garringer, H. J., Vidal, R., Hallinan, G. I., Lashley, T., Saito, Y., Murayama, S., Yoshida, M., Tanaka, H., Kakita, A., Ikeuchi, T., … Scheres, S. H. W. (2021). Structure-based classification of tauopathies. *Nature*, *598*(7880), 359–363. https://doi.org/10.1038/s41586-021-03911-7

Skovronsky, D. M., Zhang, B., Kung, M.-P., Kung, H. F., Trojanowski, J. Q., & Lee, V. M.-Y. (2000). In vivo detection of amyloid plaques in a mouse model of Alzheimer's disease. *Proceedings of the National Academy of Sciences*, *97*(13), 7609–7614. https://doi.org/10.1073/pnas.97.13.7609

Spillantini, M. G., Yoshida, H., Rizzini, C., Lantos, P. L., Khan, N., Rossor, M. N., Goedert, M., & Brown, J. (2000). A novel tau mutation (N296N) in familial dementia with swollen achromatic neurons and corticobasal inclusion bodies. *Annals of Neurology*, *48*(6), 939–943. https://doi.org/10.1002/1531-8249(200012)48:6<939::aid-ana17>3.3.co;2-t

Stanford, P. M., Brooks, W. S., Teber, E. T., Hallupp, M., McLean, C., Halliday, G. M., Martins, R. N., Kwok, J. B. J., & Schofield, P. R. (2004). Frequency of tau mutations in familial and sporadic frontotemporal dementia and other tauopathies. *Journal of Neurology*, *251*(9), 1098–1104. https://doi.org/10.1007/s00415-004-0489-x

Stöhr, J., Wu, H., Nick, M., Wu, Y., Bhate, M., Condello, C., Johnson, N., Rodgers, J., Lemmin,

T., Acharya, S., Becker, J., Robinson, K., Kelly, M. J. S., Gai, F., Stubbs, G., Prusiner, S. B., & DeGrado, W. F. (2017). A 31-residue peptide induces aggregation of tau's microtubule-binding region in cells. *Nature Chemistry*, *9*(9), 874–881. https://doi.org/10.1038/nchem.2754

Strang, K. H., Golde, T. E., & Giasson, B. I. (2019). MAPT mutations, tauopathy, and mechanisms of neurodegeneration. *Laboratory Investigation*, *99*(7), 912–928. https://doi.org/10.1038/s41374-019-0197-x

Sui, D., Liu, M., & Kuo, M.-H. (2015). In Vitro Aggregation Assays Using Hyperphosphorylated Tau Protein. *Journal of Visualized Experiments : JoVE*, *95*, 51537. https://doi.org/10.3791/51537

Tan, R. H., Kril, J. J., Yang, Y., Tom, N., Hodges, J. R., Villemagne, V. L., Rowe, C. C., Leyton, C. E., Kwok, J. B. J., Ittner, L. M., & Halliday, G. M. (2017). Assessment of amyloid β in pathologically confirmed frontotemporal dementia syndromes. *Alzheimer's & Dementia : Diagnosis, Assessment & Disease Monitoring*, *9*, 10–20. https://doi.org/10.1016/j.dadm.2017.05.005

Tanaka, M., Chien, P., Naber, N., Cooke, R., & Weissman, J. S. (2004). Conformational variations in an infectious protein determine prion strain differences. *Nature*, *428*(6980), 323–328. https://doi.org/10.1038/nature02392

Taniguchi-Watanabe, S., Arai, T., Kametani, F., Nonaka, T., Masuda-Suzukake, M., Tarutani, A., Murayama, S., Saito, Y., Arima, K., Yoshida, M., Akiyama, H., Robinson, A., Mann, D. M. A., Iwatsubo, T., & Hasegawa, M. (2016). Biochemical classification of tauopathies by immunoblot, protein sequence and mass spectrometric analyses of sarkosyl-insoluble and trypsin-resistant tau. *Acta Neuropathologica*, *131*(2), 267–280. https://doi.org/10.1007/s00401-015-1503-3

Telling, G. C., Parchi, P., DeArmond, S. J., Cortelli, P., Montagna, P., Gabizon, R., Mastrianni, J., Lugaresi, E., Gambetti, P., & Prusiner, S. B. (1996). Evidence for the conformation of

the pathologic isoform of the prion protein enciphering and propagating prion diversity. *Science (New York, N.Y.)*, *274*(5295), 2079–2082. https://doi.org/10.1126/science.274.5295.2079

Tetz, G., Pinho, M., Pritzkow, S., Mendez, N., Soto, C., & Tetz, V. (2020). Bacterial DNA promotes Tau aggregation. *Scientific Reports*, *10*(1), 2369. https://doi.org/10.1038/s41598-020-59364-x

Trabzuni, D., Wray, S., Vandrovcova, J., Ramasamy, A., Walker, R., Smith, C., Luk, C., Gibbs, J. R., Dillman, A., Hernandez, D. G., Arepalli, S., Singleton, A. B., Cookson, M. R., Pittman, A. M., de Silva, R., Weale, M. E., Hardy, J., & Ryten, M. (2012). MAPT expression and splicing is differentially regulated by brain region: Relation to genotype and implication for tauopathies. *Human Molecular Genetics*, *21*(18), 4094–4103. https://doi.org/10.1093/hmg/dds238

Weingarten, M. D., Lockwood, A. H., Hwo, S. Y., & Kirschner, M. W. (1975). A protein factor essential for microtubule assembly. *Proceedings of the National Academy of Sciences of the United States of America*, *72*(5), 1858–1862. https://doi.org/10.1073/pnas.72.5.1858

Wesseling, H., Mair, W., Kumar, M., Schlaffner, C. N., Tang, S., Beerepoot, P., Fatou, B., Guise, A. J., Cheng, L., Takeda, S., Muntel, J., Rotunno, M. S., Dujardin, S., Davies, P., Kosik, K. S., Miller, B. L., Berretta, S., Hedreen, J. C., Grinberg, L. T., … Steen, J. A. (2020). Tau PTM Profiles Identify Patient Heterogeneity and Stages of Alzheimer's Disease. *Cell*, *183*(6), 1699-1713.e13. https://doi.org/10.1016/j.cell.2020.10.029

Whitwell, J. L., Josephs, K. A., Murray, M. E., Kantarci, K., Przybelski, S. A., Weigand, S. D., Vemuri, P., Senjem, M. L., Parisi, J. E., Knopman, D. S., Boeve, B. F., Petersen, R. C., Dickson, D. W., & Jack, C. R. (2008). MRI correlates of neurofibrillary tangle pathology at autopsy: A voxel-based morphometry study. *Neurology*, *71*(10), 743–749. https://doi.org/10.1212/01.wnl.0000324924.91351.7d

Wickramasinghe, S. P., Lempart, J., Merens, H. E., Murphy, J., Huettemann, P., Jakob, U., &

Rhoades, E. (2019). Polyphosphate Initiates Tau Aggregation through Intra- and

    Intermolecular Scaffolding. *Biophysical Journal*, *117*(4), 717–728.

    https://doi.org/10.1016/j.bpj.2019.07.028

Wille, H., Drewes, G., Biernat, J., Mandelkow, E. M., & Mandelkow, E. (1992). Alzheimer-like

    paired helical filaments and antiparallel dimers formed from microtubule-associated

    protein tau in vitro. *The Journal of Cell Biology*, *118*(3), 573–584.

    https://doi.org/10.1083/jcb.118.3.573

Winsor, C. P. (1932). The Gompertz Curve as a Growth Curve. *Proceedings of the National*

    Academy of Sciences of the United States of America, *18*(1), 1–8.

    https://doi.org/10.1073/pnas.18.1.1

Wu, J. W., Herman, M., Liu, L., Simoes, S., Acker, C. M., Figueroa, H., Steinberg, J. I.,

    Margittai, M., Kayed, R., Zurzolo, C., Paolo, G. D., & Duff, K. E. (2013). Small Misfolded

    Tau Species Are Internalized via Bulk Endocytosis and Anterogradely and Retrogradely

    Transported in Neurons *. *Journal of Biological Chemistry*, *288*(3), 1856–1870.

    https://doi.org/10.1074/jbc.M112.394528

Zhang, W., Falcon, B., Murzin, A. G., Fan, J., Crowther, R. A., Goedert, M., & Scheres, S. H.

    (2019). Heparin-induced tau filaments are polymorphic and differ from those in

    Alzheimer's and Pick's diseases. *ELife*, *8*, e43584. https://doi.org/10.7554/eLife.43584

Zhong, Q., Congdon, E. E., Nagaraja, H. N., & Kuret, J. (2012). Tau Isoform Composition

    Influences Rate and Extent of Filament Formation *. *Journal of Biological Chemistry*,

    287(24), 20711–20719. https://doi.org/10.1074/jbc.M112.364067